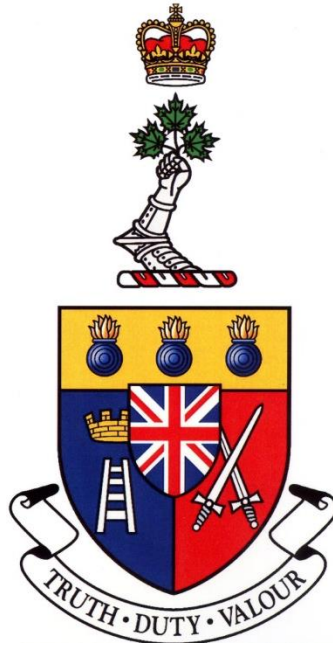


# MITIGATION OF END FLUX PEAKING IN CANDU FUEL BUNDLES USING NEUTRON ABSORBERS



A Thesis Submitted to the  
Department of Chemistry and Chemical Engineering of  
the Royal Military College of Canada  
by

Dylan J. C. Pierce

In Partial Fulfillment of the Requirements for the Degree of Master's of Science in Chemistry

March 2017

(RMC-CCE-CC504-15-3)

©This thesis may be used within the Department of National Defense but copyright for open publication remains the property of the author

# Acknowledgements

I would like to thank the Radiation Protection Bureau of Health Canada (RPB-HC), and the Physics and Fuel Division (PFD) and Environmental Compliance and Laboratory Services Division (ECLSD) of the Canadian Nuclear Safety Commission (CNSC), for the internship opportunities they provided during the course of my Master's degree. While working with RPB-HC, PFD and ECLSD of the CNSC, I was provided the opportunity to work on a variety of diverse projects. These terms allowed me to develop many useful skills that will be applicable in my future career, for that I am very appreciative.

While working with RPB-HC, I was able to learn about and develop gamma detector system simulations using the general purpose Monte Carlo code GEANT4. GEANT stands for GEometry AND Tracking, and is the fourth iteration of the code developed by CERN (Conseil Européen pour la Recherche Nucléaire). I was tasked with developing two separate gamma detector system simulations, the first of which used a single broad energy germanium (BEGe) detector from Canberra. The second gamma detector system used two BEGe detectors for gamma coincidence and anti-coincidence measurements. The purpose of these simulations was to provide a quick and accurate tool for predicting gamma detection efficiencies and spectra of a wide range of source configurations. This in turn provides users with the ability to optimize their experimental designs.

For my next internship I was working at the CNSC in two different divisions, PFD and ECLSD, each for six-month terms. While with PFD, I was tasked with investigating the impact of nuclear industry practices associated with reactor lattice physics calculations, such as simplifications to their lattice physics model. This project involved learning the WIMS-AECL code, a two-dimensional lattice physics code developed at Chalk River Laboratories (CNL). Also while working with PFD, I aided in the development of a code-framework to provide lattice physics outputs from WIMS-AECL, to NESTLE-C, a three-dimensional CANDU core physics code. This code-framework made use of Dakota, uncertainty quantification and data manipulation software developed at Sandia National Laboratories (SNL) and PERL scripts created by myself and a colleague.

For my second term with CNSC, I was given the opportunity to work at the CNSC's independent laboratory under the ECLSD. While at the lab I was given two separate major tasks. The first task was to help one of the senior analysts collect and analyze data from uranium ore concentrate (UOC) samples using a laser ablation (LA) unit coupled to an inductively-coupled plasma mass spectrometry (ICP-MS). As part of the analysis portion of this task, I developed Excel macros to incorporate statistical tests which determine and exclude outliers from the collected data. The second task was to help another senior analyst in a joint project with Environment Canada (EC). The goal of this project was to investigate a formula EC had developed to decontaminate building materials of various radiological hazards, in particular cesium. Here I was in charge of the experimental set-up and collecting of samples to be analyzed by the senior analyst.

Aside from these two projects while working at the lab, I was also tasked with preparing manuals for various instruments. This involved learning the techniques associated with each piece of equipment and developing a comprehensive procedure on how the instruments operate and experiments must be conducted. Manuals for the following instruments were prepared; an electrodeposition apparatus, an AUTOTAP and an air-flow calibration unit. The electrodeposition apparatus is used to deposit actinides from solution onto a stainless steel puck for use in radio-chromography. The AUTOTAP instrument is used to determine the tapped density of powder samples. The air-flow calibration unit is used to

calibration the air samplers which are used as part of the CNSC's Individual Environmental Monitoring Program (IEMP).

I would also like to thank the following individuals for their technical expertise and helping with kinks that arose during the course of completing my Master's thesis; Dr. Andrew Prudil, Dr. Maddison Andrews, Dr. Julian Atwood, LCdr. Stephane Paquette and Dr. Jingliang Hu. I would also like to thank my thesis supervisors, Dr. Paul Chan and Dr. Wei Shen, for the opportunity to work on this project. Finally, I would like to thank my family and girlfriend for their endless support and understanding for the duration of my Master's.

# Abstract

Pierce, Dylan (Chemistry). Royal Military College of Canada. January 2017. Mitigation of End Flux Peaking in CANDU Fuel Bundles Using Neutron Absorbers. Supervisors: Dr. Paul Chan and Dr. Wei Shen

End flux peaking (EFP) is a phenomenon where a region of elevated neutron flux occurs between two adjoining fuel bundles. These peaks lead to an increase in fission rate and therefore greater heat generation. It is known that the addition of neutron absorbers into fuel bundles can help mitigate EFP, yet implementation in Canada Deuterium Uranium (CANDU) type reactors using natural uranium fuel has not been pursued.

The computer code Monte Carlo N-Particle code (MCNP) 6.1 was used to develop a three-dimensional CANDU bundle-bundle contact model and simulate the addition of neutron absorbers positioned strategically within various locations within the fuel bundle. The burnable absorbers of interest include  $Gd_2O_3$  and  $Eu_2O_3$ . The locations investigated include: within the end pellets of a fuel stack; within the CANLUB layer, which is a graphite layer on the inner surface of a CANDU fuel element; within thin disks located at the ends of the fuel stack; and alloyed in the endplate, which is a structural component of the CANDU fuel bundle. Concentrations of the absorbers were varied to gain a better insight into their effect on the axial-thermal-neutron flux profile of the fuel bundle. This work supports the work done at RMCC in introducing BNAs in the CANDU fuel bundle design.

Keywords: CANDU, Reactor Physics, Burnable Neutron Absorbers, Gadolinium, Europium, End Flux Peaking, Reactor Safety.

# Résumé

Pierce, Dylan (Chimie). Collège militaire royal du Canada. Janvier 2017. *Atténuation des pics de flux neutronique aux extrémités des grappes de combustible CANDU à l'aide d'absorbeurs de neutrons*.  
Directeurs: Dr. Paul Chan et Dr. Wei Shen.

Les pics de flux aux extrémités des grappes de combustible sont un phénomène par lequel une région de flux neutronique élevé se produit entre deux grappes de combustible contiguës. Ces pics produisent une augmentation du taux de fission et, par conséquent, une plus grande génération de chaleur. On sait que l'addition d'absorbeurs de neutrons dans les grappes de combustible peut aider à réduire ces pics, mais sa mise en œuvre dans les réacteurs nucléaires de type CANDU (Canada Deutérium Uranium) utilisant de l'uranium naturel n'a pas encore été effectuée.

Le code d'ordinateur MCNP 6.1 ("Monte Carlo N-Particle") a été utilisé pour développer un modèle tridimensionnel d'un contact grappe à grappe CANDU et pour simuler l'ajout d'absorbeurs de neutrons placés à divers endroits stratégiques dans la grappe de combustible. Les absorbeurs de neutrons consommables pertinents à cette étude comprennent le trioxyde de gadolinium ( $Gd_2O_3$ ) et le trioxyde d'euporium ( $Eu_2O_3$ ). Les endroits étudiés incluent l'intérieur des pastilles de combustible à l'extrémité de l'empilement des pastilles, à l'intérieur de la couche CANLUB qui est une couche mince de graphite à la surface interne de la gaine, à l'intérieur de disques minces placés à l'extrémité de l'empilement des pastilles, et, finalement, formant une composante de l'alliage utilisé pour la fabrication des plaques d'extrémité qui font partie de la structure des grappes de combustible CANDU. On a varié les concentrations d'absorbeurs pour obtenir une meilleure connaissance de l'effet de leur présence sur le profil axial du flux de neutrons thermiques dans la grappe de combustible. Cette recherche supporte le travail effectué au CMRC sur l'introduction d'absorbeurs de neutrons consommables dans le design des grappes de combustible CANDU.

Mots-clefs: CANDU, Physique du réacteur, Absorbeurs de neutrons consommables, Gadolinium, Euporium, Pics de flux aux extrémités, Sûreté du réacteur.

# Table of Contents

<i>Acknowledgements</i> .....	<i>i</i>
<i>Abstract</i> .....	<i>iii</i>
<i>Résumé</i> .....	<i>iv</i>
<i>Glossary</i> .....	<i>xi</i>
<i>List of Acronyms</i> .....	<i>xii</i>
<i>Chapter 1: Introduction</i> .....	<i>1</i>
<i>Chapter 2: Research Objectives</i> .....	<i>2</i>
<i>Chapter 3: Background</i> .....	<i>3</i>
3.1 Nuclear Reactions.....	3
3.2 Interaction of Neutrons with Matter.....	3
3.3 Fission Chain Reaction.....	4
3.4 Canadian Deuterium Uranium (CANDU) Reactor.....	5
3.4.1 CANDU Fuel Bundle Design.....	6
3.5 Cross Section.....	8
3.5.1 Introduction.....	8
3.5.2 Types of Cross Sections.....	9
3.5.3 Macroscopic Cross Section.....	10
3.5.4 Dependencies of Cross Sections.....	12
3.6 Fuel Burnup Effects.....	13
3.6.1 Refuelling Transient.....	14
3.6.2 Plutonium Peaking.....	15
3.7 Burnable Neutron Absorber.....	15
3.8 End Flux Peaking.....	17
3.9 Fuel Bundle Radial Power Peaking Factor.....	18
3.10 The Neutron Transport Equation.....	19
3.10.1 Introduction.....	19
3.10.2 Neutron as a Point Particle.....	19
3.10.3 Neutron Density and Flux.....	22
<i>Chapter 4: Methodology</i> .....	<i>24</i>
4.1 Monte Carlo Method.....	24
4.2 Monte Carlo N-Particle (MCNP) Transport Code.....	24
4.2.1 Introduction.....	24

4.2.2	<i>Surfaces</i> .....	25
4.2.3	<i>Cells</i> .....	25
4.2.4	<i>Nuclear Information and Reactions</i> .....	27
4.2.5	<i>Cross Sections</i> .....	28
4.2.6	<i>Source Specification</i> .....	30
4.2.7	<i>Tallies and Output</i> .....	30
4.2.8	<i>Physics</i> .....	32
4.2.9	<i>Neutron Interactions</i> .....	33
4.3	<i>Least Squares Method</i> .....	36
4.4	<i>Geometry Specification</i> .....	37
4.5	<i>Material Specification</i> .....	41
<i>Chapter 5: Results and Discussion</i> .....		46
5.1	<i>Preliminary Model Results</i> .....	46
5.2	<i>KCODE Cycle Determination</i> .....	49
5.2.1	<i>Error Calculation</i> .....	50
5.3	<i>Model Validation</i> .....	51
5.4	<i>MATLAB Automation</i> .....	53
5.5	<i>Absorber Location Testing</i> .....	55
5.5.1	<i>Thin Disks</i> .....	55
5.5.2	<i>CANLUB</i> .....	56
5.5.3	<i>End Pellets</i> .....	57
5.5.4	<i>Endplates</i> .....	59
5.5.5	<i>Ring-Optimized Absorber Amounts</i> .....	60
5.6	<i>Swapping Adjacent and End Pellet Locations</i> .....	69
5.7	<i>Effects of Doped Fuel Pellets on the Other Fuel Rings</i> .....	71
5.7.1	<i>Effect of Center-Optimized Fuel Bundle Configuration</i> .....	71
5.7.2	<i>Effect of Inner-Optimized Fuel Bundle Configuration</i> .....	73
5.7.3	<i>Effect of Intermediate-Optimized Fuel Bundle Configuration</i> .....	75
5.7.4	<i>Effect of Outer-Optimized Fuel Bundle Configuration</i> .....	76
5.7.5	<i>Effect of Using All Ring-Optimized Results</i> .....	78
5.8	<i>Bundle-Optimized Results</i> .....	79
<i>Chapter 6: Conclusion</i> .....		82
<i>Chapter 7: Recommendations</i> .....		83
<i>References</i> .....		84
<i>Appendices</i> .....		88
<i>Appendix A.1: Surfaces Defined by Equations</i> .....		89

<i>Appendix A.2: Derivation of the F4 Tally</i> .....	91
<i>Appendix A.3: Section of General MCNP Input File for Automation</i> .....	93
<i>Appendix A.4: MATLAB Script to Generate a Set of MCNP Trials</i> .....	94
<i>Appendix A.5: Batch Script to Execute Multiple MCNP Inputs</i> .....	96
<i>Appendix A.6: MATLAB Script to Lift Output From MCNP Output File</i> .....	97
<i>Appendix A.7: MATLAB Script for Function “importfile” Used In MATLAB Output Script</i> .....	100
<i>Appendix A.8: MATLAB Script for Function “importerror” Used In MATLAB Output Script</i> ....	101
<i>Appendix A.9: Python Script to Determine the Optimal Amount of Europium Oxide</i> .....	102



# List of Figures

Figure 3.1: Schematic diagram of typical fission chain reaction.....	4
Figure 3.2: CANDU reactor schematic courtesy of [15] .....	6
Figure 3.3: CANDU fuel bundle design, including the 37 element pattern [11].....	7
Figure 3.4: Schematic representation for the definition of cross section.....	9
Figure 3.5: Measurement of neutron from a beam that passes through a target .....	10
Figure 3.6: $1/v$ vs. non- $1/v$ absorber, the green curve is the example non- $1/v$ absorber U-235 and the red curve is the example $1/v$ curve H-1, from KAERI website .....	12
Figure 3.7 Typical decay chain for U-238 during reactor operation .....	13
Figure 3.8: Reactivity in NU fuel in CANDU reactors during normal irradiation at constant flux level [4] .	14
Figure 3.9: Illustration of End Flux Peaking.....	18
Figure 3.10: Polar Coordinate representation of point-like neutron courtesy of HyperPhysics webpage on Spherical Polar Coordinates ( <a href="http://hyperphysics.phy-astr.gsu.edu/hbase/sphc.html">http://hyperphysics.phy-astr.gsu.edu/hbase/sphc.html</a> ).....	21
Figure 3.11: Representation of the volume element $dV$ , image courtesy of HyperPhysics webpage on Spherical Polar Coordinates ( <a href="http://hyperphysics.phy-astr.gsu.edu/hbase/sphc.html">http://hyperphysics.phy-astr.gsu.edu/hbase/sphc.html</a> ).....	22
Figure 4.1: 2D cross section of sphere centered at origin with 3.0 cm radius .....	26
Figure 4.2: First MCNP model geometry including axial and radial image of model .....	38
Figure 4.3: Second MCNP model geometry .....	38
Figure 4.4: Reflective boundary conditions mimic an infinite lattice of fuel bundles .....	39
Figure 4.5: U-235 fission spectrum using the empirical formula from Equation 5.1.2 .....	40
Figure 4.6: Two half bundle model, including blown up cross section of a fuel element.....	41
Figure 5.1: Effect of geometry on axial-thermal-neutron flux throughout the length of the bundle, a) Full length of the fuel bundle, b) zoomed into one end region of the fuel bundle.....	46
Figure 5.2: Shelf-shielding model.....	47
Figure 5.3: Axially segmented homogenized fuel bundle to obtain axial-flux output .....	48
Figure 5.4: Results of parametric study for number of KCODE cycles.....	49
Figure 5.5: EFP error calculation on results from parametric study to demonstrate relationship between number of KCODE cycles and relative error .....	50
Figure 5.6: RPPF comparison between MCNP 6.1 model and values taken from correspondence with CAMECO.....	52
Figure 5.7: Automation scheme for absorber trials .....	54
Figure 5.8: Trial results using neutron absorbing material in thin disks.....	56
Figure 5.9: Trial results using neutron absorbing material mixed in the CANLUB layer.....	57
Figure 5.10: Trial results using neutron absorbing material mixed in a single end pellet .....	58
Figure 5.11: Trial results using neutron absorbing material mixed in two end pellets.....	59
Figure 5.12: Trial results using neutron absorbing material mixed in the endplate.....	60
Figure 5.13: Process by which the optimal values were found .....	61
Figure 5.14: Ring-optimized results for the amount of $\text{Eu}_2\text{O}_3$ placed into the both end pellets .....	64
Figure 5.15: RPPF comparison between MCNP and literature values with center-optimized amount of $\text{Eu}_2\text{O}_3$ was added to the center element.....	66
Figure 5.16: RPPF comparison between MCNP and literature values with an inner-optimized amount of $\text{Eu}_2\text{O}_3$ added to the fuel elements of the inner ring .....	67

<i>Figure 5.17: RPPF comparison between MCNP and literature values with an intermediate-optimized amount of <math>\text{Eu}_2\text{O}_3</math> added to the fuel elements of the intermediate ring .....</i>	<i>67</i>
<i>Figure 5.18: RPPF comparison between MCNP and literature values with an outer-optimized amount of <math>\text{Eu}_2\text{O}_3</math> added to the fuel elements of the outer ring .....</i>	<i>68</i>
<i>Figure 5.19: Effect of swapping the ring-optimized adjacent and end pellet locations on the EFP curve for fuel elements in each fuel ring .....</i>	<i>70</i>
<i>Figure 5.20: Effects of adding ring-optimized amount of <math>\text{Eu}_2\text{O}_3</math> in the center element on the other three fuel rings.....</i>	<i>72</i>
<i>Figure 5.21: Effects of adding ring-optimized amount of <math>\text{Eu}_2\text{O}_3</math> in the inner element on the other three fuel rings.....</i>	<i>74</i>
<i>Figure 5.22: Effects of adding ring-optimized amount of <math>\text{Eu}_2\text{O}_3</math> in the intermediate element on the other three fuel rings .....</i>	<i>76</i>
<i>Figure 5.28: Effects of adding ring-optimized amount of <math>\text{Eu}_2\text{O}_3</math> in the outer element on the other three fuel rings.....</i>	<i>78</i>
<i>Figure 5.24: Effect of adding ring-optimized <math>\text{Eu}_2\text{O}_3</math> added to each of the fuel rings simultaneously .....</i>	<i>79</i>
<i>Figure 5.30: Comparison of bundle-optimized solution to all previous cases.....</i>	<i>81</i>

# List of Tables

<i>Table 3.1: CANDU fuel pellet design [2]</i> .....	8
<i>Table 3.2: Properties of burnable neutron absorbers candidates</i> .....	16
<i>Table 4.1: Available MCNP tallies</i> .....	30
<i>Table 4.2: F4:N Tally Quantity Scored</i> .....	31
<i>Table 4.3: CANDU fuel bundle design features</i> .....	37
<i>Table 4.4: Information obtained from KAERI website</i> .....	42
<i>Table 4.5: Weight fractions for natural UO<sub>2</sub></i> .....	42
<i>Table 4.6: Constants used in the determination of atomic composition of doped fuel</i> .....	43
<i>Table 4.7: Isotropic abundance for 10 mg of Eu<sub>2</sub>O<sub>3</sub> added to a fuel pellet</i> .....	45
<i>Table 5.1: Calculated end flux peaking factors for NU-37 at nominal power from Balaceneau and Hrista [3]</i> .....	48
<i>Table 5.2: MCNP 6.1 model comparison [1][31]</i> .....	51
<i>Table 5.3: Demonstrating location of Eu<sub>2</sub>O<sub>3</sub> in each graph of Figure 5.19</i> .....	63
<i>Table 5.4: Description of Eu<sub>2</sub>O<sub>3</sub> location and amount for Figure 5.20</i> .....	71
<i>Table 5.5: Description of Eu<sub>2</sub>O<sub>3</sub> location and amount for Figure 5.21</i> .....	73
<i>Table 5.5: Description of Eu<sub>2</sub>O<sub>3</sub> location and amount for Figure 5.22</i> .....	75
<i>Table 5.6: Description of Eu<sub>2</sub>O<sub>3</sub> location and amount for Figure 5.23</i> .....	77
<i>Table 5.7: Bundle-Optimized amount of Eu<sub>2</sub>O<sub>3</sub> in the inner and outer fuel elements</i> .....	80
<i>Table A.1.1: Geometry definitions in MCNP</i> .....	89

# Glossary

<i>Burnable Neutron Absorber:</i>	term indicating a material which originally possesses a high neutron absorption cross section that decreases as the fluence accumulates
<i>Burnup:</i>	a value indicating the amount of power generated by the fuel, commonly provided in units of Mega-Watt days per kilogram of uranium (MWD/kgU)
<i>Criticality:</i>	a method of quantitatively describing a fission chain, defined as the ratio of neutrons in the one generation to the number of neutrons in the next generation
<i>Cross Section:</i>	the probability for a particular nuclear interaction to take place, in terms of an effective target area defined by the target and incident particle
<i>End Flux Peaking:</i>	phenomenon in CANDU fuel bundles caused by a difference in absorption cross section between the UO <sub>2</sub> fuel and structural Zircaloy-4 material
<i>Fluence:</i>	product of neutron flux and irradiation time
<i>Fuel Element:</i>	component of a fuel bundle, also called fuel rod, consisting of a stack of fuel pellets inserted in a sheath of cladding and leak tight with two end caps
<i>Full Power Day:</i>	operation of a reactor at full power for 24 hours
<i>Plutonium Peaking:</i>	transient which occurs between 40 and 50 full power days, and results from an accumulation of fissile plutonium which subsequently undergoes fission introducing a positive reactivity
<i>Radial Power Peaking Factor:</i>	a ratio of the power of a given element in a CANDU fuel bundle to the average element power
<i>Xenon (Refuelling) Transient:</i>	transient which occurs within the first 2 to 3 full power days, resulting in a power spike located near fresh fuel bundles which leads to a steep drop due to build-up of xenon in the fresh fuel
<i>Zircaloy-4:</i>	structural material used in CANDU fuel bundles, is a metal alloy primarily consisting of zirconium, chosen for its low neutron absorption cross section

# List of Acronyms

AECL	Atomic Energy Canada Limited
ACTI	Advanced Computational Technology Initiative
ACTL	Activation Library
BNA	Burnable Neutron Absorber
CANDU™	CANada Deuterium Uranium
EFP	End Flux Peaking
ENDF	Evaluated Nuclear Data File
ENDL	Evaluated Nuclear Data Library
EPDL	Evaluated Photon Data Library
FGTT	Free-Gas Thermal Treatment
FPD	Full Power Day
KAERI	Korea Atomic Energy Research Institute
LANL	Los Alamos National Laboratory
LOCA	Loss of Cooling Accident
LSM	Least Squares Method
LWR	Light-Water Reactor
MCNP	Monte Carlo N-Particle
NU	Natural Uranium
RPPF	Radial Power Peak Factor
SCC	Stress Corrosion Cracking
ZED	Zero-Energy Deuterium

# List of Symbols

$E_{293}$	the energy of the incident particle at room temperature, which is 293 K
$E_B$	total bundle energy
$\bar{E}_E$	the average element energy
$E_{FD}$	the fission energy deposited in a single element
$E_{FM}$	the fission energy deposited in a given mass of material
$E_T$	the energy of the incident particle at a temperature of $T$
$F_f$	the Radial Power Peaking Factor (RPPF)
$F_{f1}$	fission fragments
$F_{f2}$	fission fragments
$F_N$	original fissionable nucleus
$\hbar$	Planck's constant divided by $2\pi$ , and equals $6.62606957 \times 10^{-34} \text{ J} \cdot \text{s}$
$I$	intensity (flux) of the beam
$k$	Boltzmann constant
$k_\infty$	is the multiplication factor for an idealized case of an infinite reactor with no loss of neutrons (leakage)
$k_{eff}$	effective multiplication factor includes leakage of neutrons at the peripheries and is thus a more physical representation of criticality
$\lambda$	reduced wavelength
$l$	some distance which a particle travels
$M_C$	the mass of the given material
$n$	number of particles per $\text{cm}^3$ in incident beam
$n(\vec{r}, E, t)$	the neutron density
$N$	the number density of target particles
$\phi(\vec{r}, E, t)$	total flux
$\Phi(\vec{r}, \vec{\Omega}, E, t)$	the angular flux

$\phi^{end}$	the neutron flux in the end regions
$\phi^{mid\ plane}$	the neutron flux within the mid plane of the bundle
$p$	momentum of the particle
$P^{flux}$	end flux peaking factor
$p(V)$	probability density function
$R$	the remainder of the particles and photons which might be created as the result of a particular fission
$\sigma$	microscopic cross section (barns)
$\sigma_a$	absorption microscopic cross section
$\sigma_{elastic}$	elastic scattering microscopic cross section
$\sigma_{fission}/\sigma_f$	fission microscopic cross section
$\sigma_\gamma$	radiative capture microscopic cross section
$\sigma_{inelastic}$	inelastic scattering microscopic cross section
$\sigma_s$	scattering macroscopic cross section
$\sigma_{total}/\sigma_t$	total microscopic cross section
$\Sigma$	macroscopic cross section
$\Sigma_t$	total macroscopic cross section
$S$	score provided by Least Squares Method
$T_l$	track length
$v$	velocity
$V$	volume of the cell in MCNP
$W$	particle weight
$X$	thickness
$\xi$	random number

# Chapter 1: Introduction

End flux peaking (EFP) is a phenomenon that affects the flux profile of a fuel bundle and occurs in the vicinity of bundle-bundle interfaces (also known as the bundle end-region) [1]. Here the fuel stack in each element ends and the element is sealed with a Zircaloy-4 end cap. The endcap is then welded to a Zircaloy-4 endplate to maintain the bundle geometry. The bundle is positioned within a fuel channel in contact with other CANDU bundles. Within a fuel channel, an end region consists of heavy water ( $D_2O$ ) coolant, Zircaloy-4 bundle end plate and end caps, and uranium dioxide fuel pellets [2]. Since the coolant and Zircaloy-4 have much lower neutron absorption cross sections,  $\sigma_a$ , than the uranium dioxide fuel, this causes neutrons to pass through these materials more readily. The neutrons which pass more readily, lead to peaks in the thermal neutron flux within the end region of the fuel bundles. Along with the peak in the end regions, some neutrons diffuse into the end of the fuel stack leading to a local increase in the flux in the fuel. These effects caused by neutrons passing through the end regions ultimately are the cause of EFP in CANDU fuel bundles.

For CANDU fuel bundles, the existence of EFP results in a higher fission rate and therefore more heat production and higher temperatures in the fuel adjacent to the end regions [3]. See Figure 3.1 for the fuel bundle geometry and Figure 3.9 for a schematic demonstrating EFP. Localized high temperatures can lead to an increased risk of sheath strain, corrosion and fuel centreline melting. The issues associated with EFP are deemed manageable during normal operation conditions. Most EFP work involves accurately characterizing the phenomena but ignores potential methods of mitigating it. However, all of these potential issues can have significant impact on the integrity of the sheath and fission gas release during over-power or loss of coolant accident (LOCA) conditions [1].

In the work done by *Chan et al.*, it was determined that a combination of gadolinium oxide ( $Gd_2O_3$ ) and europium oxide ( $Eu_2O_3$ ) was able to mitigate both the refuelling transient and the plutonium peak.  $Gd_2O_3$  targets the refuelling transients since it has a burn-out rate that matches closely with the Xenon build-up rate, while  $Eu_2O_3$  targets plutonium peaking since it has a long chain of stable isotopes that have a relatively large thermal absorption cross section. It was concluded by *Chan et al.* that ~180 mg of  $Gd_2O_3$  and ~1000 mg of  $Eu_2O_3$  per bundle can both suppress the refuelling transient and lower the axial plutonium peak. The combined mass of the absorbers to the total mass of the fuel bundle represents only  $\sim 2 \times 10^{-3}$  wt% (weight percent) [4].

The present work investigates distributing the gadolinium and europium oxide neutron absorbers throughout the fuel bundle.  $Gd_2O_3$  and  $Eu_2O_3$  were chosen over other burnable neutron absorbers as they were demonstrated to effectively mitigate fuelling transients as part of the work done at RMCC by *Chan et al.* The neutron absorber will be introduced into the fuel bundle through a variety of locations. These locations include, thin disks, CANLUB, end pellets, and end plates. The goal is to introduce the neutron absorbing material in such a way to mitigate EFP while minimizing negative effects on the neutron economy. Minimizing negative effects on neutron economy correlates to a minor cost in fuel bundle discharge burnup. For these reasons, neutron absorbers may provide a viable means to mitigate the reactivity transients and end-flux peaking simultaneously.



# Chapter 2: Research Objectives

The primary objective of this work is to demonstrate that the addition of neutron absorbers to the end region will mitigate end flux peaking within CANDU natural uranium (NU) fuel bundles. To achieve this objective, the present study involves the use of a computer-simulated bundle-bundle geometry model to calculate the spatial flux distribution with various concentrations of absorber materials included in the designated locations. These simulations are done with the Monte Carlo N-Particle Transport Code 6.1 (MCNP 6.1) developed and maintained by the Los Alamos National Laboratory (LANL). The bundle-bundle model uses the geometry for the standard 37-element CANDU fuel bundle, with simplifications made to the fuel pellet stack, end region and end plate geometry. The model created is the first three-dimensional EFP MCNP 6.1 model developed. The model and results from this work support the design and implementation of BNA in a CANDU fuel bundle. Since there are concerns over the effects of end flux peaking during refuelling, the model was constructed to investigate typical refuelling conditions. Mitigation of end flux peaking will provide more even power production in the fuel during reactor operation as well as improving fuel margins during overpower and loss of coolant accidents conditions.

# Chapter 3: Background

## 3.1 Nuclear Reactions

A nuclear reactor is an extremely complex system where particles are being generated from various nuclear processes. First, it would be best to outline what is meant by a nuclear reaction. A nuclear reaction is said to occur when either two nuclei or a nucleus and particle interact at the level of the atomic nuclei to produce two or more nuclear particles and/or some form of radiation such as gamma particles. To gain a better understanding, consider the following simple interaction of two particles,  $a$  and  $b$ , which interact to produce two different particles,  $c$  and  $d$ , as shown below:



Experimentally, one of the reactant particles is considered to be a target and therefore is assumed at rest, while the other particle is projected towards the target. In the generic reaction described above in Equation 3.1.1, particle  $a$  is considered the target while particle  $b$  is the incident particle [5] [6].

## 3.2 Interaction of Neutrons with Matter

Like any other particle in a nuclear reaction, neutrons can interact with particles through a wide variety of interactions. Two categories of interactions are scattering and absorption. If a neutron interacts with a nucleus and both the target and the neutron retain their nature as the products of the reaction, the reaction is called a scattering reaction. Not all interactions between neutrons and nuclei have the nature of the products remaining the same as the reactants. Interactions which involve a change in nature of the reactants are classified under the absorption category [7][8] [9].

An important form of absorption reaction is fission. Fission forms the backbone of energy generation in a reactor. The process of fission occurs when a neutron is absorbed by certain heavy nuclei. The heavy nucleus becomes unstable and splits into two fragments. This separation into two fragments is accompanied by a difference in mass between reactants (the neutron and heavy nucleus), and products (the fission fragments plus other particles emitted in such a nuclear reaction such as neutrons, neutrinos and gamma photons). But since mass-energy is neither created nor destroyed, it instead appears as energy. The process of fission will be discussed in more detailed in the following section [10].

### 3.3 Fission Chain Reaction

As mentioned in the previous section, fission is a process where a heavy nucleus is split into two separate nuclei, called fission fragments, releasing energy in the process. The fission fragments are highly unstable and undergo their own radioactive decay, after which point they are referred to as fission products. Like the fission fragments, the fission products may not necessarily be in their ground state and therefore may also be unstable and continue to decay [11].

Fission can be classified as either spontaneous or induced, and is dependent on the process which initiates it. Spontaneous fission occurs as a radioactive decay process similar to alpha- or beta- decay. While induced fission occurs when some form of energy, such as the absorption of a neutron, is imparted onto the original heavy nucleus [6]. Spontaneous fission can be represented by the Equation 3.3.1a and Equation 3.3.1b represents induced fission.

$$F_N \rightarrow F_{f1} + F_{f2} + R \quad 3.3.1a$$

$$F_N + x \rightarrow F_{f1} + F_{f2} + R \quad 3.3.1b$$

Where  $F_N$  is the original fissionable nucleus,  $F_{f1}$  and  $F_{f2}$  are the fission fragments created right after fission has taken place, and  $R$  is the remainder of the particles and photons which might be created as the result of a particular fission. The remainder may consist of neutrons, neutrinos, or gamma rays [6]. In Equation 3.3.1b,  $x$  is an incident particle such as a neutron or gamma photon (photofission).

Since the main focus of a reactor is to safely induce as many fission reactions as possible, particular emphasis is placed on the investigations of induced fission reactions. A typical nuclear chain reaction is shown in Figure 3.1.

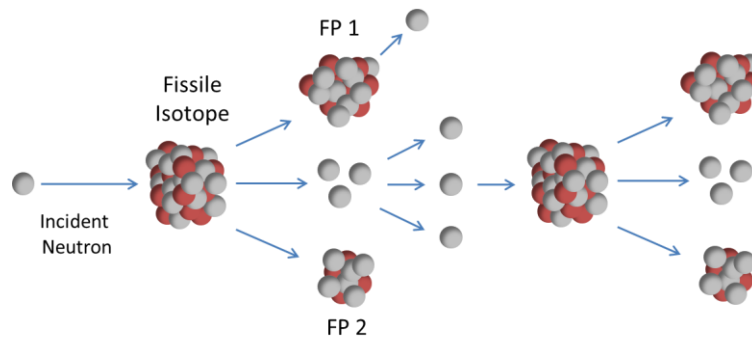


Figure 3.1: Schematic diagram of typical fission chain reaction

Neutron induced fission can be summarized as follows,

1. A neutron is incident upon some fissile nucleus, approximated to be spherical in shape (Bohr Model);
2. Depending on the cross sections associated with the fissile nucleus, the neutron may be absorbed by the nucleus, if it does the energy of the neutron is shared by the nucleons causing oscillation which elongate and distort the spherical nucleus;
3. If the energy is sufficient the distortion of the nucleus will form a dumbbell shape, if the energy is greater than the energy keeping the nucleus together, the nucleus will burst and form two separate fission fragments as well as some gamma rays and neutrons;

4. These newly generated neutrons will go on to generate further fissions, and so on.

After the neutron interacts with the first nucleus, it will subsequently produce more neutrons which then react with other nuclei and so on.

The energy of the incident neutron plays a large role in the fission process. For CANDU reactors neutrons are classified into two separate groups, thermal for neutrons with energies lower than roughly 1 eV, and fast for those with energies greater than this cut off energy [12].

A method of quantitatively describing a fission chain reaction is by the use of the multiplication (criticality) factor,  $k$ , which is defined in the following equation:

$$k = \frac{\text{number of fissions in one given generation}}{\text{number of fissions in preceding generation}} \quad 3.3.2$$

If  $k$  is greater than one, the reaction is said to be supercritical. Supercriticality refers to an increase in neutrons from generation to generation leading to an increase of energy produced with time. If  $k$  is less than one, the reaction is said to be subcritical. Subcriticality refers to a decrease in neutrons in successive generations and thus a decrease of energy produced with time [6]. Finally, if  $k$  is exactly one the reaction is said to be critical and thus the fission reaction proceeds at a constant rate, releasing a steady power [13].

In terms of reactor physics, the factor,  $k$ , can be characterized in two different ways. These two characterizations are the infinite multiplication factor,  $k_{\infty}$ , and the effective multiplication factor,  $k_{eff}$ . The infinite multiplication factor is the multiplication factor for an idealized case of an infinite reactor with no loss of neutrons (leakage). The effective multiplication factor includes leakage of neutrons at the peripheries and is thus a more realistic representation of criticality. The equations which describe each type of multiplication factor are provided below [14].

$$k_{\infty} = \frac{\text{number of neutrons produced in a generation}}{\text{number of neutrons absorbed in the previous generation}} \quad 3.3.3$$

$$k_{eff} = \frac{\text{number of neutrons produced in a generation}}{\text{number of neutrons absorbed + leak out in previous generation}} \quad 3.3.4$$

## 3.4 Canadian Deuterium Uranium (CANDU) Reactor

The Canadian Deuterium Uranium (CANDU) reactor is classified as a pressurized heavy water reactor (PHWR). The classification comes from the nature of the moderator (heavy water) and the coolant, also heavy water, but pressurized. Figure 3.2 below demonstrates the particular design features in a CANDU reactor.

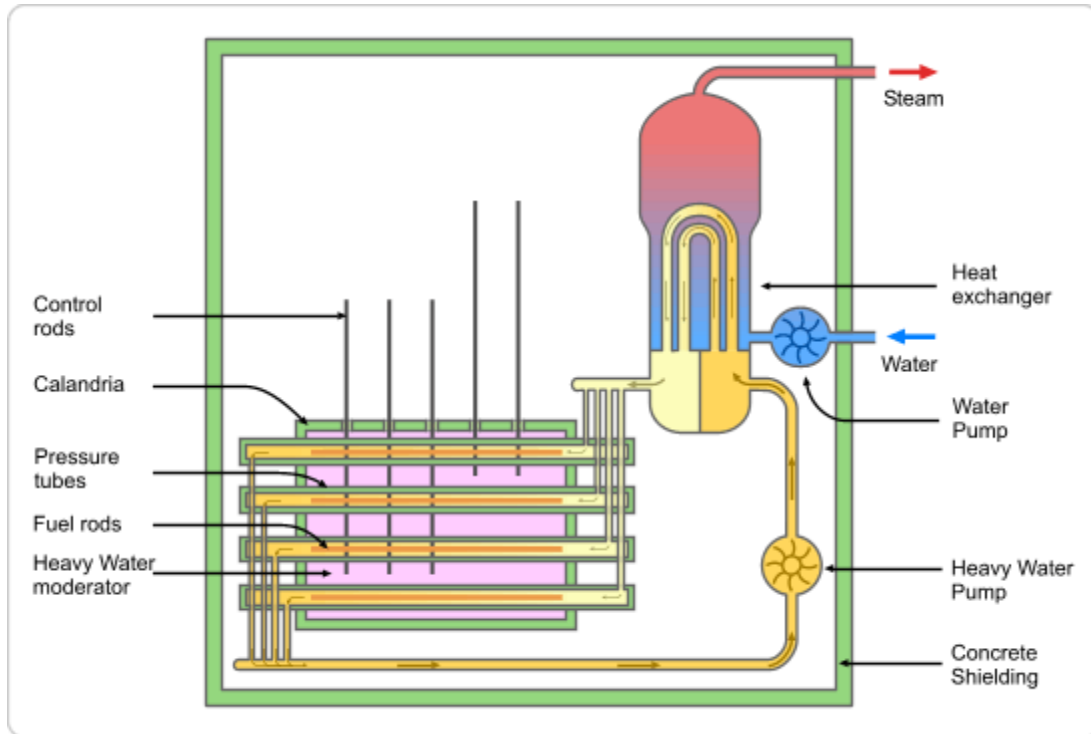


Figure 3.2: CANDU reactor schematic courtesy of [15]

Unlike most reactor designs which feature a vertical reactor core, the CANDU reactor core is set horizontally. Another difference between CANDU and most other reactors is the use of a heavy water ( $D_2O$ ) moderator. The  $D_2O$  moderator is contained within a 6.0 m long and 7.6 m in diameter cylindrical vessel called the calandria. Within the calandria exists 300 to 600 fuel channels. The number of fuel channels depends on the model of CANDU reactor [15].

In each fuel channels exists a pressure tube which contains the heavy water coolant and fuel bundles. The coolant is pressurized to 10.4 MPa. Each pressure tube contains 12-13 fuel bundles each made of 37 fuel elements or rods arranged in an annular pattern [15]. Fuel bundles will be discussed in greater detail in the following section. The pressure tubes are connected by feeder tubes to headers above the core [15]. These headers are the intermediate between the core and the steam generators. The flow of the coolant within the core is provided by by the heat transport pumps.

### 3.4.1 CANDU Fuel Bundle Design

Approximately 31 ceramic natural uranium dioxide (0.72% enriched U-235) fuel pellets measuring ~1.54 cm in length are placed in each of the 37 ~50 cm long fuel elements [14]. The fuel pellets are designed to include; a pellet dish, as well as diametrical and axial clearance and chamfers. The purpose of the pellet dish is to accommodate for thermal expansion of the pellet due to the high temperatures experienced during irradiation. The diametrical clearance between the pellet and the inner surface of the sheath makes it easier to load the fuel elements with the fuel pellets. The axial clearance is included to limit the axial interference between the pellet and endcap. Along with the axial clearance, the

endcap is machined to include a cavity. This cavity serves the same purpose as the axial clearance and is included to provide a space in the fuel element to store fission gases produced during irradiation [15].

37 individual fuel elements are then placed in 4 concentric rings: 18 elements make up the outer ring, 12 make up the intermediate ring, the inner ring has 6 elements and finally 1 central element. On the inner surface of each fuel element exists a protective graphite coating referred to as CANLUB. CANLUB is designed to help mitigate the effects of stress corrosion cracking (SCC) of the Zircaloy-4 sheaths. SCC is caused by a combination of corrosion, of the Zircaloy-4 sheath due to iodine as a fission product and the strain experienced during reactor operation [15] [16].

The rings which make up the radial cross section of a CANDU fuel bundle are also referred to numerically, where ring 1 represents the center element, and ring 4 represents the outer elements [17] [18]. This ring geometry can be seen in Figure 3.3. Welded onto each of the 18 outer elements are bearing pads that maintain the separation between the bundle and the pressure tube. Similar to the bearing pads, spacer pads are welded onto the inner surface of the outer elements and the outer surface of all elements in subsequent rings. Bearing pads maintain the distance between the fuel elements, to maintain sufficient coolant flow through the fuel bundle. The fuel elements are then locked into this geometry via end plates welded at both ends [19] [20] [21].

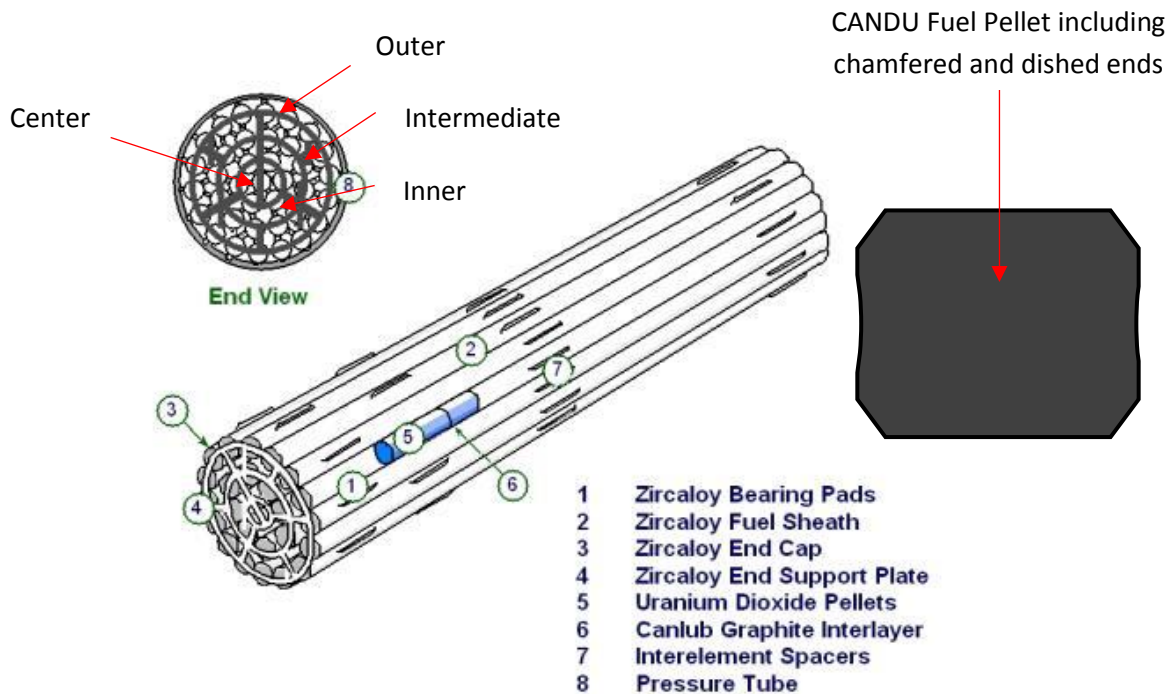


Figure 3.3: CANDU fuel bundle design, including the 37-element pattern [11]

A summary of the key design features of the CANDU fuel bundle is summarized in the table below. Note that these values are typical of a CANDU reactor.

Table 3.1: CANDU fuel pellet design [2]

Parameter	Value	Parameter	Value
Number of elements per bundle	37	Sheath thickness (mm)	0.4
U weight per bundle (kg)	19.2	Pellet outside diameter (mm)	12
Zr weight per bundle (kg)	2.2	Pellet length (mm)	16
Overall bundle length (mm)	495	Pellet density (g/cm <sup>3</sup> )	10.6
Overall bundle diameter (mm)	102	Endplate width (outer ring) (mm)	4.9
Element length (mm)	493	Endplate thickness (mm)	1.6
Element outside diameter (mm)	13		

## 3.5 Cross Section

### 3.5.1 Introduction

To understand what cross sections are, its best to investigate the physical definition of cross section by considering the following experiment. Consider a beam of mono-energetic particles being incident upon a target of some given thickness  $X$  and surface area  $A$ , as shown in Figure 3.4 [22]. Assuming that the incident beam has  $n$  particles per cm<sup>3</sup>, that are travelling at a velocity defined by  $v$  in cm/s. The intensity (flux) of the beam is given by,

$$I = nv \quad 3.5.1$$

To find the number of incident particles which strike the target in a given second, use the following relation,

$$nvA = IA \quad 3.5.2$$

Since the incident particles are small and assuming the target is thin, most incident particles will not interact with the particles in the target material [5]. Those particles which do interact with the target, collide at a rate given by the following equation,

$$\text{Number of collisions per second (in entire target)} = \sigma INAX \quad 3.5.3$$

where  $\sigma$ , is the microscopic cross section. The microscopic cross section can be viewed as a proportionality constant, equal to the number of collisions per second with a single target per unit intensity of the beam. The common unit for cross section is the barn ( $b$ ), where  $1 b = 10^{-28} m^2$ [5] [6].

With  $N$  representing the number density of target particles which form the thin target and has units of  $\text{cm}^{-3}$ .

From Equation 3.5.3 multiplying the area,  $A$ , by the thickness of the target,  $X$ , gives volume which has units of  $\text{cm}^3$ . If the number density of target atoms  $N$ , is multiplied by the volume of the target, the product is simply the number of target particles, which is unitless. Therefore, to determine the number of collisions occurring in the target, multiple the intensity of the beam by the number of target particles. However, this assumes that all target particles undergo collisions. This is where the role of the cross section being a proportionality constant is derived. In short, microscopic cross section is defined as the probability for a particular nuclear interaction to take place, in terms of an effective target area defined by the target and incident particle [2].

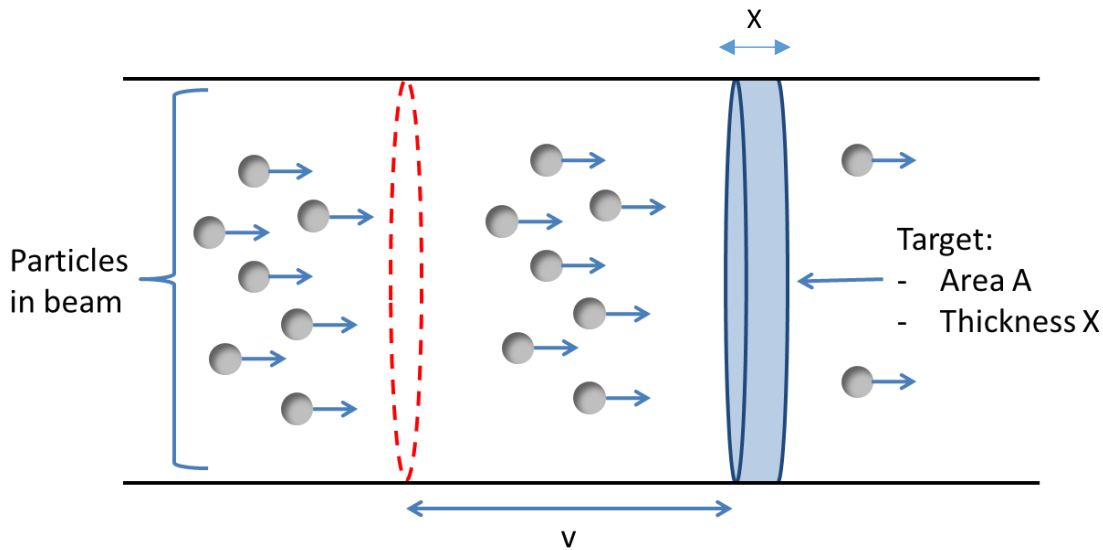


Figure 3.4: Schematic representation for the definition of cross section

### 3.5.2 Types of Cross Sections

As introduced in the previous subsection, particles interact with one another in a variety of ways. It is therefore convenient to describe each interaction with a representative cross section. For example, elastic and inelastic scattering interactions will have their own representative cross sections,  $\sigma_{elastic}$  and  $\sigma_{inelastic}$ , respectively. The sum of all cross-section forms for a nucleus is referred to as the total cross section, and represents the total probability of any type of interaction occurring between a given particle and nuclei [5]. The total cross section is given by:

$$\sigma_{total} = \sigma_{elastic} + \sigma_{inelastic} + \sigma_{fission} + \dots \quad 3.5.4$$

Similar to the total cross section but only summing cross sections of similar types leads to two cross section classes, scattering and absorption. With the sum of all cross sections relating to absorption reactions is called the absorption cross section, denoted by  $\sigma_a$ ,



$$\sigma_a = \sigma_c + \sigma_f + \dots \quad 3.5.5$$

where  $\sigma_c$  is the radiative capture cross section.

The scattering cross section,  $\sigma_s$ , is the sum of all cross sections for interactions where the form of the reactants and products remains unchanged [5]. This encompasses the elastic and inelastic scattering cross sections, and is given by,

$$\sigma_s = \sigma_{elastic} + \sigma_{inelastic} \quad 3.5.6$$

### 3.5.3 Macroscopic Cross Section

Aside from the microscopic cross section, there exists a second form of classification of cross section. This second classification relates to the cross section for the entirety of a target, instead of for a single target particle. Since this form of cross section relates to the target as a whole and not just a microscopic subsection, it is named the macroscopic cross section, and is denoted by,  $\Sigma$ . If the target has a given number of particles,  $N$ , per unit volume,  $m^3$ , then  $\Sigma$  is related to  $\sigma$  through the following equation,

$$\Sigma = N\sigma \quad 3.5.7$$

Similar to the definition of microscopic cross section, the definition of macroscopic cross section it is best understood by considering a hypothetical experiment. Therefore, consider a target of thickness  $X$ , again being placed in a mono-directional, mono-energetic neutron beam with an intensity of  $I_0$  [5]. By placing a neutron detector at some distance behind the target, the hypothetical experiment can be visualized in Figure 3.5,

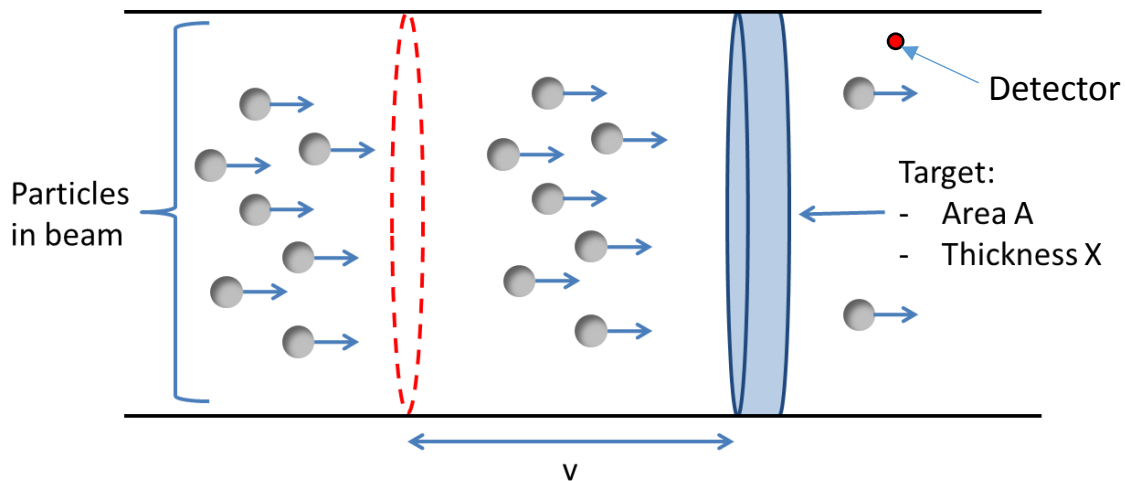


Figure 3.5: Measurement of neutron from a beam that passes through a target

As part of the hypothetical experiment, it is assumed the size of the detector is small when compared to the target. Having the detector being small means the detector subtends a small angle of the target. In this experimental configuration only neutrons which do not interact with the target will make it to the detector. Neutrons which do interact with the target are lost from the beam and scattered.

The intensity of the non-interacting neutrons after having penetrated the target a distance of  $x$  in the target, is defined as  $I(x)$ . If neutrons which have already penetrated a distance  $x$  now travel another small amount denoted  $dx$  through the target. Now consider the neutrons which have already penetrated a distance  $x$  through the target, travel an additional distance of  $dx$ . The intensity of the beam will decrease since more neutrons will have interact with the target within the distance  $dx$ . This decrease in intensity can be represented by the following equation,

$$-dI(x) = N\sigma_t I(x)dx \quad 3.5.8$$

where  $N$  is the atom density of the target material and  $\sigma_t$  is the total interaction cross section, and is in the equation since by definition any interaction will remove a neutron from the beam.

Equation 3.5.8 can be integrated to yield an equation for intensity as a function of distance,  $x$ . If the intensity of the non- interacted beam that emerges after traveling through the total thickness of the target,  $X$ , is of interest the differential equation is solved as,

$$I(X) = I_0 e^{-N\sigma_t X} \quad 3.5.9$$

As provided, the product of atom density and microscopic cross section is the macroscopic cross section. Macroscopic cross section is given its own title since the product of atom density and microscopic cross section is common throughout reactor theory. The dimensions of macroscopic cross sections are  $cm^{-1}$ . This arises from the fact that microscopic cross section has dimensions of  $cm^2$  and atom density has dimensions of  $atoms/cm^3$ .

Rewriting Equation 3.5.8 to include the definition of macroscopic cross section yields,

$$-dI(x) = \Sigma_t I(x)dx \quad 3.5.10$$

If both sides of Equation 3.5.10 are divided by  $I(x)$ , the equation becomes,

$$\frac{-dI(x)}{I(x)} = \Sigma_t dx \quad 3.5.11$$

The value on the left-hand side of Equation 3.5.11 can be considered as the probability that a neutron which did not interact in the distance  $x$  interact in the next  $dx$ . Since  $-dI(x)$  represents the decrease in intensity, defined in Equation 3.5.8, the left-hand side can be considered as a fraction of intensity decrease or decimal probability. Therefore, the right-hand side of Equation 3.5.11,  $\Sigma_t dx$ , is the probability that a neutron will interact within a distance of  $dx$ . Since cross sections are similar to probabilities in that they represent the chance of interactions in a given distance for a target material. Note that both the left- and right-hand sides are unitless.

Since  $\sigma_t$  is the total microscopic cross section,  $\Sigma_t$  is the total macroscopic cross section. The total macroscopic cross section is the probability per unit path length that a neutron undergoes some form of interaction with the target material [5].

### 3.5.4 Dependencies of Cross Sections

Since the macroscopic cross section is a product of atom density and microscopic cross section, it is easy to see that atom density of the target will have an impact on its value. If the target has a high atom density the chance of interaction increases, and so does the macroscopic cross section. Likewise, if the atom density is low the chance of interaction decreases, and so does the macroscopic cross section. When considering factors which affect the microscopic cross section, it is less straight-forward to make similar statements. The first and obvious factor would be the type of interaction, since there exist different cross sections depending on which type of interaction is taking place. Aside from the type of interaction, the energy of the target-particle system has an impact on the microscopic cross section [8] [9].

All materials can be divided into two different categories based on how their cross sections change with energy of incident particles. These two categories are the  $1/v$  and the non- $1/v$  absorbers, where  $v$  is the velocity of the incident particles. The classification of either  $1/v$ - or non- $1/v$  absorber depends solely upon how the cross-section changes with increasing the energy and therefore velocity of the incident particles.  $1/v$  absorbers will change according to the inverse of the incident particles velocity, while non- $1/v$  absorbers do not follow this trend but instead can behave in different manners such as displaying resonances. Resonance refers to a neutron energy at which the cross section is significantly larger than the overall trend, and is highlighted in Figure 3.6 [6].

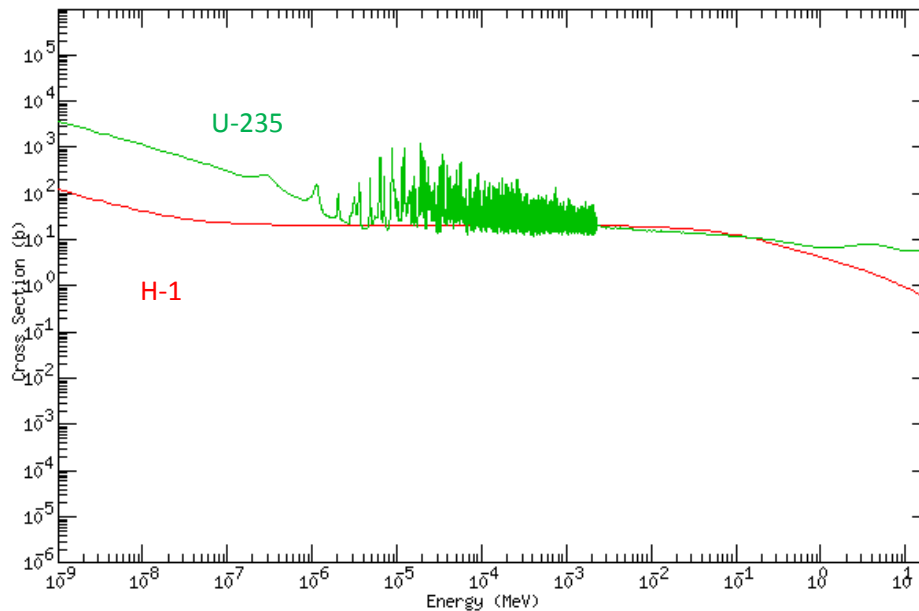


Figure 3.6:  $1/v$  vs. non- $1/v$  absorber, the green curve is the example non- $1/v$  absorber U-235 and the red curve is the example  $1/v$  curve H-1, from KAERI website

Depending on what type of absorber the target material is, the cross sections behaviour may be described by equations such as the following equations,

$$\sigma_x = \sigma_{x0} \sqrt{\frac{E_{293}}{E_T}} \quad (1/v \text{ absorber}) \quad 3.5.13$$

$$\sigma_x = \sigma_{x0} g(T) \sqrt{\frac{E_{293}}{E_T}} \quad (\text{Near-}1/v \text{ absorber}) \quad 3.5.14$$

where  $\sigma_x$  is the microscopic cross section for interaction type  $x$  post energy correction,  $\sigma_{x0}$  is the microscopic cross section for interaction type  $x$  prior to energy correction,  $E_{293}$  is the energy of the incident particle at room temperature, which is 293 K, and  $E_T$  is the energy of the incident particle at a temperature of  $T$ . The difference in energy correction between a  $1/v$  and non- $1/v$  absorber is the  $g(T)$  term, and is referred to as the Westcott factor. The Westcott factor is an empirical correction for absorbers which deviate from a  $1/v$  dependence in cross section [6].

### 3.6 Fuel Burnup Effects

As nuclear fuel undergoes fission in a reactor, the fuel is said to “burnup”, and the fuel composition changes [23]. The composition of the fuel changes through the production of fission products and the depletion of fissile and fissionable nuclides which compose the fuel through fission or converted to other nuclides through neutron capture [24]. This change of fuel composition has a direct effect on the reactivity of the reactor core. The primary mechanisms by which NU fuel undergoes changes are through the fission of U-235, which both depletes the fissile U-235 isotope and generates fission products. The second mechanism in which NU fuel undergoes changes is through the conversion of U-238 to the fissile Pu-239 and Pu-241, via a chain of neutron capture reactions and radioactive decays. Figure 3.7 shows how fissile plutonium isotopes are created from the fissionable U-238 [19] [20].

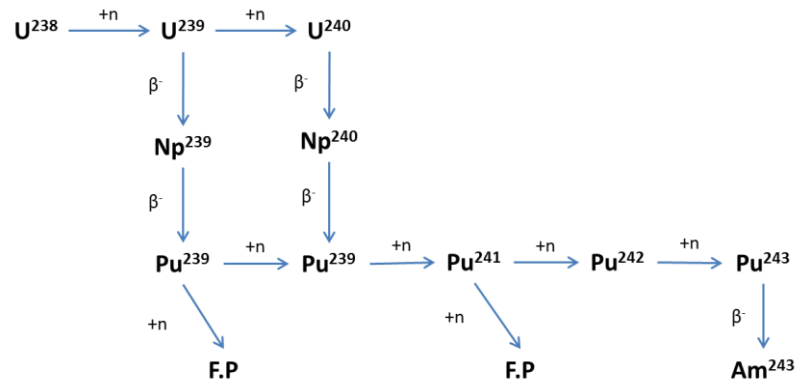


Figure 3.7 Typical decay chain for U-238 during reactor operation

The burnup directly affects the criticality of a reactor core, through the depletion of fissile isotopes which leads to a steady decrease of isotopes which readily produce energy [25]. The burnup also affects the criticality of the reactor, through the production of fission products and the conversion of fertile isotopes to fissile isotopes [26]. These two effects lead to criticality transients within a CANDU reactor. These two transients are referred to as the xenon or refuelling transient and plutonium peaking. These two transients are discussed in the following sub sections.

Both the refuelling transient and plutonium peak represent inconveniences for power compliance as they have effects on the current and adjacent channel powers, and can potentially place the channel power close to the operating limits [27].

### 3.6.1 Refuelling Transient

Since CANDU reactors can be re-fuelled while on-power, fresh fuel bundles added into the core will increase both the local flux and power density. This increase in flux and power density occur due to fresh fuel bundles being void of fission products and therefore replenish the fissile content of a reactor core. Therefore, when a fresh bundle is placed within the core it will have a positive effect on the reactivity, which leads to an increase in the criticality value of core. This positive effect on reactivity diminishes significantly in the first day of irradiation as fission products are generated from fission of U-235. This decrease following the positive insertion of reactivity from fresh fuel bundles is referred to as the refuelling transient and can be seen in Figure 3.8. Compared to the  $\text{UO}_2$  fuel fission products, such as xenon-135 and samarium-149, have relatively large thermal neutron absorption cross sections. This leads to the fission products absorbing neutrons which ideally would be absorbed by U-235 to undergo fission. Fission products can be divided into two separate categories, saturating and non-saturating. Saturating fission products equilibrate quickly, and contribute the most to the refuelling transient. Some examples of saturating fission products are xenon-135, samarium-149 and samarium-151. Non-saturating fission products on the other hand accumulate slower and build-up over time. It is the build-up of non-saturating fission products which will ultimately cause the core to become subcritical [28] [29] [30].

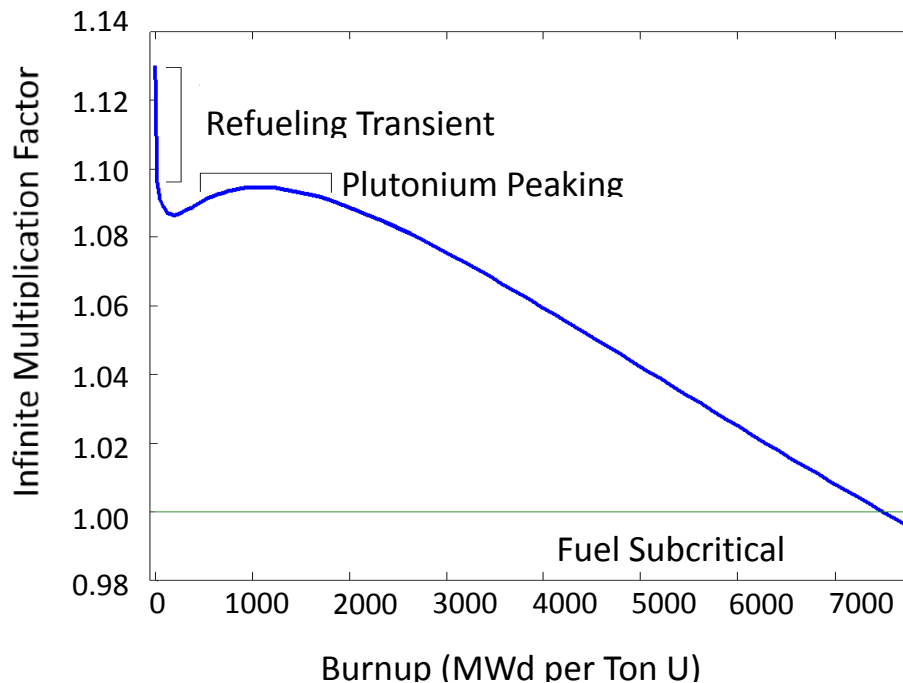


Figure 3.8: Reactivity in NU fuel in CANDU reactors during normal irradiation at constant flux level [4]

## 3.6.2 Plutonium Peaking

Plutonium peaking is directly related to the conversion of U-238 to fissile plutonium isotopes, as shown in Figure 3.8. This creation of plutonium occurs slowly during reactor operation and is at its highest concentration around 40 – 50 full-power days (FPD). The addition of more fissile isotopes contributes to an increase in reactivity, which leads to a peak in criticality around this time. During normal operating conditions the plutonium peak represents the time when the core criticality is at its highest, aside from the point of refuelling, this can be seen in Figure 3.8 [28] [29] [30].

## 3.7 Burnable Neutron Absorber

Burnable neutron absorbers have been used regularly within Light Water Reactors (LWR) for some time now, but their use has not been implemented in CANDU type reactors, due to the primary concern of their effect on neutron economy. An ideal burnable neutron absorber for CANDU application must be able to mitigate specific undesirable behaviours within the reactor, such as the transients described above, while having minimal effect on the neutron economy [28]. To be classified as a good absorber the material must have a large absorption cross section for thermal neutrons, compared to the fuel and structural materials of the fuel bundle. As the name, burnable neutron absorber, implies, the material must eventually burn-out of the reactor. This primarily occurs through the neutron capture reaction and subsequent decay, transforming the absorber isotopes into isotopes which have lower neutron absorption cross sections than the original material. The burn-out rate of a BNA is correlated to the absorption cross section of the material itself and that of the decay products that are produced through various nuclear interactions.

Since the main transients discussed above occur at different times, the absorber(s) must be potent at each stage of fuel burnup. In regards to plutonium peaking, since the effect isn't prominent until roughly 40 FPDs, a BNA must remain potent enough to mitigate the increase in reactivity from plutonium production. Whereas for the refuelling transient the BNA should be effective at the beginning of fuel burnup, but should burn-out as rapidly as the transient.

In *Chan et al.*, it was determined that gadolinium oxide ( $Gd_2O_3$ ) and europium oxide ( $Eu_2O_3$ ) meet the criteria discussed above. The BNAs are chosen in their oxide form, as to make them compatible with the uranium oxide fuel pellet material in CANDU design. Europium and gadolinium were chosen as BNA candidates because they both have large neutron absorption cross sections relative to the natural uranium fuel. Gadolinium has the largest absorption cross section of any element and therefore will burn-out very quickly. In comparison, the absorption cross section of europium is roughly a factor of one tenth that of gadolinium. Some properties of interest for both gadolinium and europium isotopes are shown in Table 3.2.

Using these two absorbers it was concluded by *Chan et al.* that ~180mg of  $Gd_2O_3$  and ~1000 mg of  $Eu_2O_3$  within a fuel bundle can suppress both the refuelling transient and lower the plutonium peak. The combined mass of the absorbers, ~180mg of  $Gd_2O_3$  plus ~1000 mg of  $Eu_2O_3$  equalling 1180 mg of absorbing material, added to the total mass of the fuel bundle, roughly 24-kg, is on the order of  $\sim 10^{-3}$  weight % , [30]. This will provide an upper limit on the amount of absorber that can be added into the fuel bundle to mitigate end flux peaking.

Table 3.2: Properties of burnable neutron absorbers candidates

Isotope	Molar Mass (g mol <sup>-1</sup> )	Half-Life	Abundance (atom %)	Thermal $\sigma_a$ (barns)
<i>Gd-152</i>	151.9197879	1.08 x 10 <sup>14</sup> y	0.20	1056
<i>Gd-153</i>	152.9217580	240.4 d	0.0	22455
<i>Gd-154</i>	153.9208623	Stable	2.18	84.99
<i>Gd-155</i>	154.9226188	Stable	14.80	60 889
<i>Gd-156</i>	155.9221196	Stable	20.47	2.188
<i>Gd-157</i>	156.9239567	Stable	15.65	254 078
<i>Gd-158</i>	157.9241005	Stable	24.84	2.496
<i>Gd-159</i>	158.9263970	18.479 hr	0.0	N/A
<i>Gd-160</i>	159.9270506	Stable	21.86	0.7981
<i>Gd-161</i>	160.9296775	3.646 m	0.0	16319
<i>Natural Gd</i>	157.2521		100	48 780
<i>Eu-151</i>	150.919846	Stable	47.8	9198
<i>Eu-152</i>	151.921752	13.537 y	0.0	12819
<i>Eu-153</i>	152.921226	Stable	52.2	312.7
<i>Eu-154</i>	153.922987	8.601 y	0.0	1348.5
<i>Natural Eu</i>	151.9645665		100	4559.8

Note the rows which contain red text indicate an isotope of either BNA candidate that is not naturally occurring.

As shown in the table, the absorption cross sections of the gadolinium isotopes largely vary, by several orders of magnitude. This is a beneficial quality in the candidacy of gadolinium as a BNA, since having a large absorption cross section and variability between different isotopes means that it will burn-out quickly and the resulting daughter isotopes will have a lower absorption cross section than the original material. In fact, the burn-out rate of gadolinium is close to the build-up rate of the fission products which lead to the refuelling transient. Therefore, gadolinium in its oxide form provides an ideal BNA candidate to mitigate the refuelling transient.

In contrast the difference in absorption cross section for the two naturally occurring europium isotopes is only a single order of magnitude. Also, the absorption cross section of the daughter isotopes remains within the same order of magnitude as the original material. This means europium as a BNA, will remain in the reactor core for a longer duration than gadolinium, while keeping roughly the same degree of neutron absorption potential as the initial material. Therefore, europium in its oxide form provides an excellent BNA candidate to mitigate the plutonium peaking transient, due to its ability to retain neutron absorption potential over long periods of reactor operation.

### 3.8 End Flux Peaking

The primary cause of end flux peaking (EFP) is a discontinuity in absorption cross section of the uranium dioxide fuel, heavy-water moderator and Zircaloy structural components [31]. Since the thermal neutron absorption cross section of the heavy-water and Zircaloy components is significantly lower than that of the  $\text{UO}_2$  fuel, more thermal neutrons are able to pass through these materials, leading to an increase in thermal flux in the end regions [32]. In Figure 3.9, a demonstration of thermal neutrons passing through the end region is shown. The coloured curves in the figure are included to provide an indication of how large the neutron flux peaks in the end region [33]. Each colour represents a separate ring in the fuel bundle. The blue curve represents EFP in the center element, the red curve represents EFP in the fuel elements of the inner ring, the green curve represents EFP in the fuel elements of the intermediate ring and the yellow curve represents EFP in the fuel elements of the outer ring.

As shown in Figure 3.9, the thermal neutron flux peaks differ depending on the fuel ring in which a fuel element resides [34] [35]. This difference in flux peak arises from the fact the thermal neutron flux is larger in the outer elements and decreases in a cosine fashion the closer to the center of the fuel bundle an element is. This shape in radial thermal neutron flux arises from the fact that thermal neutrons must penetrate three fuel rings before making it to the center element. Therefore, the probability that a thermal neutron is absorbed, increases with the amount of material it passes through.

Figure 3.9 depicts the EFP phenomenon in fuel elements from each fuel ring. Note that the flux curve peaks the most in the center element and fuel elements in the inner ring, as shown by the black and red curves in Figure 3.9 respectively. An image of two half-fuel bundles is superimposed on the graph to demonstrate the flux curve reaching a maximum at the location where the two bundles meet. Note the red box is included to demonstrate the area of concern of EFP, within the fuel pellets adjacent to the end region.



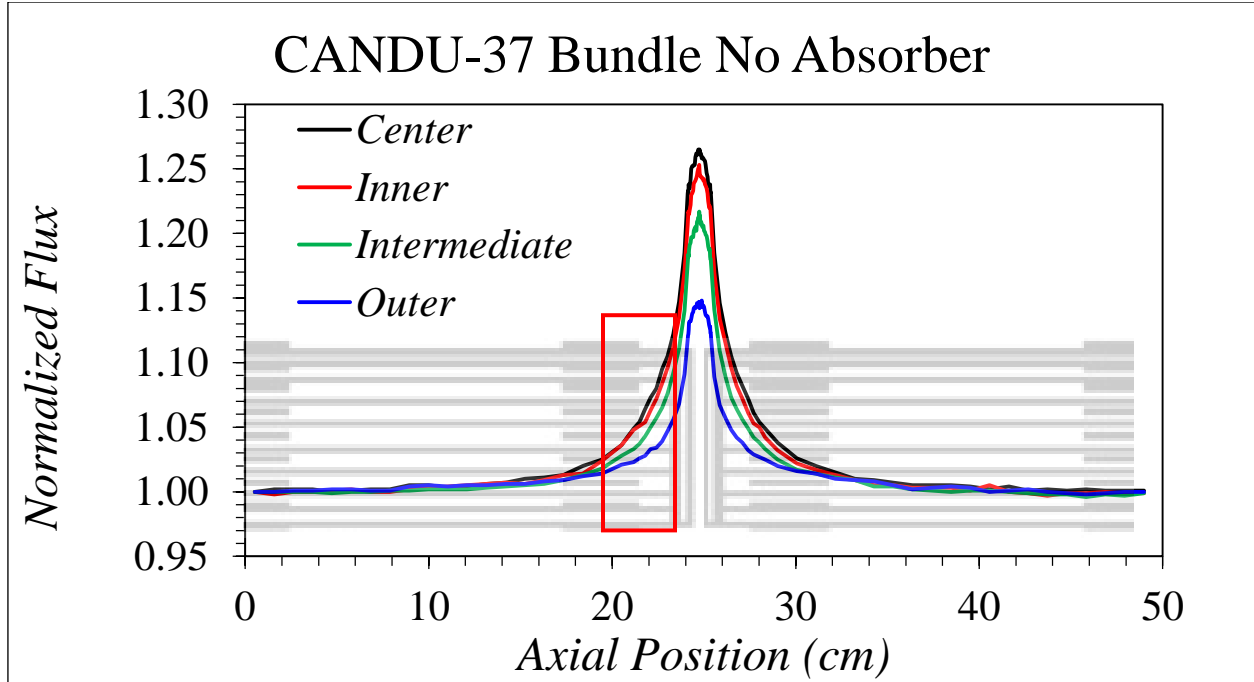


Figure 3.9: Illustration of End Flux Peaking

To quantify the phenomenon of EFP, an end flux peaking factor,  $PF^{flux}$ , is used. The end flux peaking factor is the ratio of the neutron flux in the end regions of the bundle to the neutron flux within the mid plane of the bundle.  $PF^{flux}$  is defined for a single element in each element ring, and, as discussed, the value of peaking is dependent upon which fuel ring an element exists [31].

$$PF^{flux} = \frac{\phi^{end}}{\phi^{mid\ plane}} \quad 3.8.1$$

### 3.9 Fuel Bundle Radial Power Peaking Factor

The Radial Power Peaking Factor (RPPF) is another means of characterizing a fuel element aside from EFP. The RPPF is a ratio of the average element power to the power of a given element in a CANDU fuel bundle. The determination of RPPF not only is an indication of a fuel elements power but also the neutron flux, since the power and the flux are proportional. To calculate the RPPF of a fuel element simply apply the following equation,

$$F_f = \frac{E_{FD}}{\bar{E}_E} \quad 3.9.1$$

where,  $E_{FD}$  is the maximum fission energy deposited in a single element and  $\bar{E}_E$  is the average element energy, in units of Mega Electron-Volts (MeV). The fission energy deposited in a single element can be easily determined from the MCNP code using the output provided by the F7 tally. As the F7 tally

provides the fission energy deposited in a given mass of material. Tallies in MCNP will be discussed in a later chapter.

Since the value of an F7 tally is mass dependent, it first must be converted to fission energy using,

$$E_{FD} = E_{FM} \times M_C \quad 3.9.2$$

Here  $E_{FM}$  is the fission energy deposited in a given mass of material, from the F7 tally output, and has units of Mega Electron-Volts per gram (MeV/g), and  $M_C$  is the mass of the given material for which the F7 tally is applied to, in units of grams (g).

Once the fission energy deposited is determined, the average element energy must be calculated. To find the average element energy, take the sum of the fission energy deposited in all fuel elements within a fuel bundle and then divide by the total number of fuel elements in the fuel bundle. The total number of elements is 37 for a CANDU fuel bundle. The average element energy is therefore given by,

$$\bar{E}_E = E_B/37 \quad 3.9.3$$

where  $E_B$  is the total bundle energy. This can be given by,

$$E_B = E_{FC} + E_{FIN} + E_{FIT} + E_{FOU} \quad 3.9.4$$

where  $E_{FC}$ ,  $E_{FIN}$ ,  $E_{FIT}$ , and  $E_{FOU}$  are the total fission energy in the center, inner, intermediate and outer rings respectively.

## 3.10 The Neutron Transport Equation

### 3.10.1 Introduction

The behaviour of a reactor is governed by a distribution which is dependent on space, time, and energy of the neutrons present in the system. One must define a distribution which is able to predict the correct behaviour for each dependent variable. Defining a distribution is not an easy task since reactors tend to be extremely complex and are heterogeneous systems. This section will attempt to provide a simple introduction and derivation of the neutron transport equation, an equation which strives to represent the behaviour of neutrons in reactor systems.

### 3.10.2 Neutron as a Point Particle

As mentioned, the derivation of an equation which describes a system that is inherently complex and heterogeneous is not an easy task. To simplify the derivation, transport theory is used and assumes

that neutrons are considered to be point particles [36]. This means that the position and velocity of a neutron provides a complete description of the neutron in the system. The condition, which indicates that a point particle approximation is valid for a neutron, is related to the comparison of the neutron's reduced wavelength compared to its macroscopic dimensions and mean free path as being small [5]. To obtain an estimate of the reduced wavelength of a neutron, use the de Broglie equation for wavelength, as provided below,

$$\lambda = \hbar/p \quad 3.10.1$$

where  $\hbar$  is Planck's constant divided by  $2\pi$ , and is given by  $\hbar = 6.62606957 \times 10^{-34} \text{ J} \cdot \text{s}$ , and  $p$  is the momentum, in  $\text{kg m s}^{-1}$ , of the particle. For a neutron, this equation becomes,

$$\lambda = \frac{4.55 \times 10^{-10}}{\sqrt{E}} \text{ cm} \quad 3.10.2$$

where  $E$  is the energy of the neutron in units of electron Volt (eV).

Of greatest interest to CANDU reactors are neutrons whose energies fall within the thermal energy group regime. For example, thermal neutrons have an energy of roughly 0.01 eV. Using this energy estimate for a thermal neutron and Equation 3.10.2, the reduced wavelength of the thermal neutron is roughly,  $4.55 \times 10^{-11} \text{ m}$ . This value of reduced wavelength is roughly an order of magnitude less than the average distance between the atoms in a solid, which is on the order of tenths of angstroms ( $10^{-10} \text{ m}$ ). Based on the assumptions thus far, this indicates that the position of a neutron is a quantity with a relatively high degree of accuracy. The high degree of accuracy of a neutron's position is due to the small relative wavelength. This means the position and velocity (or momentum) of a neutron can be determined to sufficient accuracy while not violating the Heisenberg's uncertainty principle [5], which is provided by the following equation:

$$\Delta x \Delta p \cong \hbar \quad 3.10.3$$

where  $\Delta x$ , is the uncertainty of a particle's position and  $\Delta p$ , is the uncertainty of a particle's momentum.

The Heisenberg's uncertainty principle is a relationship derived from quantum mechanics, which provides a limitation on how well the position and momentum of a particle can be known. The relationship indicates that if the position of a particle is known extremely well, then the particle's momentum is not well characterized, and vice versa [10] [12] [13].

For the case of a thermal neutron, assuming an uncertainty in the position of roughly,  $\Delta x = 10^{-4} \text{ cm}$ , can be tolerated in the calculations, then the uncertainty in the neutron momentum corresponds to an uncertainty in the energy given by,

$$\Delta E \cong 10^{-5} / \sqrt{E} \quad 3.10.4$$

where  $\Delta E$  and  $E$  have units of eV.

From Equation 3.10.4, neutrons with low energies have large wavelengths due to the dependence of the equation on  $E^{-1/2}$ . The large wavelengths indicate that an accurate spatial description cannot be provided for low-energy neutrons. Therefore, to explain low-energy neutron behaviour with a high degree of accuracy some form of quantum mechanical formulation is necessary. Fortunately, low-energy neutron behaviour does not play a huge role when dealing with reactor systems. This minimal impact on reactor systems is due to reactors seldom having neutrons of low enough energy to cause a significant

error to arise from the use of a point-like neutron approximation. It however is useful to understand the limitations of these assumptions when trying to characterize reactor systems [10] [12] [13].

Other characteristics of neutrons that must be taken into consideration when accurately describing their behaviour in reactor systems are the spin and the magnetic moments. Both the spin and the magnetic moment are quantities intrinsic to all particles used to distinguish between various particles. Even though a neutron has a neutral electrical charge it still possesses a magnetic moment. Both the spin and the magnetic moment can lead to polarization and therefore can affect the neutron as it moves through a reactor. The effects of the spin and the magnetic moment are most significant to the values of the scattering cross sections. However, these effects are considered to be negligible in most practical cases, as they do not contribute significantly to the overall result.

In this work, the neutrons will be considered point-like particles. Therefore, the neutrons within a reactor are described by a position, given by a vector  $\vec{r}$  and a velocity given by the vector  $\vec{v}$ . The velocity vector is provided by,

$$\vec{v} = v\vec{\Omega} \quad 3.10.5$$

where  $v$  is the magnitude of the vector  $\vec{v}$ , and is known as the speed of the neutron, and  $\vec{\Omega}$  is a unit vector in the direction of motion of the neutron. It is convenient to represent the unit vector  $\vec{\Omega}$  in polar coordinates. Consider  $\theta$  to be the polar angle and  $\phi$  to be the azimuthal angle, as shown in Figure 3.10. The Cartesian coordinates of  $\vec{\Omega}$  are given by:

$$\Omega_x = \sin\theta \cos\phi \quad 3.10.6$$

$$\Omega_y = \sin\theta \sin\phi \quad 3.10.7$$

$$\Omega_z = \cos\theta \quad 3.10.8$$

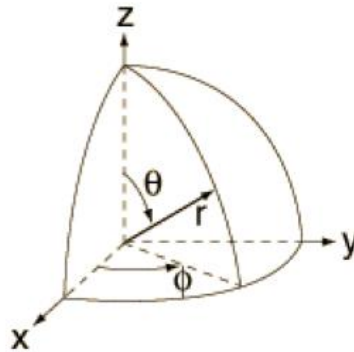


Figure 3.10: Polar Coordinate representation of point-like neutron courtesy of HyperPhysics webpage on Spherical Polar Coordinates (<http://hyperphysics.phy-astr.gsu.edu/hbase/sphc.html>)

### 3.10.3 Neutron Density and Flux

The neutron density or neutron angular density is a quantity which describes a population of neutrons and is given by the following equation,

$$\text{Angular Density} = N(\vec{r}, \vec{\Omega}, E, t) \quad 3.10.9$$

The neutron angular density is defined as the expected number of neutrons at a position  $\vec{r}$ , travelling in a direction  $\vec{\Omega}$  and having an energy  $E$  at time  $t$ , per unit volume, unit solid angle and unit energy. This in terms of actual units is, per  $\text{cm}^3$  per steradian per MeV. Therefore, Equation 3.10.10,

$$N(\vec{r}, \vec{\Omega}, E, t) dV d\vec{\Omega} dE \quad 3.10.10$$

is the expected number of neutrons in volume  $dV$  about position vector  $\vec{r}$ , with directions between  $d\vec{\Omega}$  about  $\vec{\Omega}$  as shown in Figure 3.11. The neutrons described by the above equation have energies within  $dE$  about  $E$  at time  $t$ . If  $\vec{\Omega}$  is expressed in polar coordinate then,  $d\vec{\Omega} = \sin\theta d\theta d\phi$ , where  $d\vec{\Omega}$  is described within the ranges of  $(\theta, \theta + d\theta)$  and  $(\phi, \phi + d\phi)$ . Often  $\cos\theta$  is represented by  $\mu$ . Making this transformation leads to Equation 3.10.11,

$$d\vec{\Omega} = d\mu d\phi, \quad 3.10.11$$

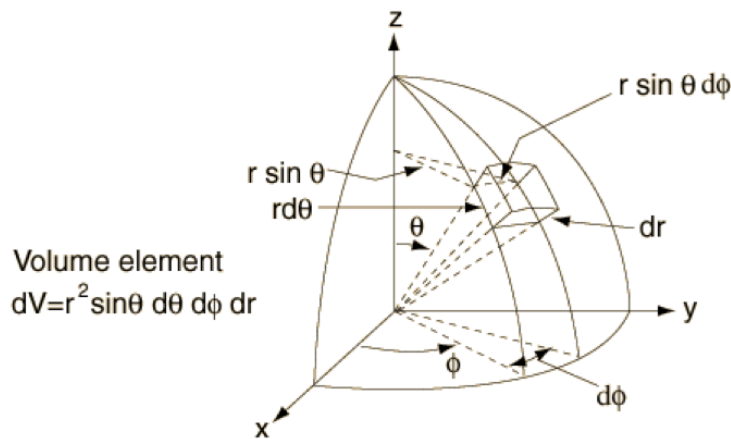


Figure 3.11: Representation of the volume element  $dV$ , image courtesy of HyperPhysics webpage on Spherical Polar Coordinates (<http://hyperphysics.phy-astr.gsu.edu/hbase/sphc.html>)

Up to this point considerations have not been made to account for fluctuations from the mean neutron population. Neutron population refers to the collective neutrons within the reactor, with mean neutron population being the time-averaged neutron population. If the neutron population is large and fluctuations in neutron population are small, the actual population at any given time in the system will be close to the average value. Conversely, if the neutron population is small and fluctuations are also small, then at any point in time the system is unlikely to resemble that of the average. From this point forward, the neutron population will be considered large such that small fluctuations do not adversely affect the overall result.

Taking the integral of the neutron angular density over all possible directions and solid angles, provides the energy-dependent neutron density, given by,

$$\text{Neutron Density} \equiv n(\vec{r}, E, t) = \int_{4\pi} N(\vec{r}, \vec{\Omega}, E, t) d\vec{\Omega} \quad 3.10.12$$

where the  $4\pi$  in the integral signifies that the integration is performed over all possible directions. The neutron density described by the above equation is defined as the expected number of neutrons at  $\vec{r}$  with energy  $E$ , at time  $t$  per unit volume and unit energy. Replacing  $\vec{\Omega}$  with polar coordinate representations, the equation for neutron density becomes,

$$n(\vec{r}, E, t) = \int_{-1}^1 \int_0^{2\pi} N(\vec{r}, \vec{\Omega}, E, t) d\mu d\varphi \quad 3.10.13$$

using the relation that  $\mu = \cos\theta$ .

Taking the product of the velocity and the neutron angular density provides an equation for the neutron angular current or the vector flux, given by,

$$\text{Vector flux} = \vec{v}N(\vec{r}, \vec{\Omega}, E, t) \quad 3.10.14$$

The neutron angular current is a vector function which is dependent upon four variables,  $\vec{r}$ ,  $\vec{\Omega}$ ,  $E$  and  $t$ . The magnitude of the neutron angular current,  $vN(\vec{r}, \vec{\Omega}, E, t)$ , is known as the scalar flux or neutron angular flux, and is denoted,

$$\text{Angular flux} \equiv \Phi(\vec{r}, \vec{\Omega}, E, t) = vN(\vec{r}, \vec{\Omega}, E, t) \quad 3.10.15$$

Integrating the angular flux over all directions, provides the total flux, given by,

$$\text{Total flux} \equiv \phi(\vec{r}, E, t) = vN(\vec{r}, E, t) = \int_{4\pi} \Phi(\vec{r}, \vec{\Omega}, E, t) d\vec{\Omega} \quad 3.10.16$$

The total flux is therefore just the flux of neutrons with an energy of  $E$  at position  $\vec{r}$  and time  $t$  per unit energy. The total flux is often referred to as just the neutron flux [10] [12] [13].

# Chapter 4: Methodology

## 4.1 Monte Carlo Method

The term Monte Carlo applies to all numerical methods that make use of random sampling techniques [7]. The calculations performed by Monte Carlo type methods are structured in a sequence of states that are determined by random events [8]. All Monte Carlo simulations apply a similar basic process to solve problems. The first step in this process is to define the domain for possible inputs, and instructions into the algorithm. The second step in this process is to generate inputs randomly from a given probability distribution which has been defined over the domain from the first step of the process. The third step is to perform the calculation on the inputs and keep track of intermediate results, collecting and outputting results once all intermediates have been calculated [37]-[46].

## 4.2 Monte Carlo N-Particle (MCNP) Transport Code

### 4.2.1 Introduction

The Monte Carlo N-Particle (MCNP) Transport code is a general-purpose Monte Carlo transport code that has the capability of handling the transport of neutrons, photons, electrons as well as the coupling between various particles. This includes the capability of selecting which transport mode will be used from a list of given modes. These modes include: neutron only, photon only, electron only, combined neutron/photon transport where the photons are generated by neutron interactions, neutron/electron/photon, and photon/electron or electron/photon. For transport modes including neutron interactions, the neutron energy regime included in MCNP goes from  $10^{-11}$  MeV to 20 MeV for all isotopes included in their libraries. Some specific isotopes in the libraries have ranges which extend up to 150 MeV. The energy regime for photon transport runs from 1keV to 100 GeV, and for electron transport the energy regime goes from 1keV to 1 GeV [47] [48] [49] [50].

MCNP is developed and maintained by the Los Alamos National Laboratories (LANL). MCNP is particularly useful for reactor systems as it contains functionality to calculate eigenvalues of critical systems. This functionality includes the calculation of  $k_{\text{eff}}$  for fissile systems. Another benefit of MCNP is that it has the ability to analyze systems in three dimensions, this gives a more accurate representation of the overall system trying to be modelled in the simulation [51].

MCNP uses pointwise cross-sectional data, utilizing libraries such as the Evaluated Nuclear Data Files (ENDF)/B-VI for this purpose. For thermal neutrons, MCNP includes specific models such as the free gas and the  $S(\alpha,\beta)$ , for more accurate results. Models for photon transport in MCNP include the following but are not limited to: incoherent and coherent scattering, fluorescent emission after photoelectric absorption, and absorption through electron-positron pair production. For the transport of electrons and positrons the following physical processes are included: angular deflection through multiple Compton scattering, collisional energy loss, production of secondaries including K x-rays, knock-on and Auger electrons, bremsstrahlung, and annihilation gammas from electron-positron annihilation [51].

To create a simulation in MCNP, the user creates an input file, referred to as an input deck that is then read by MCNP. The user must provide the following information about the system they are trying to model;

- the geometry specification of the system,
- the description of the materials within the specified geometry as well as the selection of cross-section evaluations,
- the location of the nuclear source in the problem (neutron, photon, electron or isotopic source),
- which information the user wishes to obtain as output from the simulation,
- and any variance reduction techniques which is used to improve the efficiency of the simulation

The goal of Section 4.2 is to provide the reader with a general understanding of how MCNP performs its calculations as well as how to generate an input deck [52].

## 4.2.2 Surfaces

This section is included to provide a brief overview on how problem geometries are defined in MCNP. MCNP treats user defined geometries as three-dimensional cells of user defined-materials which are bound by first- and second-dimensional surfaces. Cells are described through the use of Boolean operations, intersections, unions, and complements, for regions bound by surfaces [53]. Surfaces in MCNP are defined by user supplied coefficients to a list of analytic surface equations provided by MCNP. An example of an analytic surface equation is provided in Appendix A.1, while an example of a surface card is provided below,

<i>Surface Number</i>	<i>Surface Mnemonic</i>	<i>Surface Card Entry</i>
<i>1</i>	<i>PZ</i>	<i>-5</i>

MCNP also allows the user to define a surface as reflective. To specify a reflective surface an asterisk must precede the surface number. If a particle hits a reflecting surface is reflected as if it is the mirror image of the incident particle.

MCNP also provides the user with “macrobody”, which are basic three-dimensional shapes such as spheres, boxes, cylinders, etc. Similar to one- or two-dimensional surfaces, macrobodies may be combined using Boolean operators. The main purpose of surfaces in MCNP is to provide boundaries to which cells are being described [51] [52] [53].

## 4.2.3 Cells

Similar to surfaces, cells have their own section within the input deck, referred to as the cell card section. To define a cell, the user must define, a cell number, a material number and a material density in  $\text{g/cm}^3$ , which is then followed by a list of surfaces and operators which define the outer boundaries of the cell. If a cell contains no material, instead of defining a material number and density, one could simply use a single zero. MCNP has the restriction that the cell number must occur within columns 1 to 5. The following entries are filled in and separated by blank spaces. A description of a cell card is as follows,



<i>Cell Number</i>	<i>Material Number</i>	<i>Material Density</i>	<i>Surface Number(s) and Operator(s)</i>	<i>Cell Parameters</i>
1	1	-0.0014	-7	IMP:N=1

The user can also define certain cell parameters after the list of surfaces and operators section of a cell card. One of these parameters defines whether a cell can have a particle transport through it, for example in the above cell card IMP:N=1 means that neutrons can pass through the defined cell. Conversely if IMP:N=0 then neutrons would not be able to transport through the defined cell. Other types of cell parameters include: temperature of the material bound within the cell and the functionality to group various cells into one structure.

An important concept when constructing cells in MCNP is the “sense of points” within or outside a cell with respect to a bounding surface. To understand the concept of sense, one may consider the equation of a surface or macrobody defined by the user as  $s = f(x, y, z) = 0$ . For any point  $(x, y, z)$ , we have the following relations for  $s$ : if  $s = 0$ , then the point is on the surface; if  $s$  is negative, the point is said to have a “negative sense” or inside the surface; and if  $s$  is positive then the point is said to have a positive sense or outside the surface [51] [52]. See the following for examples.

Example: Surface Sense in defining cells

From Appendix A.1, use the equation for a sphere at the origin with the radius  $R = 3.0$ ,

$$x^2 + y^2 + z^2 - R^2 = S \tag{4.2.1}$$

This will generate a sphere situated around the origin with a radius of 3.0. The base unit of distance in MCNP is centimeters so the radius of the sphere is 3.0 cm.

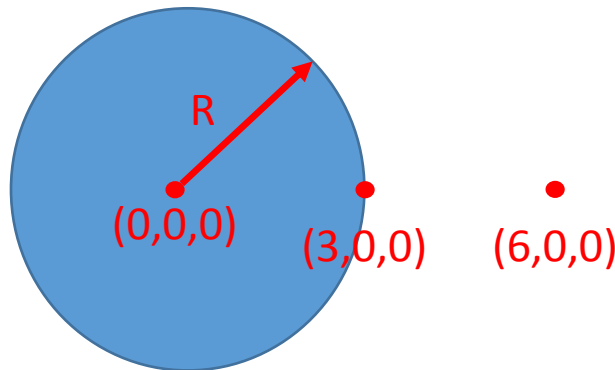


Figure 4.1: 2D cross section of sphere centered at origin with 3.0 cm radius

Now consider the following cases,

- Substitute (0, 0, 0) for (x, y, z),

$$0^2 + 0^2 + 0^2 - 3^2 = \textit{negative} \tag{4.2.2}$$

This gives a negative S, therefore this point occurs within the sphere since it has a negative sense

- Substitute (3, 0, 0) for (x, y, z),

$$3^2 + 0^2 + 0^2 - 3^2 = 0 \quad 4.2.3$$

This gives  $S = 0$ , therefore this point occurs on the surface of the sphere

- Substitute (6, 0, 0) for (x, y, z),

$$6^2 + 0^2 + 0^2 - 3^2 = \textit{positive} \quad 4.2.4$$

This gives a positive  $S$ , therefore this point occurs outside the sphere since it has a positive sense

Once all the cell parameters are defined for a particular cell, MCNP places the cell into an arbitrary Cartesian coordinate system, also defined by the user. Through the use of the bounding surfaces defined by the cell cards, MCNP is able to track particles as they travel through the user-defined geometry [51] [52].

## 4.2.4 Nuclear Information and Reactions

To generate accurate results, MCNP makes use of nuclear and atomic data libraries which are continuous in regards to energy. These nuclear and atomic data are produced by the following sources; Evaluated Nuclear Data File (ENDF) system, Advanced Computational Technology Initiative (ACTI), the Evaluated Nuclear Data Library (ENDL), Evaluated Photon Data Library (EPDL), the Activation Library (ACTL) compilations from Livermore, and evaluations from the Nuclear Physics (T-16) Group from Los Alamos National Laboratories (LANL). MCNP users have the ability to select a specific data table through the use of a unique identifier for each table. These identifiers are known as ZAIDs. In the term ZAID, Z indicates the particles atomic number, A indicates the particle mass number and ID is the specific data table selector. ZAIDs are formatted as ZZZAAA.abx, where ZZZ is the atomic number, AAA the mass number and abx is the optional library identifier. The optional library identifier is used to specify the conditions that the material is subject too. This includes temperatures and pressures. For the models used in this project, the optional library identifiers were used to simulate fresh fuel conditions.

Of particular interest to reactor physicists is the data table for neutron interactions. Through the use of the above sources, MCNP has access to over 836 neutron interaction tables and approximately 100 different data tables for isotopes and elements. Since there exists so many sources for which data could be extracted, multiple tables for a single isotope are provided. Having multiple tables for a single isotope is beneficial, because it provides the user access to information across larger temperature and processing tolerance regimes than if the data were provided by a single source.

Data tables for various important nuclear materials are also provided to the user. These materials include light and heavy water used as moderator and coolant, beryllium metal and oxide used as reflector and poisons, benzene, graphite, polyethylene, zirconium and hydrogen in zirconium hydride used in the structural components of a fuel bundle.

For photon interactions, data tables exist for all elements with atomic numbers from 1 to 100. These data tables allow MCNP to account for many photonic processes. These processes include; coherent and incoherent scattering, photoelectric absorption and pair production. Thermal neutron data tables are used with the  $S(\alpha,\beta)$  scattering treatment in MCNP. These thermal neutron data tables include chemical (molecular) binding and crystalline effects that are necessary when the energy of the neutron becomes sufficiently low. Like all other neutron data tables, the thermal neutron data tables include temperature dependence for materials of importance to reactor simulations [51].

## 4.2.5 Cross Sections

MCNP has nine classes of cross section data tables,

- (1) Continuous-energy neutron interaction data
- (2) Discrete reaction neutron interaction data
- (3) Continuous-energy photo-atomic interaction data
- (4) Continuous-energy photonuclear interaction data
- (5) Neutron dosimetry cross sections
- (6) Neutron  $S(\alpha,\beta)$  thermal data
- (7) Multi-group neutron, coupled neutron/photon, and charged particles masquerading as neutrons
- (8) Multi-group photon
- (9) Electron interaction data

Of particular interest to reactor physics and neutronics are the continuous- and discrete-energy neutron interaction data and the neutron  $S(\alpha,\beta)$  thermal data. The reasons will be explained in the following sub-sections.

Cross sections and emission distributions for secondary particles and angular distribution for neutron (and photonuclear) collisions are included in the cross-section data sets in MCNP. These angular distributions are typically provided in the center-of-mass frame for both elastic and inelastic scattering. The angle of scattering is important since it uniquely determines the energy of the secondary particles generated in both forms of scattering. If photons are generated as secondaries in a neutron interaction, all the photon interaction data are included in the neutron data tables. The secondary photon interaction data include production cross sections, angular distributions and energy distributions.

Other information of importance to neutron interactions included in these neutron interaction data tables is the atomic weight ratio of the target nucleus, and the Q-value of each reaction. The average number of neutrons per fission ( $\bar{\nu}$ ) includes both prompt and delayed neutrons [51].

### 4.2.5.1 Continuous-Energy and Discrete-Reaction

When the user is concerned about neutron interactions in his or her problem, one neutron interaction table is required for each isotope. The form of the ZAIDs in this case are either `ZZZAAA.nnC` for a continuous-energy table or `ZZZAAA.nnD` for a discrete reaction table. The `nn` in the ZAIDs

represents the value for the corresponding cross section data set. To produce one of these cross-section data sets, experimental analyses of measured cross sections are combined with data predictions from nuclear model calculations. This is done to obtain the most accurate description of the interaction.

The only difference between the discrete-reaction and continuous-energy tables is that discrete-reaction tables have cross sections which are averaged in 262 groups. This averaging is done with a flat weighting function and generates cross sections which are essentially represented by a histogram instead of a continuous curve. All of the other information included in the interaction data tables (angular and energy distributions, Q-value, etc.) are identical between the discrete-reaction and continuous-energy tables. The benefit of using a discrete-reaction table is that the required data storage for these tables is much smaller than the continuous-energy tables, and thus enhances MCNP's ability to run on smaller computers. It is advised that discrete-reaction tables be avoided since they are less accurate than the continuous-energy interaction tables and represent another source of error in the user's simulation [51].

To select the appropriate neutron interaction table for the problem defined by the user, MCNP provides the following guidelines and observations to be taken into consideration before making a selection,

1. Use the most recent data available;
2. Check the sensitivity of the results to various sets of nuclear data;
3. Consider differences in evaluators' philosophies;
4. Be aware of the neutron energy spectrum in the defined problem;
5. Check the temperature at which various tables have been processed;
6. For coupled neutron/photon problems, ensure the table chosen has photon production data available;
7. Be aware of slight differences in series which differ by a few numbers, ie. Difference between “.50c” and “.51c”; and
8. Use the best data available.

#### 4.2.5.2 Neutron Thermal $S(\alpha,\beta)$ Tables

In most problems, the  $S(\alpha,\beta)$  tables are not necessary but become absolutely essential in problems where the user is concerned about the behaviour of thermal neutrons. For thermal neutrons in inelastic collisions,  $S(\alpha,\beta)$  tables provide correlated energy-angle distributions. However, for elastic collisions involving thermal neutrons, the  $S(\alpha,\beta)$  tables do not always provide these types of correlated distributions. Instead, the data are usually determined from either an incoherent or coherent approximation. In the incoherent approximation, scattering cosines, angles at which the incident neutron is reflected, are calculated for several incident neutron energies. For the coherent approximation scattering, the cosines are calculated from a set of Bragg energies derived from lattice parameters, using Bragg's law.

The form in which the  $S(\alpha,\beta)$  tables are called is XXXXXX.nnT, where XXXXXX is a mnemonic character string, corresponding to an isotope or material defined in the MCNP libraries. The  $S(\alpha,\beta)$  tables include all the data necessary to completely characterize the thermal neutron scattering [51].

## 4.2.6 Source Specification

In MCNP the user is capable of defining the source under a wide variety of source conditions, which can be edited by the user and include probability distributions for the following variables; energy, time, position and directions, as well as which cell or surface the source applies to. This capability is important since it allows the user to tailor the source term to meet the requirements of their problem without having to edit the code itself. Aside from the ability to fully define arbitrary sources, MCNP provides the user with pre-existing source functions. These pre-existing functions include analytic functions for fission energy spectra such as, Watt, Maxwellian and Gaussian for energy, Gaussian for time, and isotropic, cosine, and mono-directional for the source direction [51].

## 4.2.7 Tallies and Output

At the end of an MCNP simulation, the code automatically creates a set of standard summary information about the simulation. This set of information provides the users further insight into the physics and the adequacy of the Monte Carlo simulation for their problem. The standard summary includes: a complete account of creation and loss of all particle tracks as well as their energy; the track population in a given cell; the number of collisions in a cell, the average weight, mean free path, and energy of tracks in a cell; the activity of each radionuclide in a cell; and a complete weight balance for each cell.

In addition to the standard summary provided at the end of every run, MCNP provides the user with a set of seven standard tallies. A tally is a virtual detector which counts specific events as the particles are simulated. These tallies allow a new method for the user to obtain output from a simulation. Some forms of tallies are: particle current, particle flux and energy deposition. All available tallies in MCNP are summarized in the following table,

*Table 4.1: Available MCNP tallies*

<b>Tally Mnemonic</b>	<b>Description</b>
<i>F1:N or F1:P or F1:E</i>	Surface current
<i>F2:N or F2:P or F2:E</i>	Surface flux
<i>F4:N or F4:P or F4:E</i>	Track length estimate of cell flux
<i>F5a:N or F5a:P</i>	Flux at a point or ring detector
<i>F6:N or F6:P or F6:N,P</i>	Track length estimate of energy deposition
<i>F7:N</i>	Track length estimate of fission energy deposition
<i>F8:N or F8:P or F8:E or F8:P,E</i>	Pulse height tally

Note, that in the above table under the column, Tally Mnemonic, N stands for neutron, P stands for photon, E stands for electron, N,P stands for coupled neutron/photon and P,E stands for coupled photon/electron.

Multiple tallies of the same or various types can be used in the same simulation. For multiple tallies of the same type, simply add multiples of 10 to the tally number. For example, the user specifies the use of four individual F1:N tallies, the tallies would have the following numbers F1:N, F11:N, F21:N, and F31:N.

The units of a tally are determined by the particle type specified in the tally mnemonic as well as a base unit specific to each tally type. For example, N as a tally mnemonic specifies neutrons, and tally type 1 species current. Therefore, an F1:N tallies has units of neutrons per time.

When discussing end flux peaking and peaking factors, the quantity of interest from the simulation is the neutron flux at various points along the length of the fuel bundle. This type of output requires the user to specify a F4:N tally in the input file. For F4:N tallies, the following table demonstrates the quantity being scored,

Table 4.2: F4:N Tally Quantity Scored

Tally	Score	Physical Quantity	Units
F4:N	$W \frac{T_l}{V}$	$\bar{\phi}_V = \frac{1}{V} \int dE \int dt \int dV \int d\Omega \Psi(\vec{r}, \Omega, E, t)$	Neutrons/cm <sup>2</sup>

where  $W$  is the particle weight,  $T_l$  is the track length in units of centimeters, (a track length being a measure of the event transit time multiplied by the particle velocity),  $V$  is the volume of the cell calculated by the code,  $\bar{\phi}_V$  is the average flux in a given cell (volume), and  $\Psi$ , is the angular flux.

The equation for  $\Psi$ , can be expanded to be,

$$\Psi(\vec{r}, \Omega, E, t) = vn(\vec{r}, \Omega, E, t) \quad 4.2.5$$

where  $n$  is the particle density ( $particles \cdot MeV \cdot steradian^{-1}$ ) and  $v$  is the velocity in cm/s. Thus the units of  $\Psi$  are ( $particles \cdot cm^{-2} \cdot MeV \cdot s \cdot steradian^{-1}$ ). See Appendix A.2 for a derivation.

In addition to the standard tallies, newer versions of MCNP provide access to a special tally form known as the superimposed mesh tally. The benefit of using a superimposed mesh tally over the standard tallies is that it allows the user to tally particles on a mesh that is independent of the problem geometry. The most recent version of MCNP, MCNP-6.1, only has the ability to implement superimposed mesh tally for track length estimate of cell flux or the F4 tally. To invoke a superimposed mesh tally, use the FMESH card. The FMESH card has many structural similarities to the F tally cards. For example, the FMESH tally card requires a unique number to be assigned for every mesh tally invoked within the simulation. The unique number also increments in multiples of ten for every new FMESH tally type.

Two types of mesh symmetry are provided for the FMESH tally. The mesh symmetries provided are rectangular or cylindrical. Since the investigation conducted in this work involves CANDU fuel bundles which have cylindrical symmetry, FMESH tallies using cylindrical mesh were included in the input deck. In the cylindrical mesh, there are three pairs of geometric parameters which need to be specified to provide detail in a mesh. The first pair of geometric parameters is the coarse mesh points along the radius, *imesh*, and the number of divisions, or fine mesh points, *iints*, between each coarse mesh

point. The second pair is the coarse mesh points along the length of the cylinder, *jmesh*, and the fine mesh points, *jints*. The third and final pairs are the coarse and fine mesh points along a 360° circle, *kmesh* and *kints* respectively. In MCNP, the angles which need to be provided are represented by values from 0 to 1, where 1 represents a full rotation or  $2\pi$  radians (360°) [52].

## 4.2.8 Physics

The essence of Monte Carlo codes is the physics behind the problems they are trying to solve, MCNP is no exception. This section is used to describe the equations that MCNP intends to solve. Two concepts of great importance for setting up the input and understanding the output are particle weight and particle tracks. These concepts will be described in the following subsections [51].

### 4.2.8.1 Particle Weight

Particle weight is a number that each particle in an MCNP simulation carries, and represents the particles contribution to the final tally outputs specified by the user. The magnitude of the particle weight is determined such that whenever MCNP deviates from an exact physical solution to the problem, the expected solution is statistically preserved.

Fundamentally, the term particle weight refers to an adjustment for the deviation of the Monte Carlo transport process from an exact physical transport process. The inclusion of particle weight is necessary to introduce some slight variance between the results predicted by the Monte Carlo method and those that are physically observed. Without the inclusion of particle weights, if a Monte Carlo method were to simulate physically observed distributions, the outputs would have the same mean and variance as the experimental comparison results. Having the variance of the Monte Carlo and physical system being the same is not ideal, since the variance of physically observed systems tends to be high. Therefore, Monte Carlo codes chose to modify the sampling process through the use of some form of variance reduction technique, which will be described in a later section. These variance reduction techniques use a weighting scheme to replicate the same mean as what would be observed in a physical system, while lowering the calculated variance. The goal of all of this is to improve computational efficiency [51].

### 4.2.8.2 Particle Tracks

Particle tracks are created as soon as a particle is generated from a defined source. If a secondary particle is generated through interactions of a primary particle with materials defined in the problem, then secondary particle tracks are generated. This means two particle tracks which originate from the same source particle. Each of these two tracks will have half the source particle's weight. A single particle track represents each component of a source particle during its lifetime. If a track crosses a surface it can be used to calculate fluence, flux, or pulse-height energy deposition, assuming the proper tallies are specified in the input file.

To sample a collision along a given track the following theory is needed. The probability that a particle will collide between distance  $l$  and  $l + dl$  along the track is given by:

$$p(l)dl = e^{-\Sigma_t l} \Sigma_t dl \quad 4.2.6$$

where  $\Sigma_t$  is the macroscopic cross section of the medium, considered as the probability of collision per unit length. If  $\xi$  is defined as a random number which exists in the range of  $[0,1)$ , then,

$$\xi = \int_0^l e^{-\Sigma_t s} \Sigma_t ds = 1 - e^{-\Sigma_t l} \quad 4.2.7$$

which can be solved for  $l$ , giving,

$$l = -\frac{1}{\Sigma_t} \ln(1 - \xi) \quad 4.2.8$$

Using the ideas derived in this section, discussions relating to interactions related to neutrons can be discussed in greater detail [51].

## 4.2.9 Neutron Interactions

When a simulated particle that represents any number of neutrons, depending on particle weight, collides with a nucleus in the medium, the following sequence occurs within the MCNP code,

1. Collision nuclide is identified;
2. Either the S( $\alpha,\beta$ ) treatment is used (if defined by user) or the velocity of target nucleus is sampled for low-energy neutrons;
3. Photons are generated (for later transport);
4. Neutron capture is modelled;
5. If S( $\alpha,\beta$ ) is not used then elastic or inelastic scattering is selected, this includes fission, energy and direction of new tracks is determined;
6. If S( $\alpha,\beta$ ) is used and the neutron energy is appropriate, then, instead of step 5, the S( $\alpha,\beta$ ) models the collision.

Each of the steps in this process is described in further detail below [52].

### 4.2.9.1 Selection of Collision Nuclide

If the material in which the collision is taking place consists of  $n$  separate nuclides, and  $\xi$  is again a random number within the unit interval of  $[0,1)$ , then the collision nuclide known as the  $k$ th nuclide is selected if the following condition is satisfied,

$$\sum_{i=1}^{k-1} \Sigma_{ti} < \xi \sum_{i=1}^n \Sigma_{ti} < \sum_{i=1}^k \Sigma_{ti} \quad 4.2.9$$



where  $\Sigma_{ti}$  is the total macroscopic cross section of the *ith* nuclide.

Equation 4.2.9 states that if the sum of the macroscopic cross section for all  $n$  nuclides multiplied by the random number,  $\xi$ , is less than the sum of all macroscopic cross sections up to the collision nuclide,  $k$ , but greater than the sum of all macroscopic cross section up to the nuclide prior to the collision,  $k - 1$ , then a collision will take place.

If the energy of the neutron is below the thermal limit (4 eV) and the appropriate  $S(\alpha,\beta)$  table is included, then the total cross section is determined as the sum of the capture cross section from the original cross-section table and the elastic and inelastic scattering cross sections as calculated by the  $S(\alpha,\beta)$  treatment. If the  $S(\alpha,\beta)$  treatment is not specified then the total cross section is taken from the original cross section table with adjustments performed for the thermal effects, described in the next section [51] [52].

## 4.2.9.2 Free Gas Thermal Treatment

When a neutron collides with an atom, the thermal motion of the atom is affected. The collision is then affected by the presence of nearby atoms. The effect of thermal motion on the collision cannot be ignored without having serious impact on the error of the problem. To counteract this potential error, MCNP uses the free gas approximation to account for the thermal motion of the atoms in a collision. While the  $S(\alpha,\beta)$  treatment takes into effect the chemical binding and crystalline structure for collisions with neutrons below 4 eV, the free gas thermal treatment (FGTT) capability is limited to a few substances and temperatures.

The FGTT assumes that the medium in which the collision takes place is a free gas, meaning the particles are not bound to each other. FGTT also assumes that the medium exists within the range where the thermal effects of a collision are significant and that the reaction cross sections with no thermal effects are independent of neutron energy. These assumptions are included to increase the speed of calculation in the thermal region such that it is almost on par with the simulation speed in the non-thermal region.

The goal of implementing the FGTT is to adjust the elastic cross section by taking into account the velocity of the target nucleus when collision kinematics are being calculated. This means that the FGTT only significantly applies to the elastic scattering and does not take into account inelastic scattering. The FGTT in MCNP can be described as a two-stage process, where the elastic cross section is first adjusted then sampling the velocity of the target nucleus occurs. Both of these processes will be described in detail in the following section [51] [52].

### 4.2.9.2.1 Adjusting the Elastic Cross Section

The step of adjusting the zero-temperature elastic cross section involves the introduction of a new factor, referred to as  $F$ . The  $F$  factor is a quantity to which the elastic cross section will have the following form:

$$F = \left(1 + \frac{0.5}{a^2}\right) \operatorname{erf}(a) + \frac{\exp(-a^2)}{(a\sqrt{\pi})} \quad \text{where } a = \sqrt{\frac{AE}{kT}} \quad 4.2.10$$

with  $A$  being the atomic weight of the nuclide,  $E$  is the energy of the incident neutron,  $T$  is the temperature of the system in Kelvin, and  $k$  is the Boltzmann constant, with  $\operatorname{erf}(a)$  being the error function (or Gauss error function). The Gauss error function and is defined as,

$$\operatorname{erf}(x) = \frac{2}{\sqrt{\pi}} \int_0^x e^{-t^2} dt \quad 4.2.11$$

To speed up the calculation, the factor  $F$  is simplified to,

$$F = \left(1 + \frac{0.5}{a^2}\right) \quad \text{for } a \geq 2 \quad 4.2.12$$

and is further simplified using linear interpolation when  $a$  is less than two. A linear interpolation is performed from a table containing 51 values of  $F$ . To ensure the calculation proceeds as quickly as possible, the thermal adjustment is omitted if the neutron energy is above  $500 kT/A$  and if the adjusted elastic cross section would be less than 0.1%.

The adjustment phase does not occur in a single step, instead it occurs partly at the setup of the problem and partly during the actual transport of the neutron. However, no adjustments are performed on the elastic cross section if the data library already has been processed to the temperature of the problem [51].

#### 4.2.9.2.2 Sampling the Velocity of the Target Nucleus

The second phase of the FGTT involves subtracting the sampled target velocity from the neutron velocity to obtain a relative velocity between the target and neutron. The frame-of-reference in which the collision occurs, is considered the target-at-rest frame. The benefit of using a target-at-rest frame in this type of calculation is that it utilizes the relative energy between the neutron and target,  $E_r$ , to determine elastic and inelastic scattering, as well as fission. The laboratory-frame incident energy,  $E_o$ , is used in MCNP for the following purposes: obtain the distance to collision, select collision nuclide, determine energy cut-offs, generate photons, generate fission sites for KCODE when criticality is of interest in a problem, for  $S(\alpha,\beta)$  scattering and for neutron capture [51].

MCNP uses the limit of  $400kT$  on incident neutron energy and whether the collision occurs with a hydrogen atom to set the velocity of the target to zero. If these conditions are not met, MCNP will sample the target velocity based on the following equations, discussed below [51].

The effective scattering cross section in the laboratory frame for a neutron with an energy of  $E$  is as follow:

$$\sigma_s^{eff}(E) = \frac{1}{v_n} \iint \sigma_s(v_{rel}) v_{rel} p(V) dv \frac{d\mu_t}{2} \quad 4.2.13$$

where,  $v_{rel}$  is the relative velocity between the neutron and the target, with the neutron travelling at a scalar velocity of  $v_n$  and the target moving at a scalar velocity of  $V$ ,  $\mu_t$  is the cosine angle between the direction-of-flight vectors of the neutron and the target,  $\sigma_s(v_{rel})$  is the scattering cross section at the relative velocity, and  $p(V)$  is the probability density function for the target velocities, which follows a Maxwellian distribution [51].

The equation for the relative velocity can be defined using the cosine law ( $c^2 = a^2 + b^2 - 2ab \cos(C)$ ), which makes use of the velocity vectors, as demonstrated below,

$$v_{rel} = (v_n^2 + V^2 - 2v_n V \mu_t)^{1/2} \quad 4.2.14$$

The probability density function can be defined as follows:

$$p(V) = \frac{4}{\pi^{1/2}} \beta^3 V^2 e^{-\beta^2 V^2} \quad 4.2.15$$

where  $\beta$  is defined as,

$$\beta = \left( \frac{AM_n}{2kT} \right)^{1/2} \quad 4.2.16$$

where  $A$  is the target nucleus mass in atomic mass units (amu), one amu is the approximate mass of a single nucleon (proton or neutron) and is defined as being one twelfth the mass of a neutral carbon-12, (C-12), ground state nucleus.  $M_n$  is the neutron mass in units of  $MeV \cdot sh/cm^2$ , and  $kT$  is the equilibrium temperature of the target nuclei in MeV [51].

### 4.3 Least Squares Method

The objective of the Least Squares Method (LSM) is to provide adjustments for parameters in a function used in a model to best fit a set of experiment data. To understand the concept behind the LSM, consider a set of  $n$  data points,

$$(x_i, y_i) \quad i = 1, \dots, n \quad 4.3.1$$

where  $x_i$  are the independent variables and  $y_i$  are the dependent variables.

To find the optimum value using the LSM a sum of residuals must be at a minimum, where the sum is calculated as,

$$S = \sum_{i=1}^n r_i^2 \quad 4.3.2$$

where  $r_i$  are the residuals defined as the difference between the actual value of the dependent variable and the value predicted by the model function. In general, residuals have the following form,

$$r_i = y_i - f(x_i, \beta) \quad 4.3.3$$

where  $x_i$  and  $y_i$  are the independent and dependent variables mentioned above,  $f(x_i, \beta)$  is the form of the model function, with  $m$  parameters contained within the vector  $\beta$ . The function of the least squares method in the context of this project was to provide a means to score each MCNP trial [54].

## 4.4 Geometry Specification

At the beginning of the investigation, the idea of trying to simplify the CANDU fuel bundle model to improve computational speeds was proposed. Various simplified models were investigated, shown in Figures 4.2 and 4.3. In both of these simplified models, the fuel, coolant and CANLUB are represented by a single large homogenized cylinder instead of having the fuel distributed in pellets amongst 37 individual fuel elements. The homogenized cylinder in Model 1 and 2 is then surrounded by a Zircaloy-4 sheath. Simplified end plates are positioned at either end of the homogenized cylinder. The entire simplified bundle is then surrounded by a large volume of heavy water moderator. The large volume of heavy water in comparison to the dimensions of the homogenized cylinder is included to mimic having an infinite amount of moderator surrounding the homogenized bundle. Beyond the large volume of moderator, a box was defined to include a boundary condition in the model. In this case neutrons which make it to the boundary are terminated. Terminating neutrons beyond the boundary mimics an infinite sink as the boundary condition. To counteract the infinite sink many neutrons were simulated in an effort to continuously flood the system. This method of generating many neutrons had its obvious drawbacks in terms of computation time but still provided a quicker method than defining the infinite moderator. Dimensions for the simplified model were taken from the design of a CANDU fuel bundle. Features of the CANDU fuel bundle design is demonstrated in Table 4.3.

Table 4.3: CANDU fuel bundle design features

Parameter	Value	Parameter	Value
Number of elements per bundle	37	Sheath thickness (mm)	0.4
U weight per bundle (kg)	19.2	Pellet outside diameter (mm)	12
Zr weight per bundle (kg)	2.2	Pellet length (mm)	16
Overall bundle length (mm)	495	Pellet density (g/cm <sup>3</sup> )	10.6
Overall bundle diameter (mm)	102	Endplate width (outer ring) (mm)	4.9
Element length (mm)	493	Endplate thickness (mm)	1.6
Element outside diameter (mm)	13		

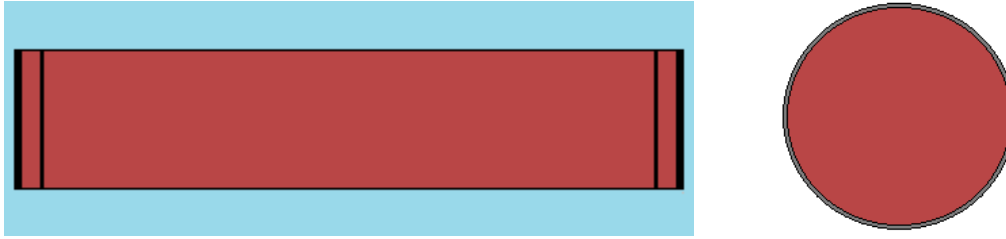


*Figure 4.2: First MCNP model geometry including axial and radial image of model*

A large issue with the first simplified model is that having to simulate a large volume of moderator increases the computational time. This increase in computational time is due to the fact that MCNP must maintain all the particle tracks until they either reach the infinite sink or are absorbed by the moderator. Aside the issue related to computational time, the first simplified model had an issue with the method in which neutrons were simulated. In this model the entire homogenized cylinder was taken as the source. Every point contained within the homogenized cylinder had equal probability of creating a neutron of a given energy. The issue with this however is not related to the shape or distribution of the source but how the neutron energies were simulated. The neutron energies were simulated as either having an energy of 1.0 MeV or 0.025 eV, fast or thermal neutrons respectively. This method of simulating a single neutron energy does not represent the fission process, since fission neutrons are produced with energies based on a continuous probability distribution.

To address the shortcomings of the first simplified model, a second simplified model was created. This second model applies a more physical boundary condition as well as the method in which the neutrons are created. The second model is shown in the figure below,

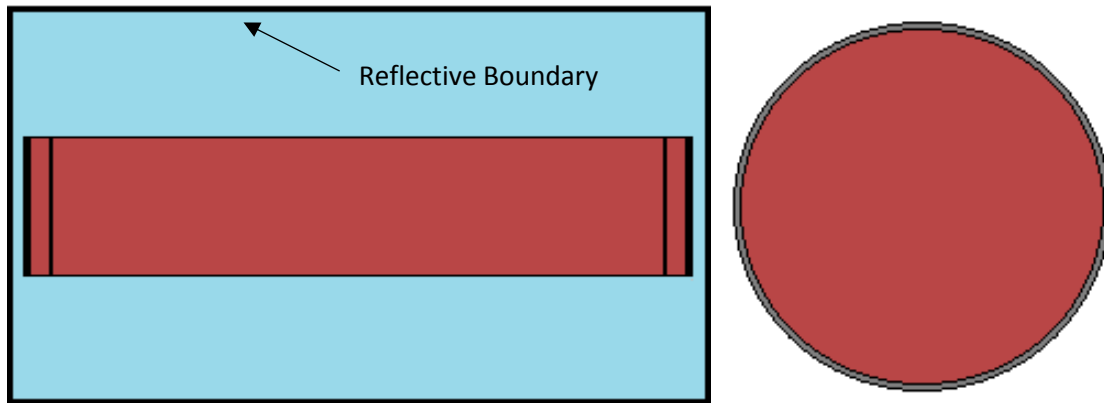


*Figure 4.3: Second MCNP model geometry*

The first improvement of applying a more physical boundary condition, involves eliminating the large volume of moderator and applying a reflective boundary condition on the outer box instead of using an infinite sink. Having a reflective boundary cuts back on the number of neutrons that need to be simulated, as well as ignores the effects of neutron leakage (i.e. an infinite lattice simulation). Neutron leakage refers to neutrons which escape the reactor core and no longer are used in fission processes. The drop-in number of neutrons being simulated is due to the fact that neutrons which are incident upon the reflective boundary are sent back towards the homogenized cylinder. This means that particle tracks are only concluded if the particle is absorbed by some medium in the model.

Also, the reflective boundary allows neutrons that are reflected to appear as neutrons coming from an adjacent fuel channel, as shown in Figure 4.4. The diameter of the cell in Figure 4.4, is 28.575

cm. Although instead of representing a realistic CANDU core, the reflective boundary condition represents an infinite core since no neutrons escape from the single lattice cell. In a realistic CANDU core some neutrons do indeed leak out, which lead to some neutrons not continuing the chain-reaction.

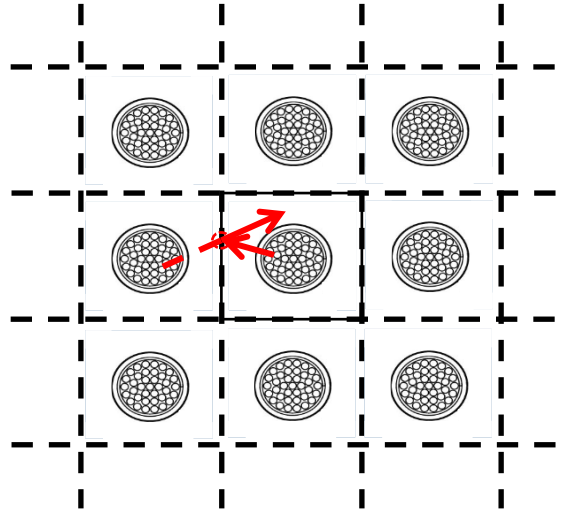


Figure 4.4: Reflective boundary conditions mimic an infinite lattice of fuel bundles

The second improvement of this model was the use of a more physical method in which neutrons are simulated. This improvement makes use of a function built into MCNP referred to as a KCODE calculation. The KCODE calculation is primarily used in MCNP to calculate the reactivity and steady state neutron distributions. To determine the reactivity and steady state neutron distributions of a problem, the KCODE calculation makes use of a well-defined neutron simulation technique. The KCODE neutron simulation technique makes use of a neutron energy probability distribution referred to as a Watt's fission spectrum. The particular Watt's fission spectrum utilized by the KCODE calculation is for U-235, which is the fissile isotope in natural uranium. The equation for the U-235 Watt's spectrum is given by,

$$N(E) = \frac{\exp\left(-\frac{E_f}{T_W}\right)}{(\pi E_f T_W)^{1/2}} \exp\left(-\frac{E}{T_W}\right) \sinh\left[2(E_f E)^{1/2}/T_W\right] \quad 4.4.1$$

provided by MCNP Physics Manual [51]. In Equation 5.1.1  $N(E)$  is the probability a neutron will be emitted from fission with an energy  $E$ ,  $E$  is the energy of the neutron in the laboratory coordinate system,  $E_f$  is the average kinetic energy per nucleon,  $T_W$  is the effective Watt temperature.  $T_W$  is determined using the maximum temperature for the laboratory system and is given by,  $T_W = \frac{8}{9}T_m$  where  $T_m$  is the maximum temperature in the laboratory system [51].

Experimentally, the Watt's spectrum for U-235 can be simplified as,

$$N(E) = 0.453 \exp[-1.036E] \sinh[\sqrt{2.29E}] \quad 4.4.2$$

Figure 4.5 represents a plot of this equation which has the following form:

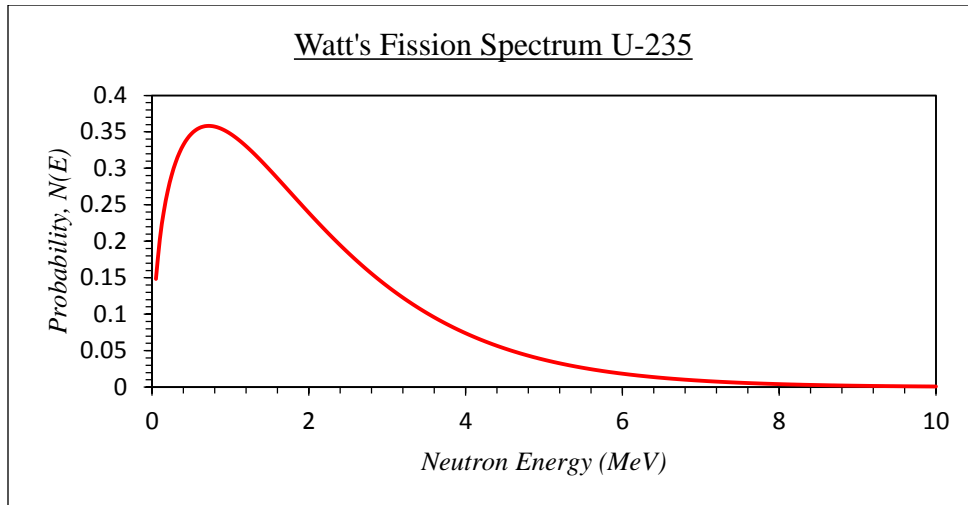


Figure 4.5: U-235 fission spectrum using the empirical formula from Equation 5.1.2

From the graph, the peak neutron energy is roughly, 0.724 MeV. After the peak neutron energy, the form of the curve is a decaying exponential in nature. The probability of generating a neutron with an energy of 10.0 MeV approaches zero. Therefore, during fission U-235 is most likely to emit a neutron in the fast region (1-2 MeV) [51].

The added benefit of simulating the neutrons using KCODE is that the simulation iterates the spatial distribution of neutrons in the source, improving it each time it runs. This allows for more accurate results with less computational time. Having included the following improvements to the first simplified model, the computational time, as well as physical accuracy of the model are greatly improved. The second model still uses a homogenized cylinder, poorly accurate results.

The third (and final) model maintains the improvements of the second simplified model, and replaces the homogenized cylinder with a more physical, yet still slightly simplified, CANDU 37-element fuel bundle. To get a more accurate representation of the EFP phenomenon, two half-fuel-bundles were modelled instead of a single full-fuel-bundle. By modelling the half-fuel-bundles, a contact region between two fuel bundles was able to be included in the model. This third model is shown in the Figure 4.6 below,

Also, included in this model are the calandria and pressure tubes, not shown in the above figure. These were included to create a more faithful model of a fuel bundle inside a CANDU reactor. The coolant is now a separate material from the natural uranium fuel, while the heavy water moderator surrounds the calandria tube. In between the pressure tube and the calandria tube is a gap of heated air, referred to as the annulus gas. The exact geometry of the end plates was not included in this model, instead an additional cylinder was modelled on the end of each end-cap, with the same radius as the end-cap a thickness given by the endplate thickness. The fuel within each half-element is modelled as a solid rod, with the exception to the last two pellets. The last two pellets are defined separately for the purpose of adding the absorbing material into the fuel. On the inside of each sheath there is a 6 micron CANLUB coating.

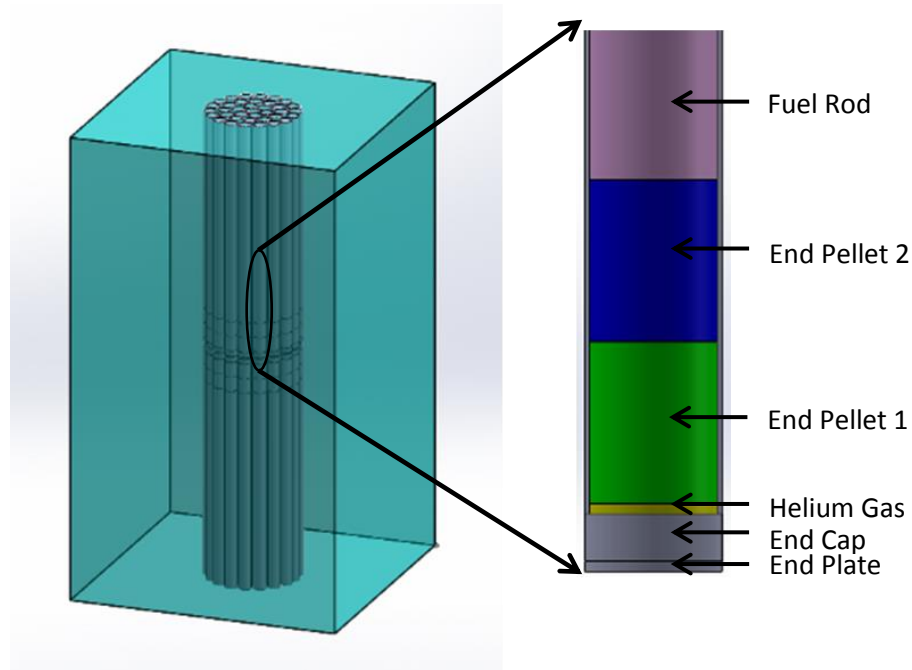


Figure 4.6: Two half bundle model, including blown up cross section of a fuel element

## 4.5 Material Specification

In the first two simplified geometries where a solid homogenized cylinder of fuel, coolant and CANLUB was used, the mass of the homogenized cylinder was taken as 22 kg, and the mass of the Zircaloy-4 sheath, endcaps and end-plate around the homogenized cylinder was taken as 2 kg. These masses represent the total mass of each region of material in a typical CANDU fuel bundle. When defining a material within a cell in MCNP, the user must provide a density value. By definition, density is calculated as follows,

$$\rho = \frac{M}{V} \quad 4.5.1$$

where  $M$  is the mass of the material in question and  $V$  is the volume that the material occupies.

For the simplified model the geometry is cylindrical, the volume of a cylinder is calculated as follows,

$$V = \pi r^2 h \quad 4.5.2$$

where  $r$  is the radius of the cylinder and  $h$  its height.

In MCNP, material properties are defined in the data card section of the input deck. The material properties include the isotopic components which constitute the material which are defined as either atomic or weight fractions. For the purposes of this project, weight fractions were used. To find a weight



fraction for a particular material, the atomic fraction and atomic mass were first taken from KAERI's Table of Nuclides (<http://atom.kaeri.re.kr>). For compounds, such as  $\text{UO}_2$ , the total molar mass must be calculated. The mass of each compound and their corresponding isotopes are found using the atomic fractions. Finally, the weight fraction determined as the ratio of the mass of the isotope to the total molar mass. An example of this process for  $\text{UO}_2$  is as follows,

The isotopic breakdown of U and O in natural  $\text{UO}_2$  fuel is provided in Table 4.4.

Table 4.4: Information obtained from KAERI website

Element	Molar Mass (amu)	Isotopes	Atomic Fraction (%)	Isotopic Mass $M_{iso}$ (amu)
Uranium (U)	238.03	$^{235}\text{U}$	0.720	1.7138
		$^{238}\text{U}$	99.28	236.32
Oxygen (O)	15.990	$^{16}\text{O}$	1.000	15.999

**Step 1:** Find the total mass of the molecule.

For  $\text{UO}_2$ , this calculation is as follows,

$$M_{tot} = M_{\text{U}235} + M_{\text{U}238} + 2M_{\text{O}16} = 270.03 \text{ amu} \quad 4.5.3$$

**Step 2:** Find the mass fraction using ratio of isotopic mass to total mass.

The equation for weight fraction ( $wf$ ) is as follows,

$$wf = \frac{M_{iso}}{M_{tot}} \quad 4.5.4$$

Applying this equation for each element's isotopes results in the following weight fractions summarized in Table 4.5,

Table 4.5: Weight fractions for natural  $\text{UO}_2$

Element	Isotope	Weight Fraction $wf$
Uranium (U)	$^{235}\text{U}$	0.0063
	$^{238}\text{U}$	0.8752
Oxygen (O)	$^{16}\text{O}$	0.1185

This process is repeated for every material defined in the input deck. For the final model of the 37-elements fuel bundle material densities were taken from *Chan et al* where a 37-element bundle model was also created.

The above explanation applies to cases for which the atomic composition of the material occupying a known volume. However, when the atomic composition of the material is being altered by the addition of a new foreign material, the process of determining atomic composition must be altered. This new process was adopted to handle the addition of BNA material into the various components of the CANDU fuel bundle. As with the previous method, the new method is best understood through an example.

Example: Addition of 10 mg of europium oxide in a single fuel pellet

Before proceeding with any calculations, it is important that various constants be collected either experimentally or from literature. The constant provided in Table 4.6 were obtained from the Kaeri Table of Nuclides and [2]. For this example, the important constants are summarised in Table 4.6. Note that the term percent in the first column of Table 4.6, refers to the total weight fraction multiplied by 100%, which each isotope or element in a molecule occupies.

As an example, the molecule  $\text{Eu}_2\text{O}_3$  consists of 2 europium atoms and 3 oxygen atoms. Oxygen is composed entirely of the O-16 isotope. Naturally occurring europium is composed of two isotopes, Eu-151 and Eu-153. Using the steps outlined in the procedure above, the weight percent breakdown for each isotope in  $\text{Eu}_2\text{O}_3$  is given in the rows two to four of Table 4.6.

Table 4.6: Constants used in the determination of atomic composition of doped fuel

Constant	Value
Isotopic Percent Eu-151 ( $\text{Eu}_2\text{O}_3$ )	41.28
Isotopic Percent Eu-153 ( $\text{Eu}_2\text{O}_3$ )	45.08
Isotopic Percent O-16 ( $\text{Eu}_2\text{O}_3$ )	13.64
Isotopic Percent U-235 ( $\text{UO}_2$ )	0.630
Isotopic Percent U-238 ( $\text{UO}_2$ )	87.52
Isotopic Percent O-16 ( $\text{UO}_2$ )	11.85
Number of Pellets	1
Pellet Mass (g)	18.90
Pellet Volume ( $\text{cm}^3$ )	1.800
Fuel Density ( $\text{g}/\text{cm}^3$ )	10.4
Europium Oxide Density ( $\text{g}/\text{cm}^3$ )	7.40

With the necessary constants now collected, the atomic composition of the doped fuel can now be determined.

Step 1: Determine the amount of absorber being added to each fuel pellet

- Convert amount of absorber added from mg to g
- As an example, 10 mg of  $\text{Eu}_2\text{O}_3$  becomes 0.01 g
- Since the BNA is being added to only one fuel pellet, the amount of BNA added to this pellet is 0.01 g, or 0.01 g/ 1 fuel pellet

Step 2: Determine the volume that will be occupied by the BNA once added to the fuel

- Take the amount of BNA added to each pellet and divide by the density of the BNA,

$$V_{\text{Eu}_2\text{O}_3} = \frac{M}{\rho_{\text{Eu}_2\text{O}_3}} = \frac{0.01 \text{ g}}{7.40 \text{ g/cm}^3} = 1.3 \times 10^{-3} \text{ cm}^3 \quad 4.5.5$$

Step 3: Determine the volume and mass of the  $\text{UO}_2$  fuel

- Subtract the BNA volume from the total volume of the fuel pellet, from Table 5.3

$$V_{\text{UO}_2} = V_{\text{tot}} - V_{\text{Eu}_2\text{O}_3} = 1.8000 \text{ cm}^3 - 1.3 \times 10^{-3} \text{ cm}^3 = 1.7987 \text{ cm}^3 \quad 4.5.6$$

- Using the volume of  $\text{UO}_2$  fuel, the mass can be determined using,

$$M_{\text{UO}_2} = V_{\text{UO}_2} \times \rho_{\text{UO}_2} = 1.7987 \text{ cm}^3 \times 10.4000 \text{ g/cm}^3 = 18.7084 \text{ g} \quad 4.5.7$$

Step 4: Determine the atomic abundance of each isotope of BNA and  $\text{UO}_2$  fuel in the doped fuel material

- For the BNA use the following equation,

$$\text{Abundance}_X = \frac{M_{\text{BNA}} \times \%X_{\text{BNA}}}{M_{\text{UO}_2} + M_{\text{BNA}}} \quad 4.5.8$$

where  $\text{Abundance}_X$  is the abundance of isotope X in BNA,  $M_{\text{BNA}}$  is the mass of the BNA added,  $\%X_{\text{BNA}}$  is the percent isotope X composes the BNA in decimal form, and  $M_{\text{UO}_2}$  is the mass of the  $\text{UO}_2$  fuel.

- For the  $\text{UO}_2$  fuel use the following equation,

$$\text{Abundance}_Y = \frac{M_{\text{UO}_2} \times \%Y_{\text{UO}_2}}{M_{\text{UO}_2} + M_{\text{BNA}}} \quad 4.5.9$$

where  $\text{Abundance}_Y$  is the abundance of isotope Y in  $\text{UO}_2$  fuel,  $M_{\text{UO}_2}$  is the mass of the  $\text{UO}_2$  fuel added,  $\%Y_{\text{UO}_2}$  is the percent isotope Y composing the  $\text{UO}_2$  fuel in decimal form, and  $M_{\text{BNA}}$  is the mass of the BNA.

- For the specific example of 10 mg of  $\text{Eu}_2\text{O}_3$ , the atomic abundances are summarised in Table 4.7,

Table 4.7: Isotropic abundance for 10 mg of  $\text{Eu}_2\text{O}_3$  added to a fuel pellet

Isotope	Abundance (decimal)
<i>Eu-151</i>	$1.102 \times 10^{-4}$
<i>Eu-153</i>	$1.204 \times 10^{-4}$
<i>U-235</i>	$6.297 \times 10^{-3}$
<i>U-238</i>	$8.745 \times 10^{-1}$
<i>O-16</i>	$1.184 \times 10^{-1}$

*Note: Since O-16 is a component of both the BNA and the  $\text{UO}_2$  fuel, the total atomic abundance is then the sum of the individual abundances from the BNA and  $\text{UO}_2$ .*

The process outlined in these four steps is done in the automatic input generation MATLAB script to help generate a set of MCNP trials with differing amounts of BNA added to the fuel. This script is shown in Appendix A.3, and will be discussed in Section 5.6 [55] [56] [57].

# Chapter 5: Results and Discussion

## 5.1 Preliminary Model Results

This section presents the results for the first two simplified preliminary MCNP models. Two key results that will be discussed are the importance of the geometry when modeling fuel bundles, and the effectiveness of neutron absorbers in mitigating EFP. To analyse the importance of the geometry, correct boundary conditions and the use of a physical neutron simulation technique are considered. Cases with no absorber added to a bundle for each MCNP model are compared. Comparisons of the axial thermal neutron flux ensure that the simplifications done to the model still retain the physics observed in a reactor. Figure 5.1 provides this comparison; geometries are numbered according to the order in which they are introduced in the previous section.

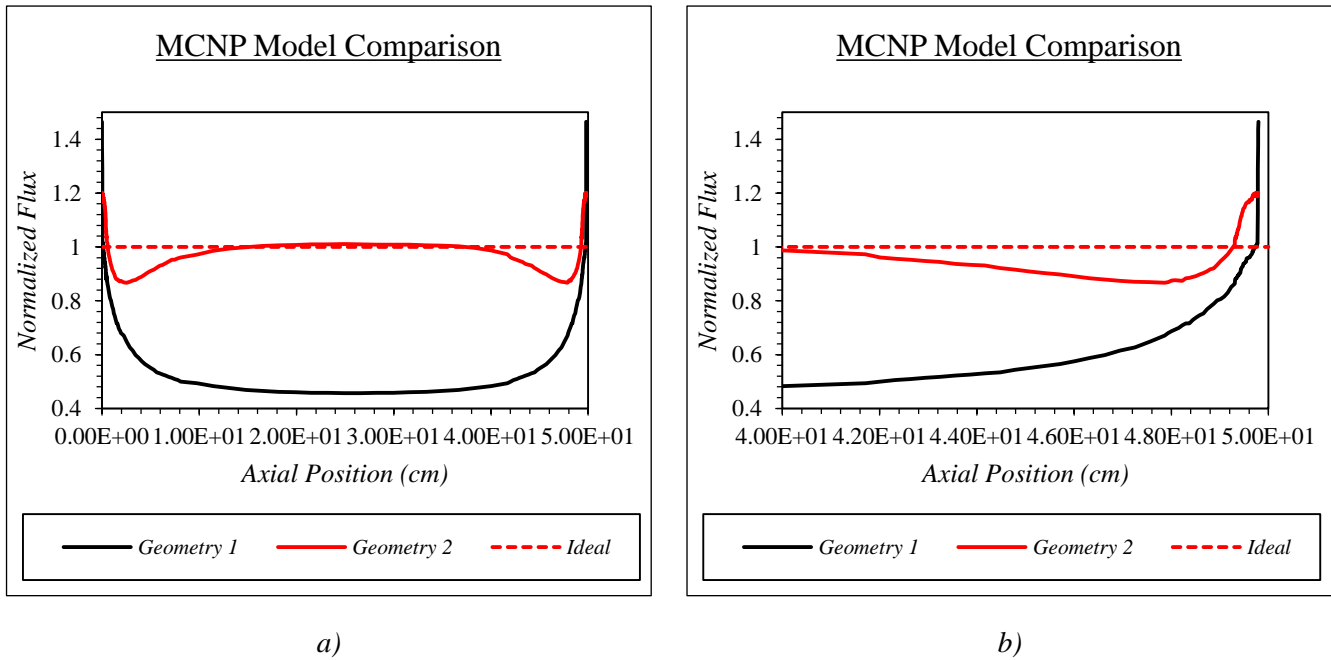
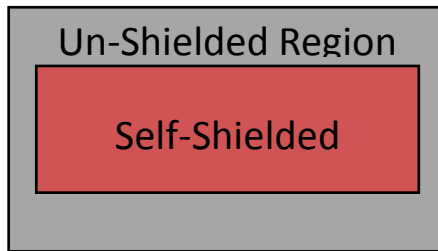


Figure 5.1: Effect of geometry on axial-thermal-neutron flux throughout the length of the bundle, a) Full length of the fuel bundle, b) zoomed into one end region of the fuel bundle

Note that the y-axes of the above graphs represent axial-thermal-neutron flux normalized to the center flux. As shown in Figure 5.1 all three geometries produce different curve shapes. The dashed “Ideal” line represents the averaged and normalized center axial-thermal-neutron flux value for these three geometries, and is included in these graphs to help highlight features of the results. The two preliminary models have various simplifications which introduce non-physical features into the flux curve.

In both Figure 5.1a and Figure 5.1b, results for Geometry 1 and 2 shown regions where the normalized flux dips below the ideal line. Geometry 1 is showing significant dipping along the entire length of the homogenized fuel bundle. The reason these dips occur in the first two simplified models is

due to an effect known as self-shielding. Self-shielding is a phenomenon where the outer portion of some material prevents particle interactions with its inner portion. This phenomenon exists only when there is enough material in a given volume that particles cannot penetrate beyond a certain depth without being absorbed. Figure 5.2 demonstrates the principle of self-shielding,



*Figure 5.2: Shelf-shielding model*

Figure 5.2 demonstrates how low-energy neutrons, like thermal neutrons, are unable to penetrate through the entirety of a large homogenized cylinder. Since low-energy neutrons will interact with the homogenous material before reaching the center of the cylinder.

The difference between Geometry 1 and 2 is related to the fact that one geometry uses reflective boundary conditions while the other does not. As mentioned in Section 5.1, the boundary condition for Geometry 1 is a near infinite sink. This means that neutrons which escape from the homogenized fuel bundle can only re-enter the bundle if they are scattered by the heavy water moderator surrounding the bundle. This scattering is only one possible type of interaction, some neutrons may also be absorbed and others which do scatter may scatter away from the bundle. All of these interactions of course happen regardless of the bundle geometry. The issue arises from the fact that in a CANDU core there exists a lattice of fuel channels where neutrons that escape one bundle may interact with a bundle in an adjacent fuel channel. Also, since thermal neutrons are low in energy they are more likely to be absorbed. Therefore, using the near-infinite sink boundary condition means that it is less likely for thermal neutrons to interact with the homogenized fuel bundle. Coupling the issue of a near-infinite boundary condition with the existence of self-shielding leads to a normalized axial flux curve that dips well below the normalized ideal center value.

By introducing a reflective boundary condition in Geometry 2, the issues associated with the loss of thermal neutrons with a near-infinite sink are eliminated. Geometry 2 still has the issue associated with self-shielding, but localized at the ends of the homogenized fuel bundle. This localisation of self-shielding is created by the method in which data is collected. To obtain outputs along the length of the homogenized bundle, the bundle was segmented axially into smaller cylinders, as shown in Figure 5.3.

When segmenting up the region in this manner, even though neutrons may not be able to deeply penetrate the homogenized bundle, they still are included in the output tally. Since the segments are only divided axially and not radially, they span the entire radius of the homogenized bundle. This means that the output is more sensitive to axial self-shielding than radially self-shielding. This is demonstrated in the above figure, where the black arrows denote neutrons which are included in a tally even though they do not deeply penetrate the homogenized bundle. Whereas, the red arrows represent neutrons that are also counted in the output but only for a few axial segments since they are unable to penetrate beyond X segments. This increased sensitivity to axial self-shielding leads to the dips in axial flux which occur between the center and end of the homogenized fuel bundle in Geometry 2.

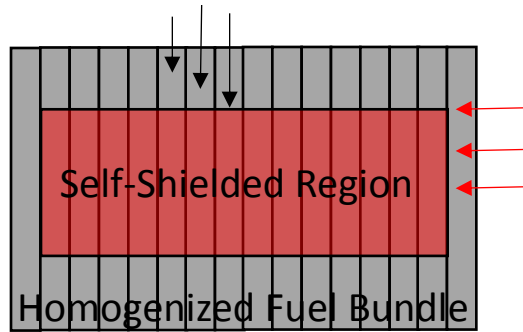


Figure 5.3: Axially segmented homogenized fuel bundle to obtain axial-flux output

Therefore, simplifying the CANDU bundle geometry does not capture all physical phenomena associated with EFP. It is necessary to use a model which incorporates the individual 37-element design associated with CANDU fuel bundles as demonstrated by Model 3. Aside from some minor simplifications associated with the shape of the end-cap and end-plate, Geometry 3 is a model of a realistic CANDU 37-element fuel bundle. However, just because the simplifications done in this project proved to affect the results negatively, does not mean that simplifications can never be made to obtain accurate results. For example, Balaceneau and Hristea [3], used codes PIJXYZ and LEGENTR, their model was two simplified half-CANDU-fuel bundles including the contact region. The half-fuel bundles made use of concentric ring interchanging between fuel and sheath as material. Using this simplified model, they were able to predict EFP values, as shown in Table 5.1,

Table 5.1: Calculated end flux peaking factors for NU-37 at nominal power from Balaceneau and Hristea [3]

Fuel Ring	End Flux Peaking Factors in NU-37		
	PIJXYZ	LEGENTR	Experimental
<i>Center</i>	1.2634	1.2885	1.268
<i>Inner</i>	1.2321	1.2602	1.240
<i>Intermediate</i>	1.1787	1.2031	1.205
<i>Outer</i>	1.1041	1.1271	1.142
<i>Average</i>	1.1946	1.2197	1.214

Note: Error on each calculated value is less than 3.0%

## 5.2 KCODE Cycle Determination

To obtain accurate results from the model, characteristics of the KCODE calculation must be defined by the user. Some of the parameters that the user needs to specify while using the KCODE calculation are the number of neutrons simulated per cycle, the number of cycles after which the calculation begins and finally the number of cycles to be completed. The second input parameter is included to allow the spatial distribution of source neutrons to converge to a realistic distribution for each specific problem. Generally, this parameter equals 10% of the maximum number of cycles. For the final model, a parametric study was performed on the maximum number of cycles for the KCODE calculation. The reason for performing a parametric study on the number of cycles is twofold. If the number of cycles is too small, the error on the results will be large. On the other hand, if the number of cycles is too large, the run time for a single trial would be too long. Longer run times mean that less trials can be run in a given time frame, hindering the ability to obtain an accurate value for the amount of absorber needed to mitigate the EFP. The results of this parametric study are summarised in Figure 5.9 below, with N representing the number of KCODE cycles. The values for the other two KCODE input parameters were fixed for the parametric study. The number of neutrons per cycle was set to 100000 and the number of cycles before the start of the KCODE calculation was 200. The parametric study included cycles ranging from 200 to 2400.

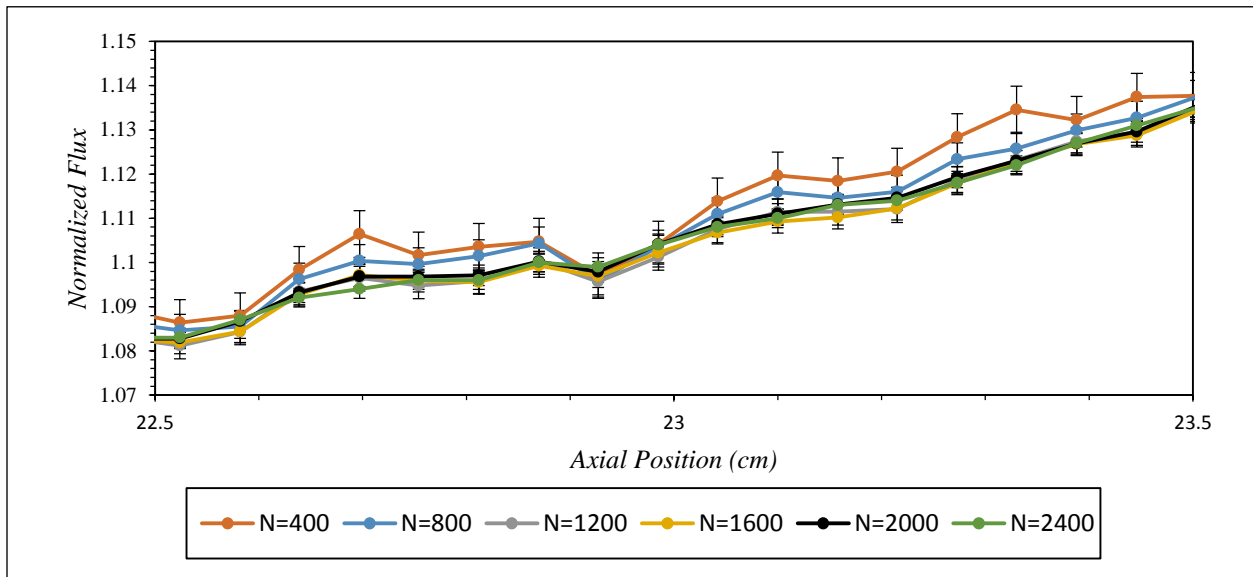


Figure 5.4: Results of parametric study for number of KCODE cycles

From the above figure, the optimal number of cycles from the parametric study was determined to be 2000. It was determined that 2000 cycles, provided a reasonable smoothness to the curves while taking a reasonable amount of time to complete the calculation. The total duration for a trial to complete was 4.5 hrs with the determined 2000 KCODE cycles.



## 5.2.1 Error Calculation

Now that the ideal number of KCODE cycles has been found, it is important to demonstrate the amount of error associated with the EFP results. To demonstrate the amount of error associated with the EFP results, the dependence of the EFP error on the number of cycles will be calculated. To determine the dependence of the EFP error on the number of cycles, the largest relative error included in the mesh tally taken from each output of the parametric study will be compared. By taking the largest relative error, a conservative estimate of the cycle number dependence on EFP error will be provided. When comparing these conservative estimates against each other from the parametric study, the trend of EFP error versus cycle number will be demonstrated.

Since MCNP includes relative and not absolute errors in the mesh tally output, a calculation must be performed to convert from relative to absolute error. To convert between relative and absolute errors, Equation 5.2.1 is needed:

$$Abs. Error = Rel. Error \times Value \text{ being measured} \quad 5.2.1$$

Once the relative errors are converted to absolute errors, percent error associated with the EFP value can be calculated using Equation 5.2.2. In Equation 5.2.2,  $\delta q$  represents the error associated with the EFP value,  $|q|$  is the absolute value of the EFP value,  $\delta x$  and  $\delta y$  represent the error associated with the flux values in the numerator and denominator of Equation 3.9.1 respectively. Finally,  $|x|$  and  $|y|$  represent the absolute value of the flux values in the numerator and denominator of Equation 3.9.1.

$$\frac{\delta q}{|q|} = \left[ \sqrt{\left(\frac{\delta x}{|x|}\right)^2 + \left(\frac{\delta y}{|y|}\right)^2} \right] \times 100\% \quad 5.2.2$$

Performing the calculation provided by Equation 5.2.2 on the largest relative errors from the parametric study provides the results summarised in Figure 5.5.

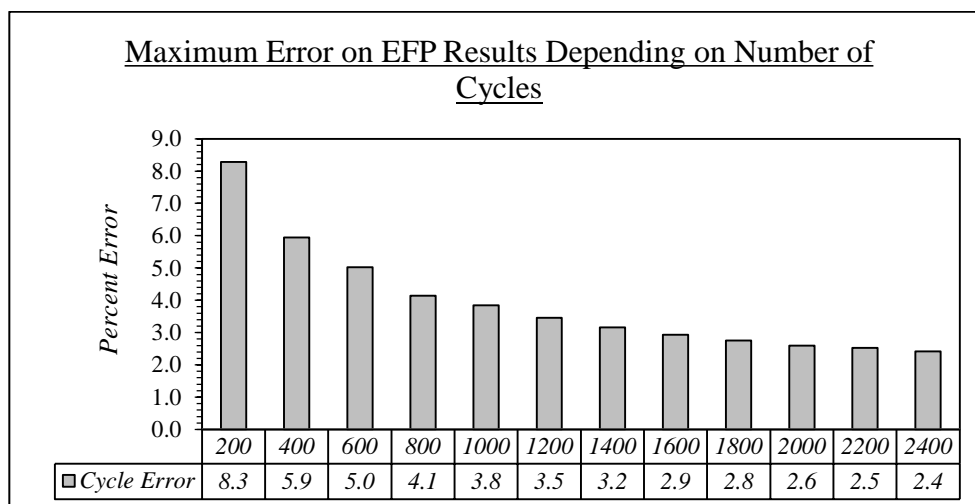


Figure 5.5: EFP error calculation on results from parametric study to demonstrate relationship between number of KCODE cycles and relative error

From Figure 5.5, as the number of cycles increases, the max percent error associated with the EFP value decreases. From the parametric study, it was determined the 2000 KCODE cycles provided the

best-case scenario which minimized the variation in the EFP results while minimizing the time to complete an trial. As shown in Figure 5.10, 2000 cycles fall in a region where successive increments in cycle number yield minimal gains in decreasing percent error. This is indicated by the percent error for 2200 cycles differing by roughly 4% from 2000 cycles,  $(|2.5 - 2.6|/2.6 \times 100\% \approx 4\%)$ . While for earlier trials, for example going from 200 to 400 cycles, the error differs by roughly 29%,  $(|5.9 - 8.3|/8.3 \times 100\% \approx 29\%)$ . This further reinforces the choice of using 2000 KCODE cycles for all further MCNP trials.

Note, since 2000 KCODE cycles will be used for all further MCNP trials, the error associated in the results will always be less than or equal to ~3%. As indicated by the max percent error on the EFP value from the parametric study shown in Figure 5.5.

### 5.3 Model Validation

To ensure that the model was able to predict the correct values for the peaking factors, comparison was done to experiments performed at the ZED-2 reactor at the Chalk River Nuclear Laboratories (CNL) and to a similar model performed with DRAGON 3.03a. It should be noted that the DRAGON model makes use of the 89-group ENDF/B-V library, while the MCNP 6.1 model uses the more up to date ENDF/B-VII.1 library. Since the MCNP model is making use of a more up-to-date material library, this may help account for its improved performance in predicting the peaking factors when compared to the DRAGON model. Results are summarized in Table 5.2,

Table 5.2: MCNP 6.1 model comparison [1] [31]

Fuel Ring	End Flux Peaking Factors in NU-37		
	Experimental	DRAGON	MCNP 6.1
<i>Center</i>	1.268 ± 0.014	1.257 (-0.9)	1.265 (-0.2)
<i>Inner</i>	1.246 ± 0.014	1.236 (-0.8)	1.248 ( 0.2)
<i>Intermediate</i>	1.205 ± 0.013	1.194 (-0.9)	1.212 ( 0.6)
<i>Outer</i>	1.142 ± 0.009	1.127 (-1.3)	1.142 ( 0.0)

Note that the values in brackets beside the peaking factors represent the percent difference from the experimental results for each simulation. From Table 5.2, the model in MCNP is able to accurately predict the peaking factors of each fuel ring, within 1%. MCNP allows for the user to include more physical detail in their model and therefore allows for more robust models with fewer simplifications.

Using this model, trials were done to determine the amount of neutron absorber to be placed within several locations within the fuel bundle deemed the most likely to demonstrate significant mitigation of EFP. Another relevant conclusion drawn from Table 5.2 is the peaking factors for fuel elements in each fuel ring have different values. This indicates that the amount of absorber need to successfully mitigate EFP in each fuel ring will differ on a ring-by-ring basis.

The next method to validate the MCNP model is to compare the RPPF values predicted by MCNP with those obtained from correspondence with industry experts. These results are summarized in Figure 5.6. In Figure 5.6, the red columns represent the RPPF values predicted by MCNP, while the black columns represent the values obtained from literature. Also, included in the figure are the blue columns representing the absolute percent difference between these two values, hereby referred to as the reference value.

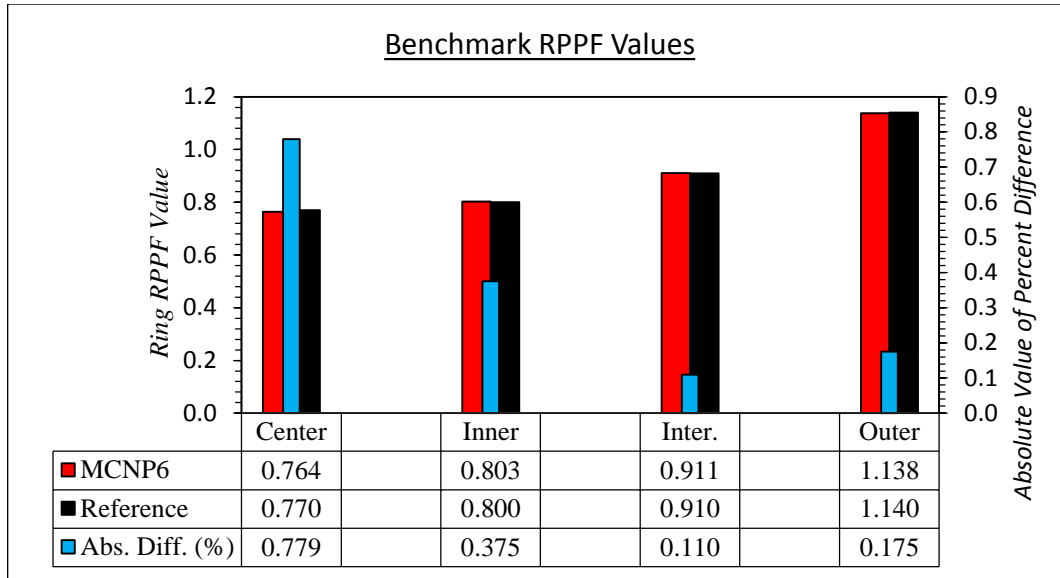


Figure 5.6: RPPF comparison between MCNP 6.1 model and values taken from correspondence with CAMECO

Below the graph in Figure 5.6, the RPPF values predicted by MCNP and those from literature along with the exact absolute value of the relative percent difference are provided. Note the percent difference between the reference and MCNP predicted results were determined using Equation 5.3.1.

$$Diff. (\%) = \frac{RPPF_{MCNP} - RPPF_{REF}}{RPPF_{REF}} \times 100\% \quad 5.3.1$$

where  $RPPF_{MCNP}$  is the ring-dependent RPPF value determined by MCNP, and  $RPPF_{REF}$  is the reference ring-dependent RPPF value.

From Figure 5.6, the observed percent across all fuel rings is less than 1.0%, with the largest difference observed in the center element. The absolute percent difference for the center element is roughly two times the next largest percent difference and roughly six times the smallest percent difference. The value of the absolute percent error in the center element should be noted for future RPPF comparisons as it will lead to larger deviations when absorber is added to the fuel bundle.

The error on the percent differences can be calculated using Equation 5.3.2 which is a combination of the various error analysis rules associated with addition, subtraction, multiplication and division of values with associated errors. Note that the absolute error on the reference values is  $1.0 \text{ E}^{-3}$  and the relative error on the MCNP values is  $3.0 \text{ E}^{-4}$ . Since MCNP outputs relative errors, they must first be transformed into absolute errors by multiplying by the predicted ring-dependent RPPF value.

$$\partial Diff. (\%) = |Diff. (\%)| \sqrt{\left(\frac{\sqrt{(\delta RPPF_{MCNP})^2 + (\delta RPPF_{REF})^2}}{(RPPF_{MCNP} - RPPF_{REF})}\right)^2 + \left(\frac{\delta RPPF_{REF}}{RPPF_{REF}}\right)^2}$$

where the first term under the first square-root is the error for the numerator of Equation 5.5.1, and the second term is the error for the denominator of the same equation. Performing this equation for each fuel ring provides an error on the percent difference of roughly 0.1% or an absolute error of 0.001. The value of error with the percent difference is on the same order as the benchmark percent differences.

## 5.4 MATLAB Automation

To streamline the process of creating and running many input decks within MCNP, MATLAB scripts were created which automate both of these processes. The automation of running each of the MCNP input deck was done using batch files. The function of the automatic input scripts was to edit an existing MCNP input deck template to generate a series of new trials. These input decks use strings of text as placeholders for the values of material density and isotopic percentage for the doped fuel material. These string placeholders are replaced with values calculated by the script for each trial in a series.

To run each set of trials, a batch file was created, which when run in a command prompt would sequentially execute the trials within MCNP. Upon completion of each trial, MCNP provides the following output files, *filename*r.txt, *filename*s.txt, *filename*o.txt and *filename*msht.txt, where the *filename* is the name of the file being run. The output files will be referred to as the r-file, the s-file, the o-file and the msht-file, respectively. Both the r-file and s-file are used to store information about the run, and are updated after each KCODE cycle. In the event of mid-run termination, the r-file and s-file contain the necessary information to pick up the run prior to the termination. In terms of output data, the r- and s-files contain no information that can be analyzed. The o- and msht-file are the two files which contain the outputs from the tallies designated in the input deck. The o-file is the general output file in MCNP, regardless of the tallies specified in the input deck. The o-file contains information about which data tables were used, outputs for all non-mesh tallies used, and error associated with the results.

As done with the input files, two automation MATLAB scripts were created to obtain the key outputs from the o- and msht-files. The principle function of these scripts is to search through each output file for key outputs, then read these values into Excel files. The Excel files are formatted to perform calculations and generate graphs. Figure 5.7 provides a schematic representation of the automation process used to streamline the work done in this project. The all necessary files for the automation process are provided in Appendices A.3 to A.6.

The first box in the primary chain of the schematic in Figure 5.7 is the generic MCNP input file. An example section of the general MCNP input deck formatting is provided in Appendix A.3. In the generic MCNP input deck, string placeholders exist for the density of the doped fuel, and the abundance of each isotope in the doped fuel. These string placeholders take the form *XXXXXXXXXXXX*, where *X* stands for a single letter in the alphabet. The length of the string placeholder is of importance since it indicates the amount of precision the values it is holding a position for will have. It was decided that ten positions for numeric entries including a decimal was sufficient. Note that the numbers were provided in scientific notation, therefore three places were needed for the “E”, the negative sign, “-”, and the number indicating the order of magnitude. For example, if the number was  $1.23456789E - 1$ , the last three positions are occupied by “E - 1”, with the first ten occupied by “1.23456789”, including the decimal

period. Other than the string placeholders, the input file has no other unique features separating it from any other MCNP input deck.

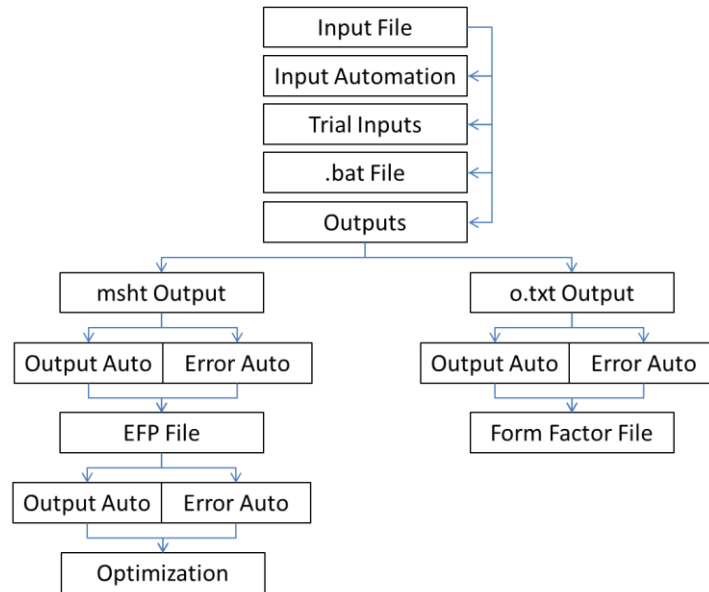


Figure 5.7: Automation scheme for absorber trials

The second box in the primary chain of the schematic is the input automation file shown in Appendix A.4. This file is a MATLAB script, which when provided with a range of BNA to be added to the fuel pellets, generates N-unique MCNP input files. This MATLAB automation script also includes a list of physical constants needed to calculate the density and isotopic abundances of the doped fuel. The calculations performed in the input automation script follow the steps outlined in Section 4.5. The script then reads in the generic MCNP input file, locating the string placeholders. The calculated values are then converted to text and replace their respective string placeholders. For example, if the user were running a set of trials ranging from 100 mg to 150 mg of  $\text{Eu}_2\text{O}_3$ , with trials being conducted every 10 mg, there would be six unique MCNP input files generated by the automation script. One script for every milligram amount of  $\text{Eu}_2\text{O}_3$  added to the fuel bundle in the example range.

The third box in the primary chain of the schematic is the input files resulting from the previous MATLAB automation script. The fourth box in the primary chain is a batch script used to sequentially run the multiple inputs generated by the input automation script. An example of this batch script is shown in Appendix A.5. Batch scripts are lists of MS-DOS commands. These MS-DOS commands are executed in the Windows command prompt. For the purpose of automating trials, commands were included in the batch scripts which execute trials sequentially. The particular commands used in the automation process includes: filepaths to specify particular directories and commands which execute scripts or input decks within these specific directories.

The fifth box in the primary branch is the outputs. The outputs include two separate files, as indicated by the primary branch splitting at this point. The branch of more importance to the EFP results is the left branch. The right branch is included to calculate the RPPFs as discussed in Section 3.9. The RPPF provides a check to ensure that the power of the fuel elements is not altered drastically by the addition of BNA. Contained in both branches are the boxes labelled “Output Auto” and “Error Auto”. As the names indicate, the scripts at this point are for manipulating the outputs and their associated errors. An

example of these output manipulation scripts is provided in Appendix A.6. The function of these MATLAB scripts is to take the values for the outputs-of-interest from MCNP output file and place the values into pre-formatted Excel files to generate graphs. The benefit of using pre-formatted Excel files to generate the graphs is it allows for easier post-processes of the outputs-of-interest than the text output provided by MCNP or running a MATLAB script every time a graph needs to be edited. All subsequent output and error automation scripts in the schematic shown in Figure 5.7 perform similar tasks and make use of similar techniques as demonstrated in Appendix A.6. The techniques utilized by these MATLAB scripts are user-specified but MATLAB-generated functions, referred to as “*importfile*” and “*importerror*” and are shown in Appendix A.7 and A.8, respectively. These functions are created by importing the MCNP output file into the MATLAB project directory then performing the necessary data manipulation and using MATLAB’s functions generating capabilities. For the purposes of this project, the generated functions select the outputs-of-interest and assign them to an array for further manipulation by the MATLAB scripts.

## 5.5 Absorber Location Testing

For absorbers to be effective, they need to be placed strategically in the end region. The absorbers need to be located closely to the locations most affected by EFP. Another consideration is that the location of the absorbing material must have minimal impact to the fuel bundle design. To determine the optimal location for the neutron absorber to be placed, various locations were investigated, with various amounts of absorbing material, either gadolinium or europium oxide. The locations of interest include: the end pellets; thin disks located in the gap between the end pellet and the end cap; layer of CANLUB coating, and the endplate itself. For all locations except the endplates, the absorbing materials are in their oxide forms. For the absorbing material in the endplates, the europium and gadolinium is alloyed into the Zircaloy-4.

### 5.5.1 Thin Disks

The first absorber location is in the form of thin disks which occupy the gap between the end pellet and the end cap. The thickness of the disks is roughly 0.1 mm. The benefit of having the neutron absorbing material located in thin disks is that it allows for the introduction of the absorbing material without having to alter existing bundle materials. A drawback of this design is that the thin disks will occupy physical space between the end pellet and the end cap. This gap is included in the fuel element designed to accommodate the axial pellet expansion during reactor operation.

Trials using the thin disks of absorbing material were done using 5 mg, 10 mg, 15 mg, 20 mg and 25 mg of either europium or gadolinium oxide. These results are summarized in Figure 5.8, which illustrates the end region of a center element. Note that the dashed horizontal line indicates an ideal situation of the flux being uniform across the length of fuel element.

Even though thin disks seem like the easiest location to implement, having neutron absorbers located in a compact volume caused dipping of the flux at the location of the thin disks. This flux dipping is more severe when gadolinium oxide is chosen as the absorbing material because gadolinium has a larger thermal neutron absorption cross section than europium. Even though the flux dips at the location

of the thin disk, there does appear to be a slight improvement in the end flux peak when compared to having no absorber in the fuel bundle. The flux dipping caused by the implementation of absorbing material as thin disks leads to a more complex flux profile while not mitigating EFP to the desired magnitude, the use of thin disks is not considered for further trials.

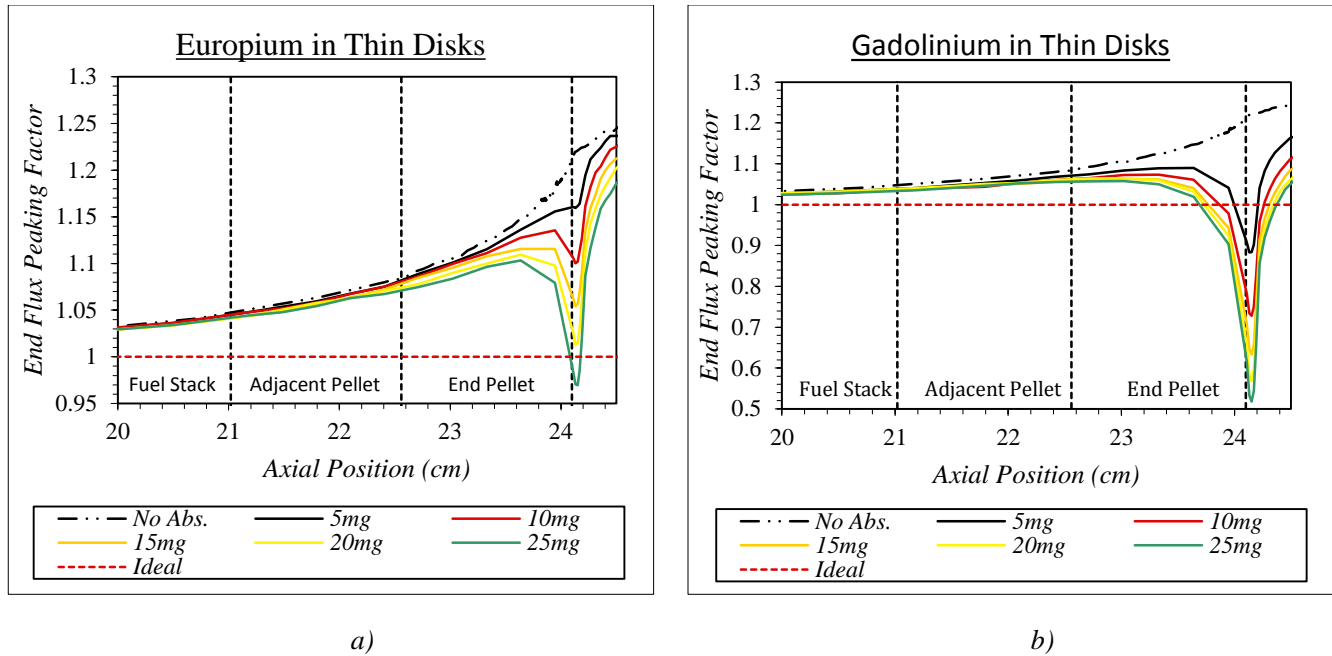


Figure 5.8: Trial results using neutron absorbing material in thin disks

## 5.5.2 CANLUB

The next absorber location of interest is to mix the absorbing material into the CANLUB coating. In the case, the neutron absorber is mixed into the CANLUB of all 37 fuel elements. Therefore, the absorbing material is assumed to be distributed uniformly throughout the entire fuel bundle.

Trials were done using 5mg, 10mg, 15mg, 20mg, 25mg and 30mg of either europium or gadolinium oxide, per element. These results are summarized in Figure 5.9, which illustrates the end region of a center element.

From the above figures, it is apparent that the axial flux curve for trials where neutron absorber is added into the CANLUB are higher than the no absorber case. This higher axial flux curves are due the fact that absorbing material is distributed uniformly along the length of the fuel elements. By uniformly distributing the absorbing material in the CANLUB, not only mitigates the neutron flux in the end regions but also along the entire length of the fuel element. Coupling the uniform mitigation with the fact that Equation 3.8.1 relies on taking a ratio of the flux in the end region over the flux at the center of the fuel bundle, leads to the end flux peaks appearing larger for cases involving the addition of absorbing material. Mixing the absorbing material into the CANLUB coating is excluded from further trials.

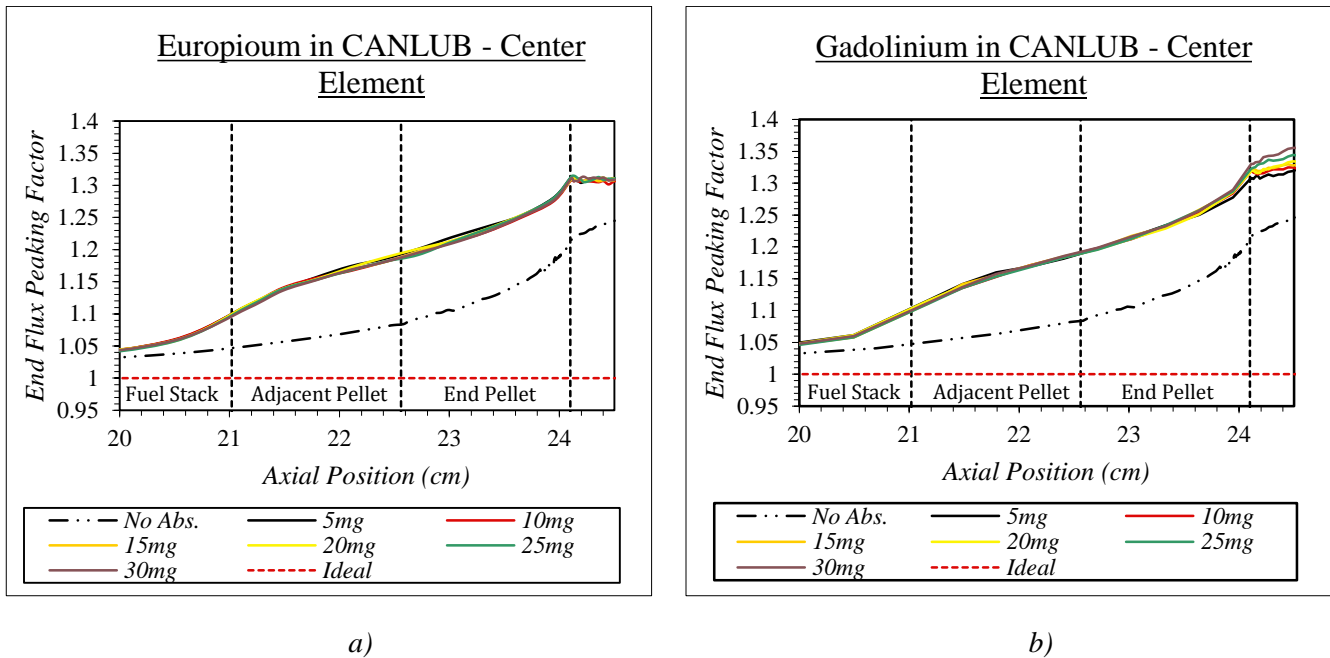


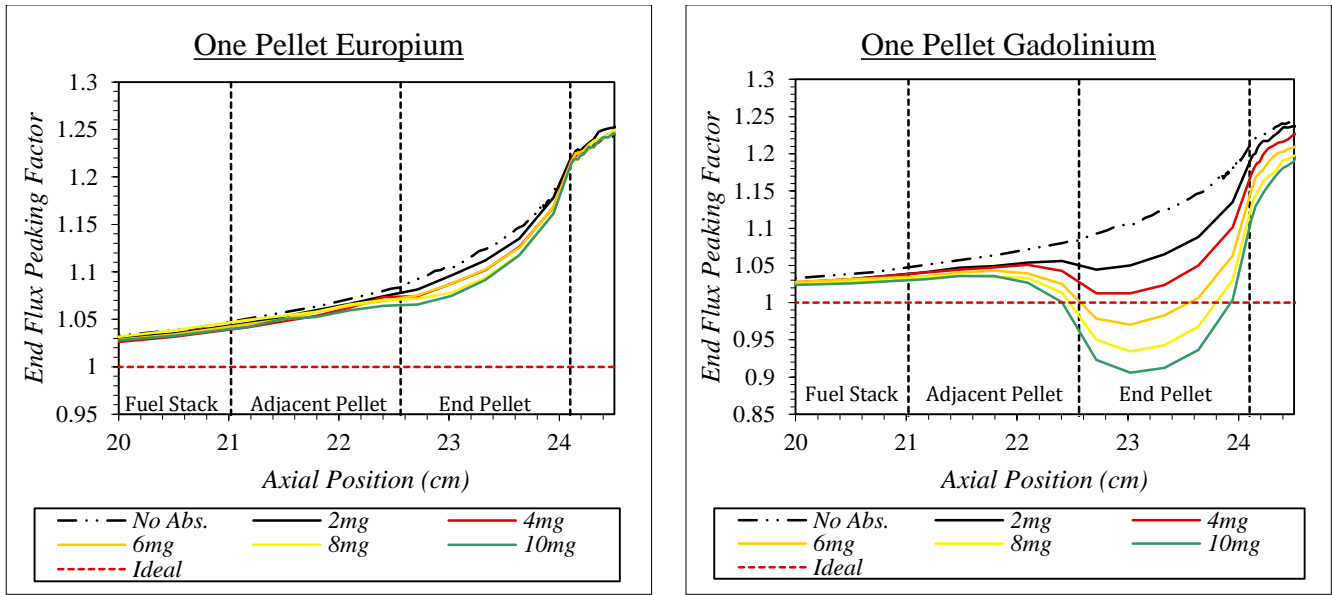
Figure 5.9: Trial results using neutron absorbing material mixed in the CANLUB layer

### 5.5.3 End Pellets

The third location considered for the absorbing material to exist is within the end pellets. End pellets are fuel pellets which are located at either end of the fuel stack. To include the absorbing material into the end pellet it must be incorporated into the fuel matrix. Having the absorbing material incorporated into the fuel matrix represents a beneficial design to mitigate EFP for several reasons. Mixing the absorbing and fuel material negates the need to introduce new equipment into the fuel manufacturing process. Also, as shown in the previous figures, EFP is a phenomenon not localized to a single pellet in the fuel stack. When no absorbing material is present the EFP curve is not localized to the endplate and end cap. Instead, the curve seems to have extended to a few pellet lengths into the fuel stack. These multiple pellets at bundle ends are of highest risk of centerline melting during accident conditions.

A potential drawback is the fuel pellets containing the absorbing material will be visibly indistinguishable from other fuel pellets. During the fabrication of a doped CANDU fuel bundle, the doped pellets could get misplaced within the fuel stack, instead of being placed as end pellets. In practice, end pellets are either shorter, chamfered or smaller in diameter than other fuel pellets. These design features help to distinguish end pellets from other fuel pellets thereby mitigating the risk associated with doped end pellets being loaded into the other positions along the fuel stack. Results using a single end pellet and doping it with 1 to 10 mg of the respective absorbing material, incremented by 1 mg are illustrated in Figure 5.10.





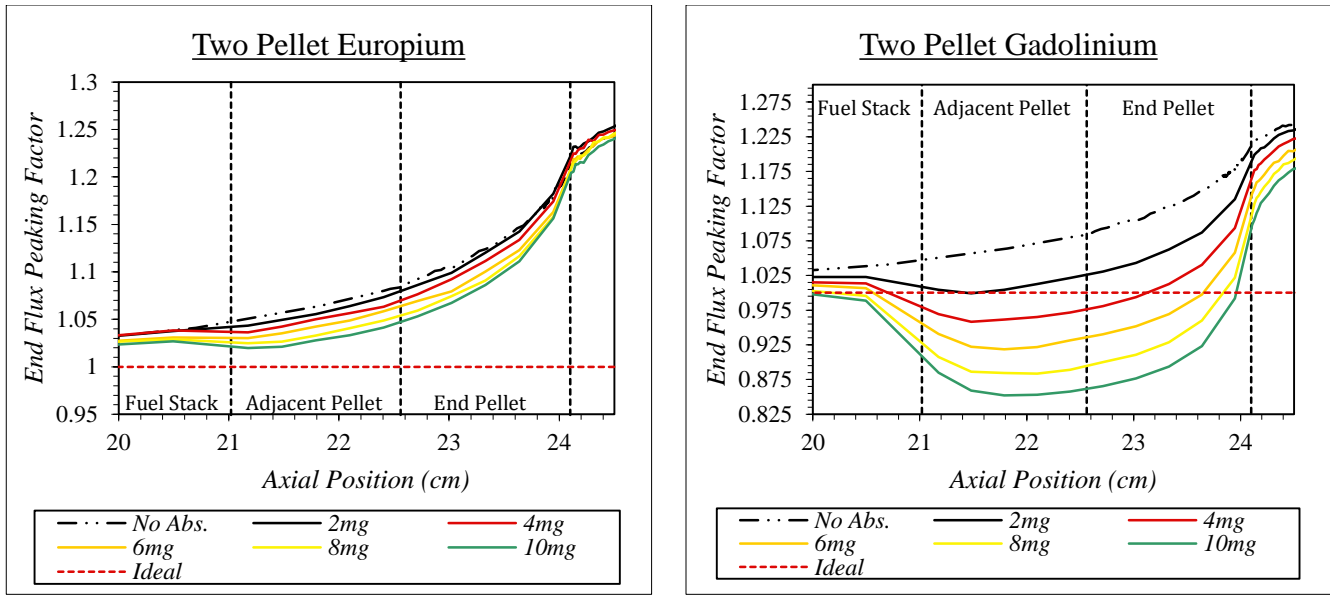
a)

b)

Figure 5.10: Trial results using neutron absorbing material mixed in a single end pellet

As shown in Figure 5.10, the europium in the single end pellet configuration brings the flux peak towards the ideal line in a smoother fashion when compared to gadolinium. For both europium and gadolinium in the single pellet configuration, mitigating potential is limited to the end pellet in which the absorbing material was added. This localization of mitigating potential is apparent in Figure 5.15b. In the “End Pellet” region of the graph, the end flux peaking factor drops below the horizontal “Ideal” dashed line. Yet just beyond the “End Pellet” region, in the “Adjacent Pellet” region, the end flux peaking factors are greater than the horizontal “Ideal” dashed line. This difference across in the flux curve across the span of just two fuel pellets indicates the mitigating potential provided by incorporating the absorbing material into the fuel matrix is fairly localized. This observation is supported by Figure 5.15a. However, since europium has a lower thermal neutron absorption cross section than gadolinium the localized mitigating potential is less pronounced. Therefore, by incorporating absorbing material into a single end pellet, a significant mitigation of the flux peak is observed primarily within the end pellet.

As shown in Figures 5.8, 5.9 and 5.10, there is still significant peaking in the adjacent end pellet. To address this issue, europium and gadolinium oxides were also placed into both the end and the adjacent-end pellets. Similar to the single pellet cases, calculations were done for each pellet with 1 to 10 mg of the respective absorbing material; incremented by 1 mg. For the preliminary trials the same amount of absorbing material was added to each pellet. So, for a case which specifies 10 mg of europium oxide, 10 mg of  $\text{Eu}_2\text{O}_3$  was added to the both the end and adjacent-to-end pellets. This would equate to a total of 20 mg per one end of a fuel element, or a 40 mg for one entire fuel element. Figure 5.11 summarizes these results.



a)

b)

Figure 5.11: Trial results using neutron absorbing material mixed in two end pellets

Similar to the single end pellet configuration, europium oxide is able to provide a more controllable option to mitigating EFP. This controllable EFP mitigating potential is demonstrated in Figure 5.16a where the flux curve steadily approaches the horizontal “Ideal” dashed line for each increment of europium oxide added. Another feature shared between the single and two end pellets configurations is the ability of gadolinium oxide to drastically alter the observed flux curve. With the absorbing material being added to two pellets instead of one, the severity in which gadolinium affects the flux curve is increased. The increase in severity is due to the increased amount of gadolinium present in a small physical location, occupying the volume of two fuel pellets. However, the benefit of having the absorbing material added to two pellets instead of one allows the flux peaks to be more completely mitigated. This more complete mitigation of the EFP peak is demonstrated in Figure 5.11 by portions of the EFP peak within the “Adjacent Pellet” and Fuel Stack” regions approaching the horizontal “Ideal” dashed line than it was with the single end pellet trials. Since there is variation in the amount of EFP occurring between the “Adjacent Pellet” and “End Pellet” regions, it may be necessary to consider trials where the amount of absorbing material in the two end-pellets be different.

Even by increasing the number of doped end pellets to two, although mitigated, flux peaking still exists with the “Fuel Stack” region. Though no three pellet configurations were investigated, the two-pellet configuration is already complex enough of a design change.

## 5.5.4 Endplates

Unlike the previous locations, adding the absorbing material to the endplates alloy does not involve the addition of oxide materials. Instead pure europium or gadolinium metal would need to be included to form either a Zircaloy-4-Europium or –Gadolinium alloy material. The inclusion of this absorbing material location was due to trials conducted at Canadian Nuclear Laboratories (CNL) where different endplate alloys were investigated to mitigate EFP. However, using the endplates as a location for

gadolinium and europium is highly discouraged as a practical method. During operation, the gadolinium and europium in the alloy would constantly be changing through neutron capture reactions, raising concern over the structural integrity of the endplate during reactor operation. Regardless, Figure 5.12 demonstrates the ability of endplates alloyed with neutron absorbing material to mitigate EFP.

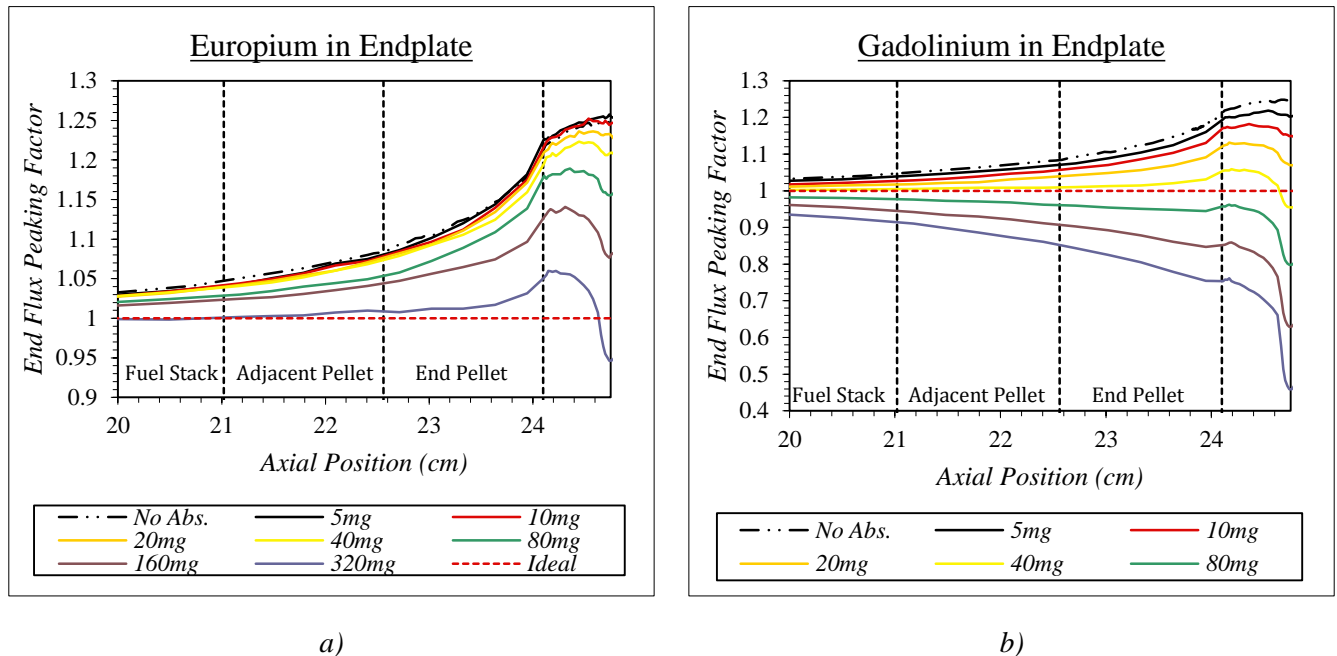


Figure 5.12: Trial results using neutron absorbing material mixed in the endplate

Similar to previous analysis, the europium seems to provide the more controllable option of absorbing material when compared to gadolinium. This is demonstrated in Figure 5.12, when comparing the addition of similar amount of europium or gadolinium into the endplates. Again, the addition of gadolinium tends to drop the flux curve below the horizontal “Ideal” dashed line. Similar amounts of europium cause a less severe flux curve response. As shown in Figure 5.12, the addition of absorbing material in the end plates provides excellent mitigation potential.

It should be noted, even though a drop of the flux curve does appear in both graphs in Figure 5.12, this is not an issue because they occur in the region beyond the “End Pellet” region. Unlike previous cases, both Zircaloy-4 and heavy water contain no material which undergoes fission.

As mentioned, the endplates are a structural component of the fuel bundle and therefore adding absorbing materials are highly discouraged. By adding any new material into the Zircaloy-4, the physical and chemical properties could be altered. This complicates the manufacturing and qualification process for new alloy to be used as a structural material.

### 5.5.5 Ring-Optimized Absorber Amounts

From the preliminary gadolinium and europium trials done thus far, the following conclusions can be obtained. Firstly, the best location for mitigating EFP is the double end pellet configuration. Secondly, gadolinium has too large a neutron absorption cross section to smoothly mitigate EFP by itself.

Therefore, the best absorber and absorber location is to have europium placed into the adjacent and end pellets. From Figure 5.11a, it is clear that the amount of europium in the pellets investigated needs to be optimized.

### 5.5.5.1 Least Squares Optimization

To determine the effectiveness of adding absorber to the two end pellets, a score is established using the least squares method. The least squares method was implemented using a Python script provided in Appendix A.9. The function which provides a score makes use of the ideal solution of a flat axial flux instead of experimental values. The optimal case for each set of trials was determined as the trial with the lowest score. Once the trial with the lowest score was determined, a new set of trials was created using a smaller amount of added absorber. This process was repeated until the final optimal trial was discovered. The following figure demonstrates the process used to find the optimal values,

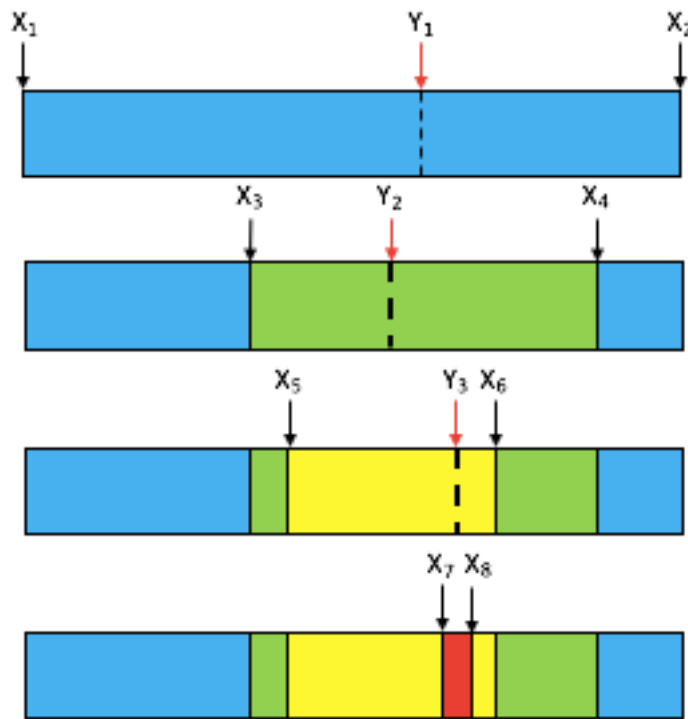


Figure 5.13: Process by which the optimal values were found

The  $X_i$  values in Figure 5.13 represent the bounds to which a set of trials was conducted. For each trial a set a figure of merit is obtained using the Least Squares Method, and the best value obtained is  $Y_i$ . The  $Y_i$  values then become the new central point of interest for the next iteration of trials. With the  $X_i$  values representing the start and end point of the new range of interest. After each set of trials, a smaller delta mass of  $\text{Eu}_2\text{O}_3$  between each trial in a set is taken. This process is repeated until the optimal absorber value is discovered.

An example of this optimization routine demonstrated in Figure 5.18 is provided below,

Example:

Iteration 1:

- Trials conducted with 20 mg, 40 mg, 60 mg, and 80 mg of a BNA
- The mass delta in this iteration is 20 mg
- It was determined that 40 mg provided the best score

Iteration 2:

- Change the mass delta to 10 mg and the center point in the range to be 40 mg
- Trials conducted at 30 mg, 40 mg, 50 mg
- It was determined that 30 mg provided the best score

Iteration 3:

- Change mass delta to 5 mg and center point in the range to be 30 mg
- Trials conducted at 25 mg, 30 mg and 35 mg
- It was determined that 25 mg provided the best score

This process will repeat until the mass delta is 1 mg and the best scoring BNA amount is determined.

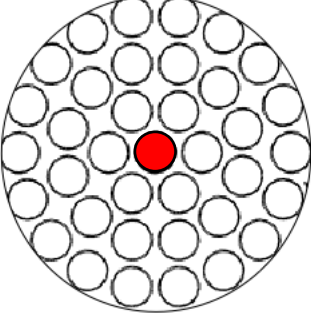
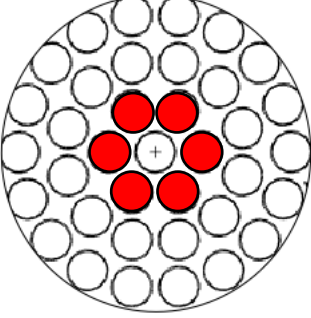
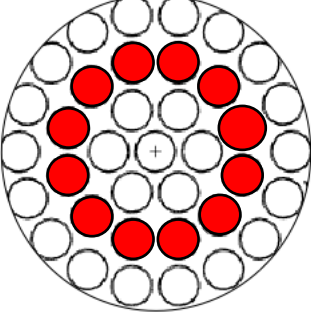
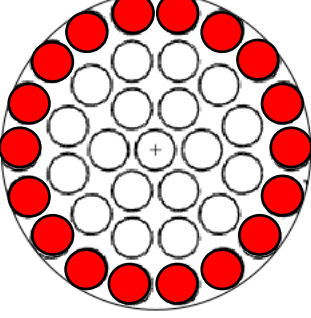
Using an optimization routine, the optimal amount of europium oxide added to both pellets in fuel elements from each fuel ring was determined. From this point forward the results summarized below will be referred to as ring-optimized. The term ring-optimized refers to a case where the optimal amount of  $\text{Eu}_2\text{O}_3$  is added to a single fuel ring only. Therefore, four separate ring-optimized cases will be presented in this section. They are; the center-optimized, the inner-optimized, the intermediate-optimized and the outer-optimized case.

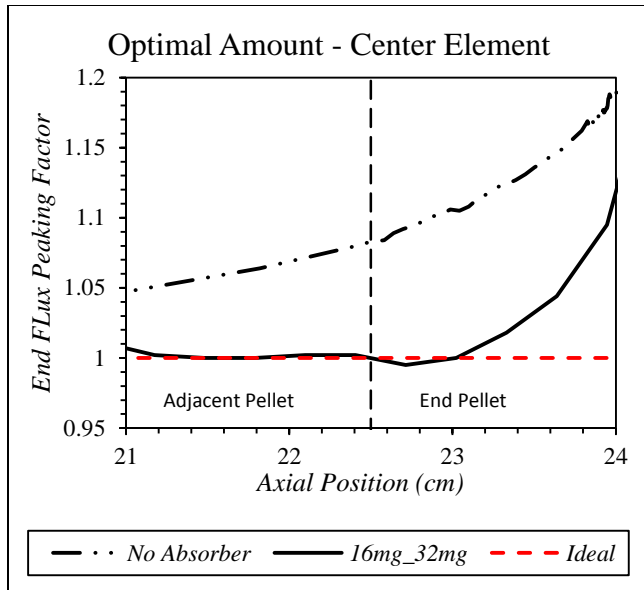
The results of each one of these ring-optimized results are summarised in Figure 5.14. Prior to Figure 5.14, Table 5.3 demonstrates the location of the absorber added to the fuel bundle for each ring-optimized case. Note, the red circles indicate fuel elements which have  $\text{Eu}_2\text{O}_3$  added to their fuel pellets. Note that the total number of doped fuel pellets in each ring-optimized case will follow Equation 5.5.1.

$$\text{Num. Doped Pellets} = (2 \text{ Pellets in One end}) \times (\text{Num. Elements in Ring}) \times (2 \text{ Ends}) \quad 5.5.1$$

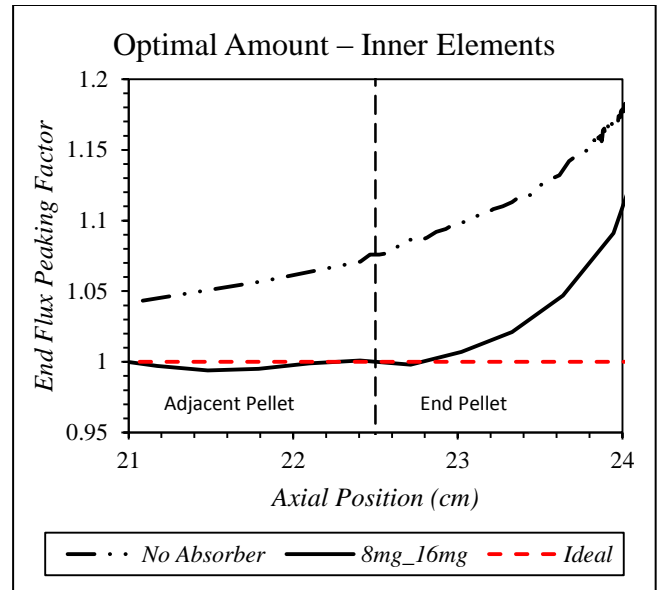
Note that the first number in the absorber curves indicates the amount of europium added to each individual adjacent pellet and the second number represent the amount of europium added to each individual end pellet.

Table 5.3: Demonstrating location of  $\text{Eu}_2\text{O}_3$  in each graph of Figure 5.14

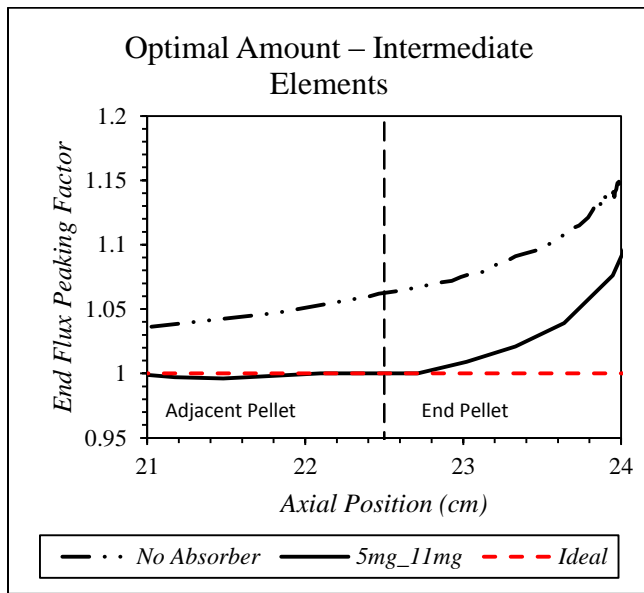
Figure Number	Description	Absorber Location
5.14a	<i>Center-Optimized</i>	
5.14b	<i>Inner-Optimized</i>	
5.14c	<i>Intermediate-Optimized</i>	
5.14d	<i>Outer-Optimized</i>	



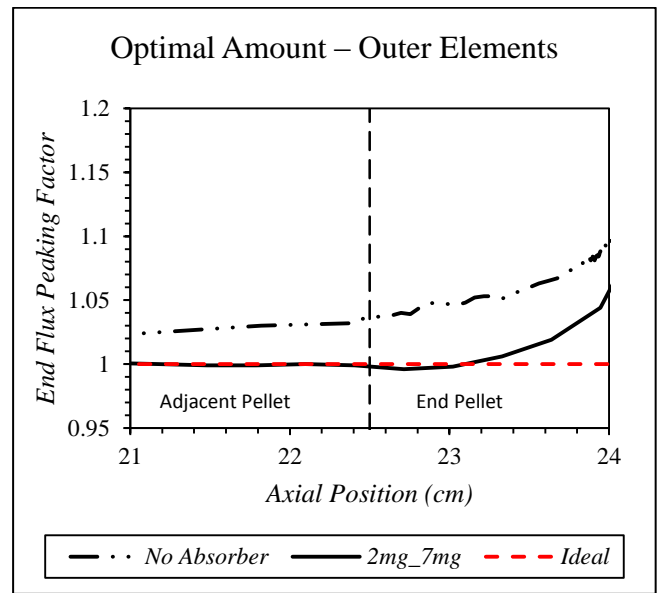
a)



b)



c)



d)

Figure 5.14: Ring-optimized results for the amount of  $\text{Eu}_2\text{O}_3$  placed into the both end pellets

Due to the exponential nature of the EFP curve, the amount of europium oxide added to the “End Pellet” region must be larger than the amount in the “Adjacent Pellet” region. The final consideration in distributing europium oxide across the entire fuel bundle is that the largest amount of europium oxide must be added to the center element. While the amount of europium oxide added in the surrounding rings will decrease as approaching the outer elements. The variability in the amount of europium oxide needed across the fuel rings is due to the variability in the peaking factor across the fuel rings, as shown in Table 5.3. Taking these effects into consideration and applying the optimization routine discussed, results in eight different doped fuel pellets. These eight different fuel pellets come from the four fuel rings with

each of the two fuel pellets in a fuel element experiences varying degrees of EFP. This solution, however optimal, is not strictly practical given the total number of different pellet designs that are necessary.

Although, when comparing the results for the doped fuel bundle to the non-doped in Figure 5.14, the EFP mitigating effect of adding specific amounts of europium oxide to specific fuel elements can be observed. Unfortunately, the optimal results are not able to completely eliminate EFP. The persistence of EFP even with an optimal amount of absorber added in a strategic location is due to the fact that the structural material remains the same as an un-doped CANDU fuel bundle. Regardless, significant mitigation of EFP has been demonstrated. This significant mitigation of EFP will decrease the risk of fuel centreline melting of the end pellets during accident conditions.

### 5.5.5.2 RPPF Results for Ring-Optimized Results

RPPF results for the ring-optimized trials are presented in this section. The goal is to ensure that the addition of  $\text{Eu}_2\text{O}_3$  into the end pellets does not adversely affect the power performance of the fuel bundle. Therefore, comparison will be to RPPF values that have no added BNA. If the RPPF results for the ring-optimized cases significantly differ from the reference values, the proposed design could have negative effects on the power performance of the fuel bundle. Since BNA are added to the fuel bundle, it is expected that the predicted and reference RPPF results will differ to some degree.

Note that all figures presented in this section follow the same format as Figure 5.6. The red columns represent the results predicted by MCNP. While the black columns representing the values taken from literature. Finally, the blue columns represent the percent difference between the MCNP predicted RPPF results and the reference values.

The RPPF values will also be compared to the benchmark values to gauge the effect of adding each of the ring-optimized amounts  $\text{Eu}_2\text{O}_3$  to the fuel bundle individually. The effect on the RPPF values will potentially indicate the existence of cross-ring effects. The term cross-ring effect refers to the ability of the  $\text{Eu}_2\text{O}_3$  place in one fuel ring affecting the flux curve within the other three fuel rings.

Figure 5.15 summarises the center-optimized results. Similar to the benchmark RPPF comparison, the center element has the largest percent difference between the predicted and reference RPPF values that is roughly 2%. However, recall from the benchmark RPPF comparisons, the benchmark center element also differs more than any other element in the other fuel rings. The RPPF value in the center element goes from 0.764 in the benchmark to 0.755 when  $\text{Eu}_2\text{O}_3$  was added to its adjacent and end pellet.

For fuel elements in the inner ring, the RPPF value has decreased to 0.801 from the benchmark value of 0.803. The RPPF values for the fuel elements in the intermediate and outer ring have also increased by 0.001 from 0.911 to 0.912, and 1.138 to 1.139 respectively.

The difference in RPPF value for the fuel elements in the intermediate and outer rings are within error, as calculated in Section 5.5.5. The difference in the center element is to be expected since the composition of the fuel is being altered. Since  $\text{Eu}_2\text{O}_3$  absorbs thermal neutrons that would otherwise be used in fission, it is expected that the RPPF value in the center element decreases in this case. But the difference between the RPPF values in the fuel elements of the inner ring is larger than error. This indicates that the addition of center-optimized amount of  $\text{Eu}_2\text{O}_3$  in the center element has an effect on the fuel elements in the inner ring.



The amount of difference between MCNP and literature values is small. This indicated that no significant alteration of the RPPF profile of a fuel bundle by adding center-optimized amount of  $\text{Eu}_2\text{O}_3$  to the center element.

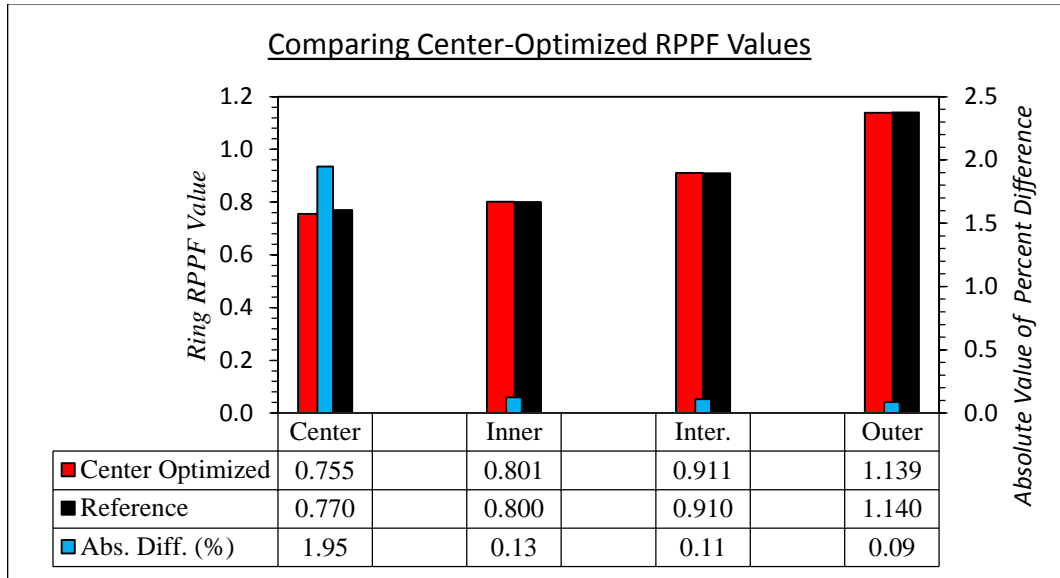


Figure 5.15: RPPF comparison between MCNP and literature values with center-optimized amount of  $\text{Eu}_2\text{O}_3$  was added to the center element

The next comparison is for the inner-optimized results. These results are summarized in Figure 5.16. Similar to the other RPPF comparison graphs indicated thus far, the largest percent difference is observed in the center element. However, the RPPF value in the center element did decrease from the benchmark value of 0.764 to 0.759 in this case. The difference between these two RPPF values is 0.005. This RPPF difference is five times larger than the error associated with the RPPF values as calculated in Section 5.5.5, meaning the difference in the center element cannot be accounted for by differences associated with the MCNP simulation. Therefore, the addition of inner-optimized amounts of  $\text{Eu}_2\text{O}_3$  in the fuel elements of the inner ring, must have some effect on the RPPF value of the center element.

By moving the  $\text{Eu}_2\text{O}_3$  to the inner elements, the RPPF value in the fuel elements of the inner ring becomes 0.797, which differs from the benchmark value of 0.803, by 0.006. This difference is six times larger than the error calculated in Section 5.5.5. Since the  $\text{Eu}_2\text{O}_3$  is being added to the fuel elements of the inner ring in this case, it is expected that the RPPF value is smaller than the benchmark.

The difference between the intermediate and outer RPPF values in this case and the benchmark are 0.001. These differences are within the 0.001 error from Section 5.5.5. The amount of difference between MCNP and literature values is small. This indicated that no significant alteration of the RPPF profile of a fuel bundle by adding inner-optimized amount of  $\text{Eu}_2\text{O}_3$  to the inner elements.

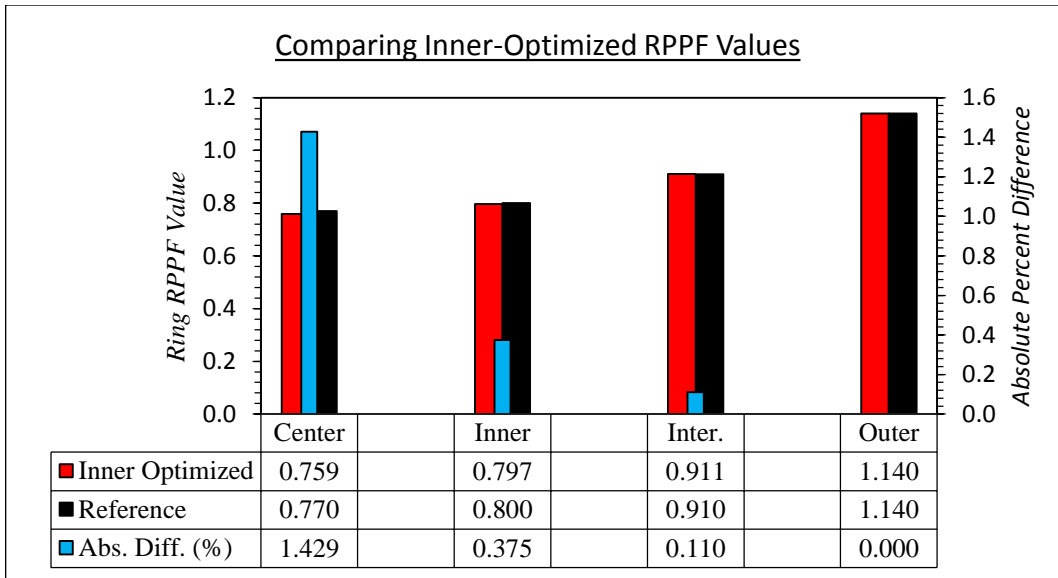


Figure 5.16: RPPF comparison between MCNP and literature values with an inner-optimized amount of  $\text{Eu}_2\text{O}_3$  added to the fuel elements of the inner ring

The next comparison will be for the intermediate-optimized results. These results are summarized in Figure 5.17. Similar to the other RPPF comparison graphs show thus far, the largest percent difference is observed in the center element. The RPPF value in the center element differs from the benchmark by 0.002. This difference is two times larger than the error associated with the RPPF results. Therefore, the addition of intermediate optimized amounts of  $\text{Eu}_2\text{O}_3$  into the fuel elements of the intermediate ring has an effect on the RPPF value of the center element.

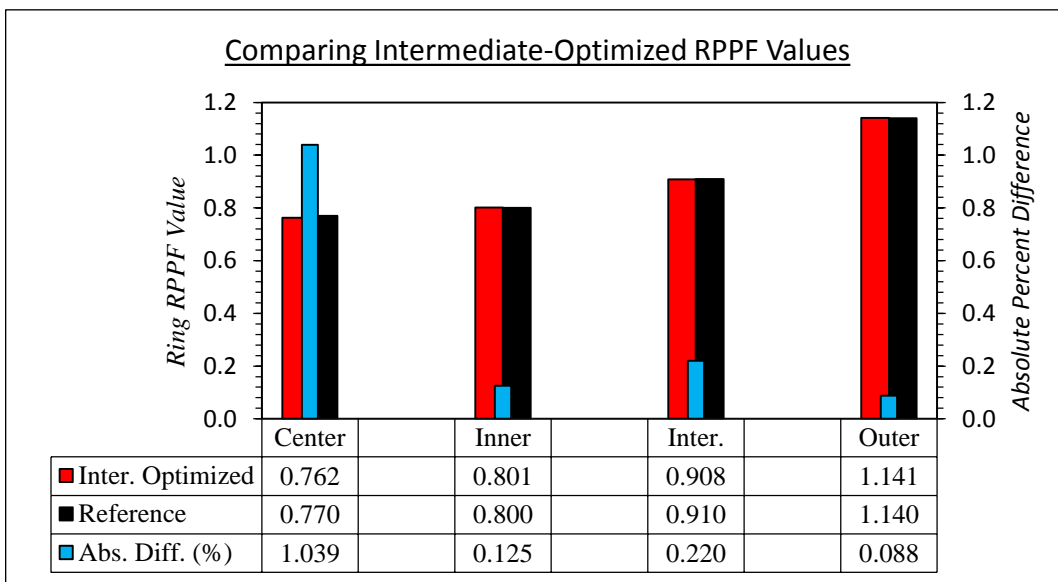


Figure 5.17: RPPF comparison between MCNP and literature values with an intermediate-optimized amount of  $\text{Eu}_2\text{O}_3$  added to the fuel elements of the intermediate ring

The RPPF value in the fuel elements of the inner ring has decreased to 0.801 from the benchmark value of 0.803. The difference between these two values is 0.002, which is two times the RPPF associated error. This indicates that adding intermediate optimized amounts of  $\text{Eu}_2\text{O}_3$  to the fuel elements in the intermediate ring has an effect on the RPPF value of the fuel elements in the inner ring.

The RPPF value in the fuel elements of the intermediate ring has decreased from the benchmark value of 0.911 to 0.908. The difference between these two results is 0.003, which is three times the RPPF associated error calculated in Section 5.5.5. The decrease in RPPF in the fuel elements of the intermediate ring is expected. Since these fuel elements have the  $\text{Eu}_2\text{O}_3$  doped fuel pellets.

Finally, the RPPF value for the fuel elements in the outer ring increase from a benchmark value of 1.138 to 1.141. The difference between these two values is 0.003, which is three times the calculated error associated with the RPPF values, indicating that having an intermediate-optimized amount of  $\text{Eu}_2\text{O}_3$  in the fuel elements of the intermediate ring has an effect of the RPPF of the fuel elements in the outer ring.

The conclusion remains the same for the intermediate-optimized case, as the two previous cases. The addition of an intermediate-optimized amount of  $\text{Eu}_2\text{O}_3$  to the intermediate elements, does not significantly alter the RPPF profile of the fuel bundle.

The final comparison is for the outer-optimized case. The comparison results are summarized in Figure 5.18. Similar to all other RPPF comparison graphs, the largest percent difference is observed in the center element. The RPPF value in the center element increases from the benchmark value of 0.764 to 0.765. The difference between these two values is 0.001, which is the calculated error associated with the RPPF values. Therefore, the addition of an outer-optimized amount of  $\text{Eu}_2\text{O}_3$  into the fuel elements of the outer ring, does not have a significant effect on the RPPF value of the center element.

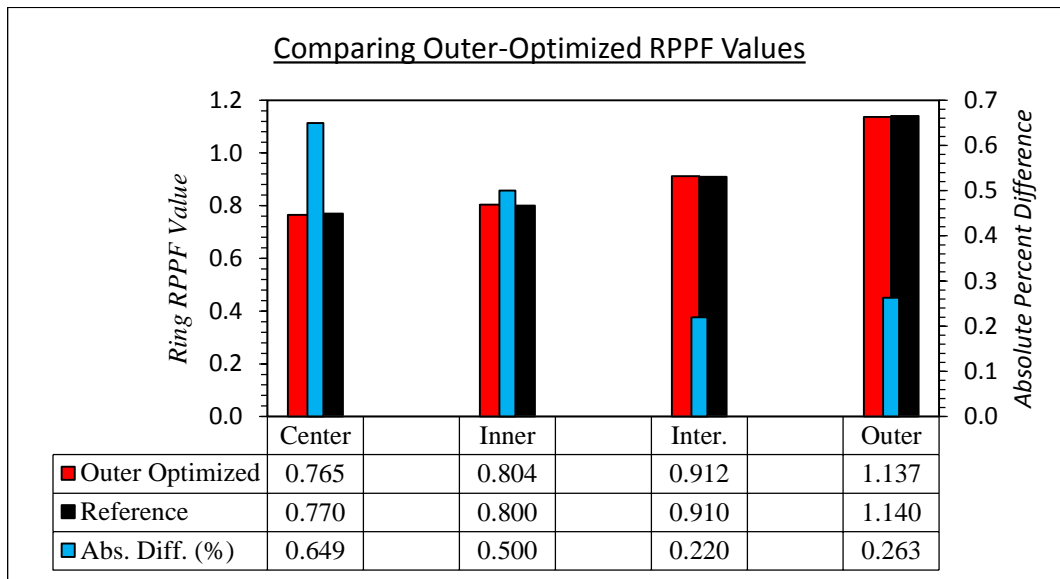


Figure 5.18: RPPF comparison between MCNP and literature values with an outer-optimized amount of  $\text{Eu}_2\text{O}_3$  added to the fuel elements of the outer ring

Next, the RPPF value for the fuel elements of the inner ring increase from a benchmark value of 0.803 to 0.804. The difference between these two values is 0.001, which is the calculated error associated

with the RPPF values. Therefore, the addition of an outer-optimized amount of  $\text{Eu}_2\text{O}_3$  into the fuel elements of the outer ring, does not have a significant effect on the RPPF value of the fuel elements in the inner ring.

The difference in the fuel elements of the intermediate ring follows the trend of this case. The difference between the RPPF value from this case and the benchmark differ by 0.001. Again, this difference is within the error associated with RPPF values calculated in Section 5.5.5. Therefore, the addition of an outer-optimized amount of  $\text{Eu}_2\text{O}_3$  into the fuel elements of the outer ring, does not have a significant effect on the RPPF value of the fuel elements in the intermediate ring.

Finally, the RPPF value for the fuel elements of the outer ring differs from the benchmark by 0.001. Therefore, the addition of an outer-optimized amount of  $\text{Eu}_2\text{O}_3$  into the fuel elements of the outer ring, does not have a significant effect on the RPPF value of the fuel elements in the outer ring.

As with all prior cases, the difference between MCNP and literature values is small. This indicated that no significant alteration of the RPPF profile of a fuel bundle by adding outer-optimized  $\text{Eu}_2\text{O}_3$  into the outer elements.

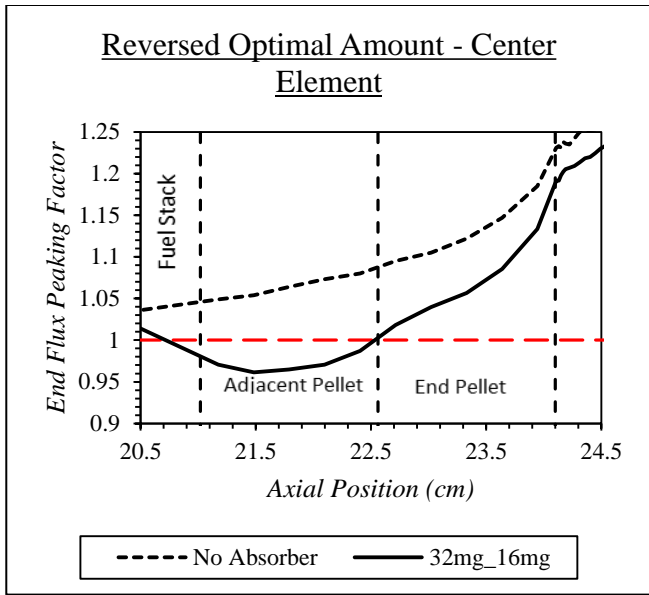
## 5.6 Swapping Adjacent and End Pellet Locations

In this section, the effect of switching the adjacent- and end-pellets in each of the ring-optimized cases from the previous section is demonstrated and discussed. For example, the center-optimized case from the previous section has 32 mg of  $\text{Eu}_2\text{O}_3$  into the end-pellet and 16 mg of  $\text{Eu}_2\text{O}_3$  into the adjacent pellet. The swapping of these two pellets places 16 mg  $\text{Eu}_2\text{O}_3$  into the end-pellet and 32 mg  $\text{Eu}_2\text{O}_3$  into the adjacent pellet.

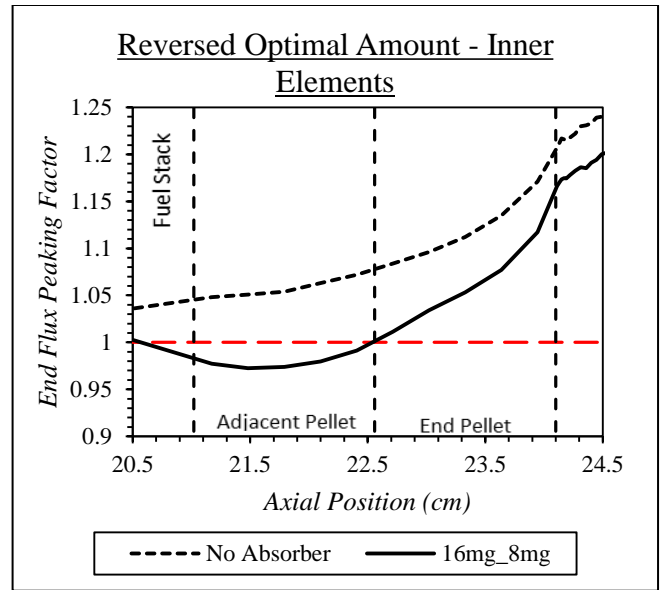
The focus of this investigation is to address concerns over misplacing doped fuel pellets in the fuel stack. As mentioned in previous sections, there already exist industry practices that would help to mitigate the risk of misplacing doped fuel pellets. The graph below shows the effect of swapping the placement of the adjacent and end pellets in the ring-optimized cases. A discussion will be provided for the potential of misplacing a doped fuel pellet elsewhere in the fuel stack. Note that the format of Figure 5.19 is the same as the format of Figure 5.14, which was presented in Table 5.3.

As shown in the above below, if the adjacent and end doped fuel pellets were swapped, the flux curve drops below the horizontal “Ideal” dashed line within the “Adjacent Pellet” region, while the flux curve in the “End Pellet” region observes mitigation, the degree of this mitigation being less than that observed in the ring-optimized cases. The reason for the flux curve drops below the “Ideal” line in the “Adjacent Pellet” region is that more  $\text{Eu}_2\text{O}_3$  is located in the adjacent pellet.

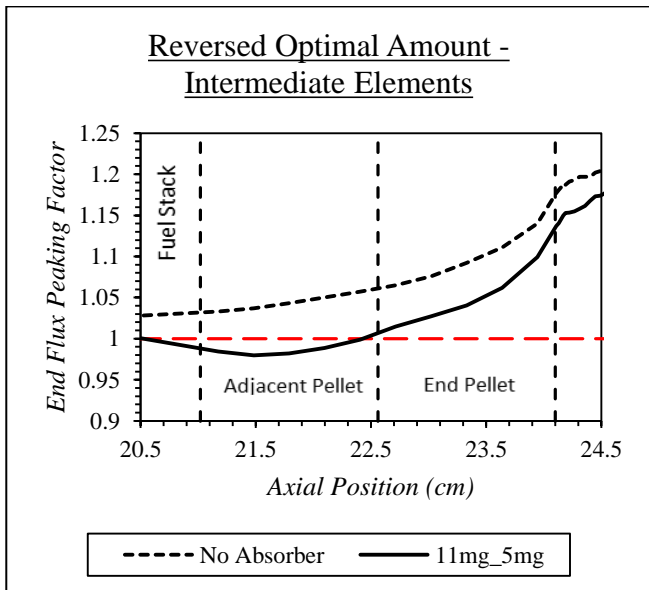
If a doped pellet were to be misplaced anywhere along the fuel stack, it is anticipated that the flux curve would drop below the horizontal “Ideal” dashed line, similar to the “Adjacent Pellet” regions in Figure 5.19. Therefore, adding a fuel pellet with a larger absorption cross section into any location in the fuel stack would cause the flux to decrease local to the doped pellet.



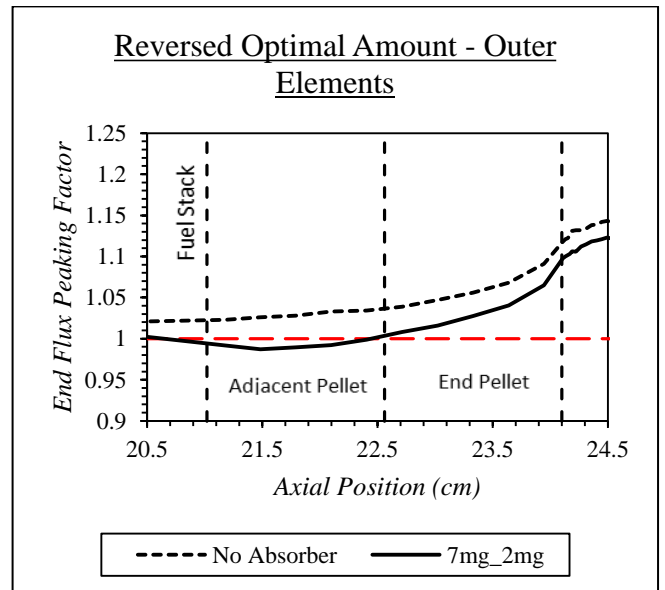
a)



b)



c)



d)

Figure 5.19: Effect of swapping the ring-optimized adjacent and end pellet locations on the EFP curve for fuel elements in each fuel ring

Physical differences in end pellet design should allow at least end pellets to be distinguishable from the other fuel pellets. Similar processes could be applied to the manufacturing of adjacent pellets as well, to allow adjacent pellets to be distinguishable from other fuel pellets. Manufactured physical

differences would help in mitigating the risk of doped fuel pellets being misplaced in the fuel stack during construction of a fuel element.

## 5.7 Effects of Doped Fuel Pellets on the Other Fuel Rings

### 5.7.1 Effect of Center-Optimized Fuel Bundle Configuration

The optimal amount of europium oxide for each ring of elements was determined in Section 5.5.5. In this section four sets of four graphs will be presented and discussed. Each set of graphs corresponds to one ring-optimized bundle configuration from Table 5.3. A similar table is also presented to reiterate each bundle configuration prior to the discussion.

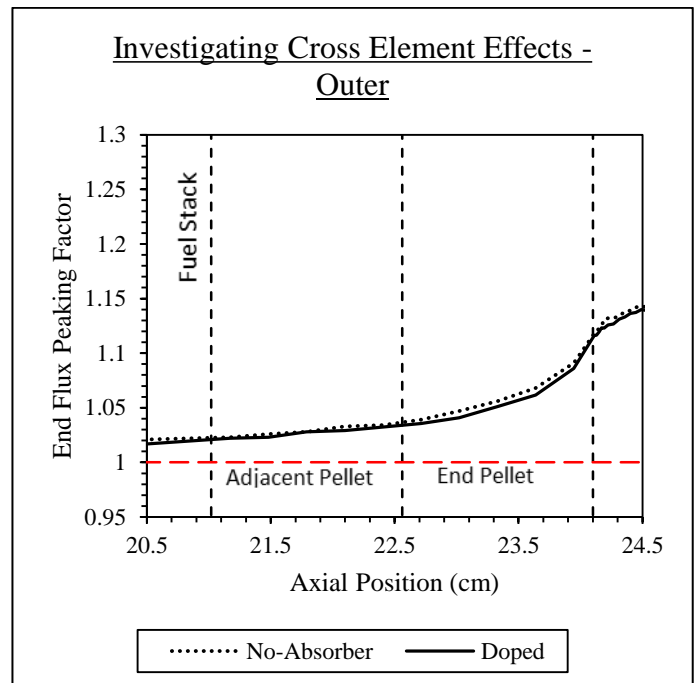
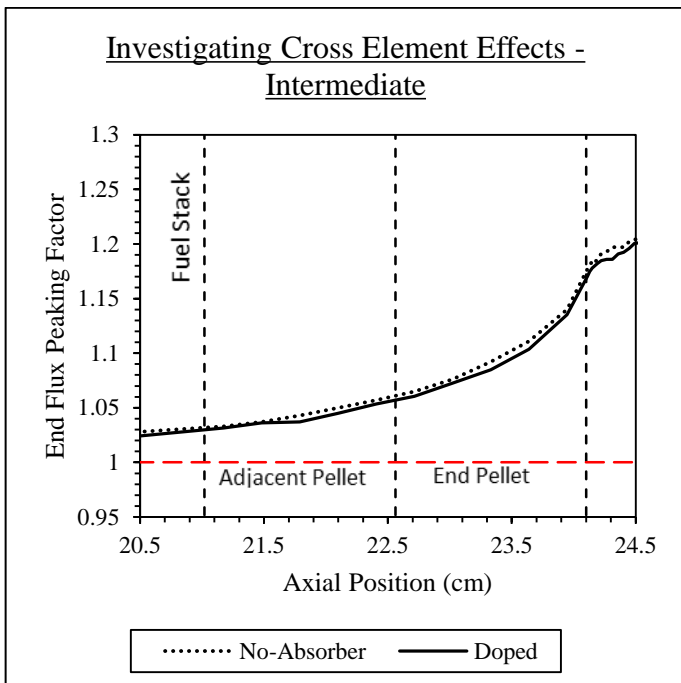
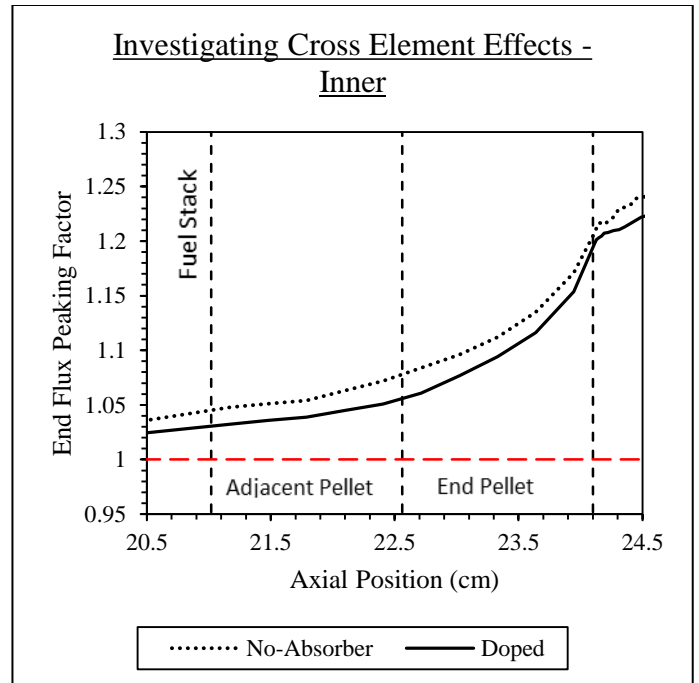
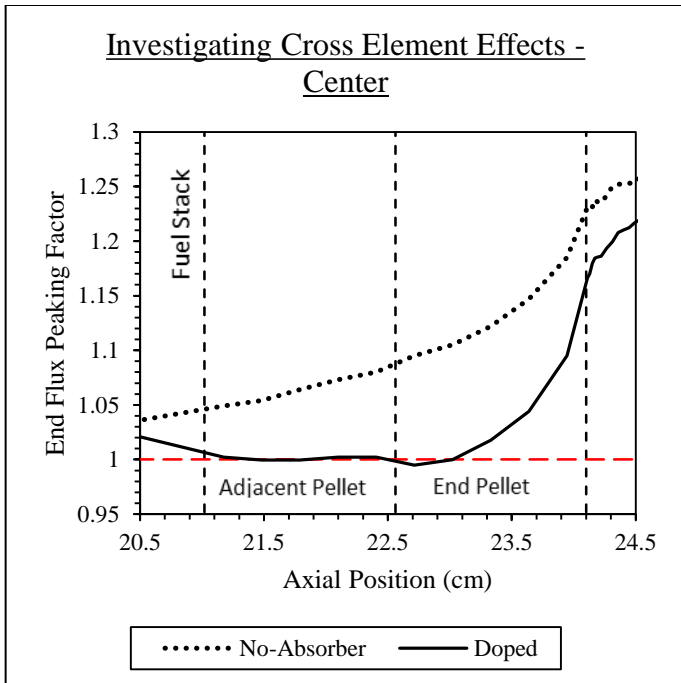
The first case is the center-optimized bundle, which is the center element doped with the center-optimized amount of  $\text{Eu}_2\text{O}_3$ . Table 5.4 summarises the amount of  $\text{Eu}_2\text{O}_3$  added to the fuel bundle and its location for the four graphs in the Figure 5.25.

Table 5.4: Description of  $\text{Eu}_2\text{O}_3$  location and amount for Figure 5.20

Figure Number	Ring Title			
	Center Element	Inner 6 Elements	Intermediate 12 Elements	Outer 18 Elements
5.20	16 mg $\text{Eu}_2\text{O}_3$ in Adjacent Pellet  32 mg $\text{Eu}_2\text{O}_3$ in End Pellet	No Absorber	No Absorber	No Absorber

Using Table 5.4, the  $\text{Eu}_2\text{O}_3$  is only added to the center element with the same amount found in the ring-optimized case. This means that no  $\text{Eu}_2\text{O}_3$  has been added to the other fuel rings. Therefore, any mitigation observed in the fuel rings other than the center element must be due to cross-ring effects. Note that the curve labels, “Doped” and “No Absorber” refer to the fuel bundle as a whole and not each fuel ring individually.

Figure 5.20a is identical to Figure 5.14a since both demonstrate the flux curve in the center element when the center-optimized amount of  $\text{Eu}_2\text{O}_3$  is added to the fuel bundle. Figure 5.20b, demonstrates the effect of the placing  $\text{Eu}_2\text{O}_3$  in the center element on the inner ring of six fuel elements. As demonstrated, there exists a small amount of mitigation in the fuel elements of the inner ring arising from the  $\text{Eu}_2\text{O}_3$  in the center element. Figure 5.20c and 5.20d further demonstrate that the mitigating effect provided by the  $\text{Eu}_2\text{O}_3$  in the center element on these fuel elements is barely distinguishable.



*Figure 5.20: Effects of adding ring-optimized amount of  $Eu_2O_3$  in the center element on the other three fuel rings*

## 5.7.2 Effect of Inner-Optimized Fuel Bundle Configuration

The next set of graphs demonstrates the effect of adding the inner-optimized amounts of  $\text{Eu}_2\text{O}_3$  in the inner ring on the other three fuel rings. The configuration is summarized in Table 5.5. The fuel bundle configuration in Figure 5.21 is the same as the fuel bundle configuration in Figure 5.14b.

Table 5.5: Description of  $\text{Eu}_2\text{O}_3$  location and amount for Figure 5.21

Figure Number	Ring Title			
	Center Element	Inner 6 Elements	Intermediate 12 Elements	Outer 18 Elements
5.21	No Absorber	8 mg $\text{Eu}_2\text{O}_3$ in Adjacent Pellet  16 mg $\text{Eu}_2\text{O}_3$ in End Pellet	No Absorber	No Absorber

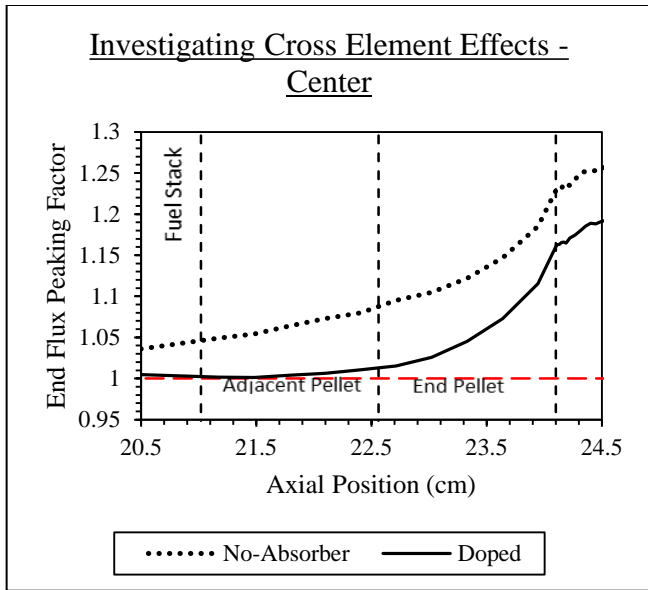
The following figure demonstrates the cross-ring effects from adding  $\text{Eu}_2\text{O}_3$  into the fuel elements of the inner ring on all other fuel rings.

Figure 5.21a demonstrates the cross-ring mitigation observed when  $\text{Eu}_2\text{O}_3$  is added to the inner elements only. As demonstrated, a significant amount of EFP mitigation is observed in the center element, even though no  $\text{Eu}_2\text{O}_3$  has been added there. Figure 5.21b is identical to Figure 5.14b, since both demonstrate the flux curve when the inner-optimized amount of  $\text{Eu}_2\text{O}_3$  is added into the fuel elements of the inner ring.

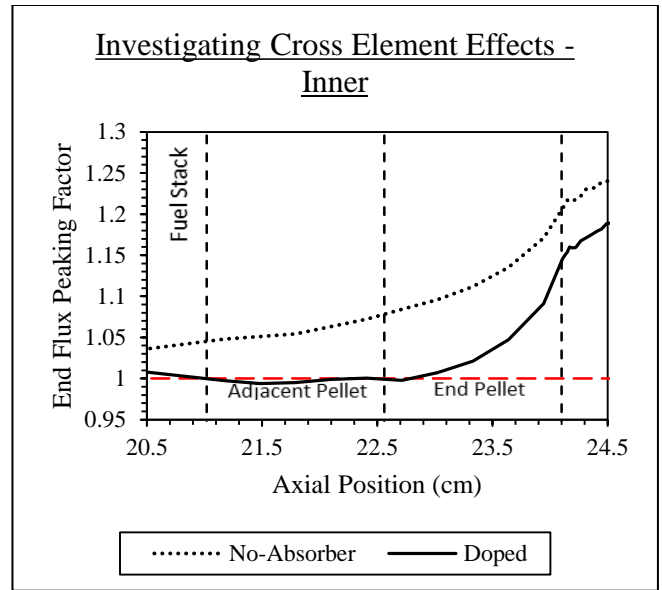
Figure 5.21c, depicts the cross-ring effect from the  $\text{Eu}_2\text{O}_3$  in the inner ring to the intermediate ring. While the degree of mitigation provided from the inner ring on the intermediate ring is less significant than on the center element, a non-negligible amount of mitigation is being provided to the intermediate ring.

Figure 5.21d demonstrates the cross-ring effect from the  $\text{Eu}_2\text{O}_3$  in the inner ring on the outer ring. Similar to the outer ring results from Figure 5.20, not much mitigation is provided to the outer ring from the inner ring. However, by comparing Figure 5.20d and 5.21d, the amount of mitigation does appear to increase in the outer ring now that the  $\text{Eu}_2\text{O}_3$  has been placed one fuel ring closer.

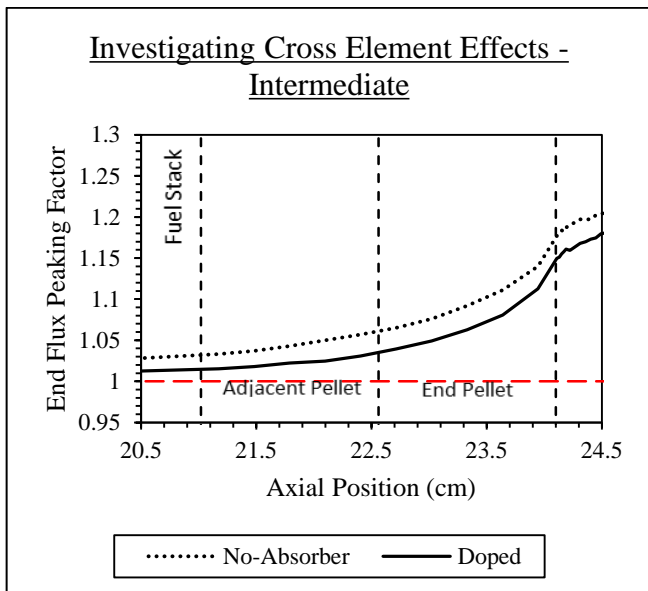




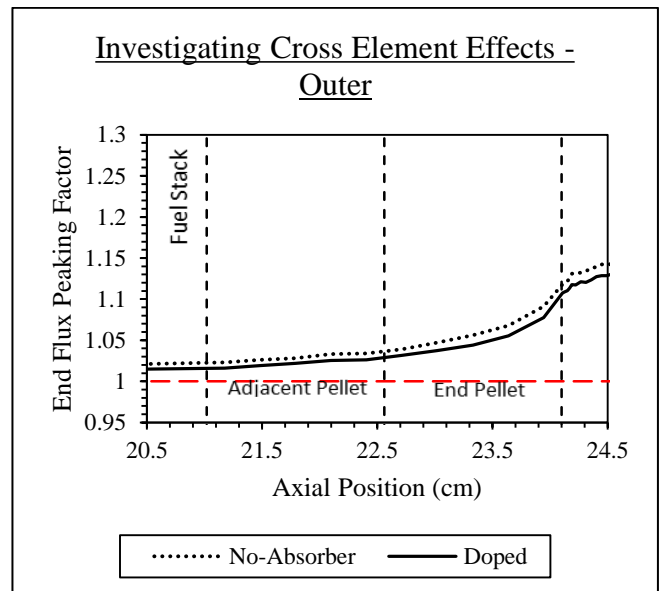
a)



b)



c)



d)

Figure 5.21: Effects of adding ring-optimized amount of  $\text{Eu}_2\text{O}_3$  in the inner element on the other three fuel rings

### 5.7.3 Effect of Intermediate-Optimized Fuel Bundle Configuration

The next set of graphs demonstrates the effect of adding intermediate-optimized amounts of  $\text{Eu}_2\text{O}_3$  into the fuel elements in the intermediate ring on the other three fuel rings. The configuration is summarized in Table 5.5.

Table 5.5: Description of  $\text{Eu}_2\text{O}_3$  location and amount for Figure 5.22

Figure Number	Ring Title			
	Center Element	Inner 6 Elements	Intermediate 12 Elements	Outer 18 Elements
5.22	No Absorber	No Absorber	5 mg $\text{Eu}_2\text{O}_3$ in Adjacent Pellet 11 mg $\text{Eu}_2\text{O}_3$ in End Pellet	No Absorber

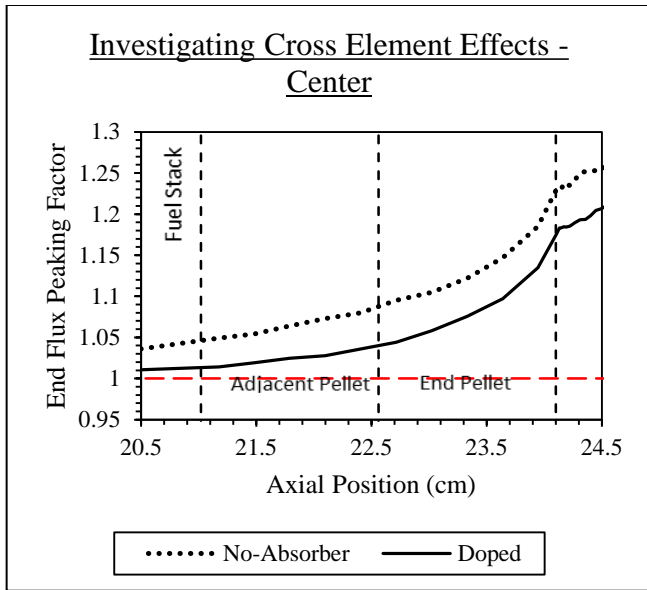
Figure 5.22 demonstrates the cross-ring effects from adding  $\text{Eu}_2\text{O}_3$  into the fuel elements of the intermediate ring on all other fuel rings. Note that the fuel bundle configuration in the following figure is the same as Figure 5.14c, as shown in Table 5.3.

Figure 5.22a demonstrates that adding  $\text{Eu}_2\text{O}_3$  into the fuel elements of the intermediate ring has a cross-ring effect on the center element. This cross-ring effect provides significant mitigation of the flux curve in the center element. However, when comparing Figure 5.21a with Figure 5.22a, the amount of mitigation provided by having the  $\text{Eu}_2\text{O}_3$  in the intermediate ring is less than having the  $\text{Eu}_2\text{O}_3$  in the inner ring. The reason for the decrease is that the intermediate ring is physically farther from the center element than the distance between inner ring and the center element.

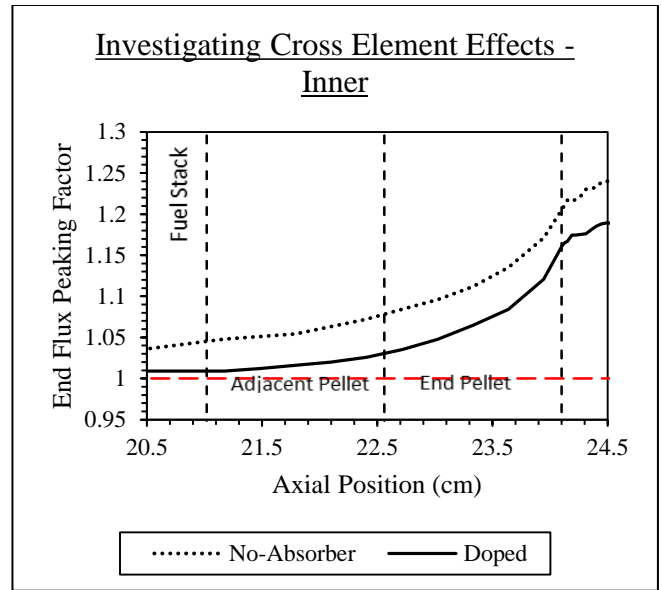
The next graph is Figure 5.22b, which demonstrates the cross-ring effect of adding  $\text{Eu}_2\text{O}_3$  to the fuel elements of the intermediate ring on the fuel elements of the inner ring. Significant mitigation is provided from the intermediate ring on the inner ring. The degree of mitigation exists somewhere between that demonstrated in Figure 5.20b and Figure 5.21b.

Figure 5.21c is identical to Figure 5.14c, since both cases contain the intermediate-optimized amount of  $\text{Eu}_2\text{O}_3$  added into the fuel elements of the intermediate ring.

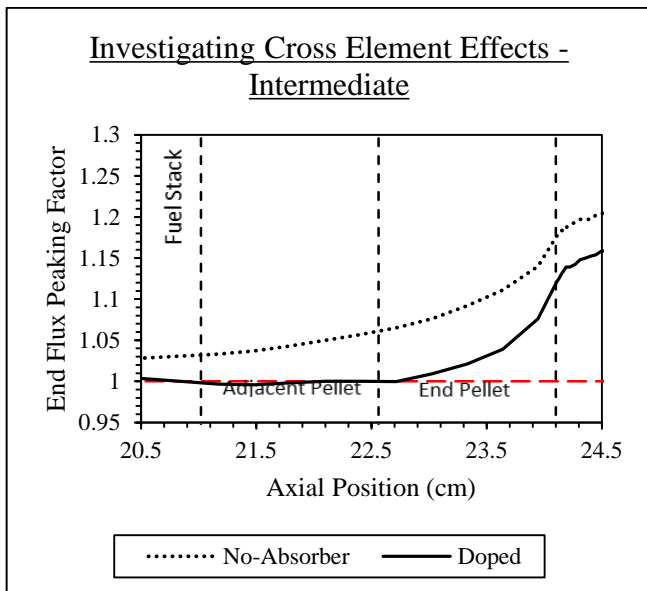
Figure 5.22d represents the cross-ring effect of effects of adding  $\text{Eu}_2\text{O}_3$  to the fuel elements in the intermediate ring on the fuel elements in the outer ring. Similar to the two previous cases, the mitigation effect on the fuel element in the outer ring is not as significant as on the other fuel rings. However, of the three cases discussed thus far, the mitigation provided by intermediate ring is the most significant. The intermediate ring is only one fuel ring away from the outer ring.



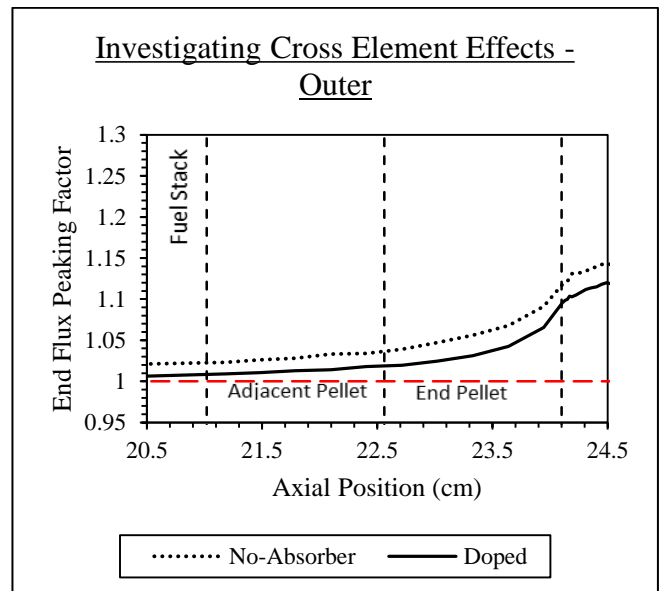
a)



b)



c)



d)

Figure 5.22: Effects of adding ring-optimized amount of  $\text{Eu}_2\text{O}_3$  in the intermediate element on the other three fuel rings

### 5.7.4 Effect of Outer-Optimized Fuel Bundle Configuration

The final set of graphs demonstrates the effect of adding outer-optimized amounts of  $\text{Eu}_2\text{O}_3$  into the fuel elements in the outer ring on the other three fuel rings. The configuration is summarized in Table 5.6.

Table 5.6: Description of  $\text{Eu}_2\text{O}_3$  location and amount for Figure 5.23

Figure Number	Ring Title			
	Center Element	Inner 6 Elements	Intermediate 12 Elements	Outer 18 Elements
5.23	No Absorber	No Absorber	No Absorber	2 mg $\text{Eu}_2\text{O}_3$ in Adjacent Pellet 7 mg $\text{Eu}_2\text{O}_3$ in End Pellet

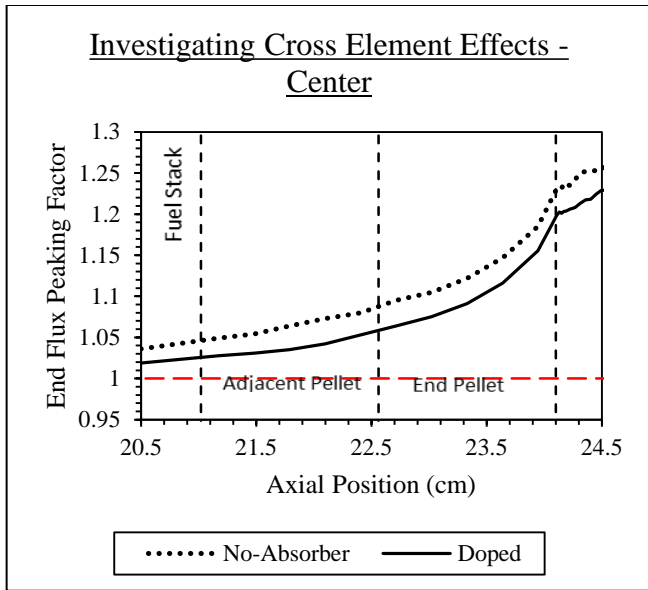
The following figure demonstrates the cross-ring effects from adding  $\text{Eu}_2\text{O}_3$  into the fuel elements of the outer ring on all other fuel rings.

Figure 5.23a shows that the addition of  $\text{Eu}_2\text{O}_3$  in the fuel elements in the outer ring provides some mitigation potential to the center element. The degree of the mitigation potential is less significant than the previous cases.

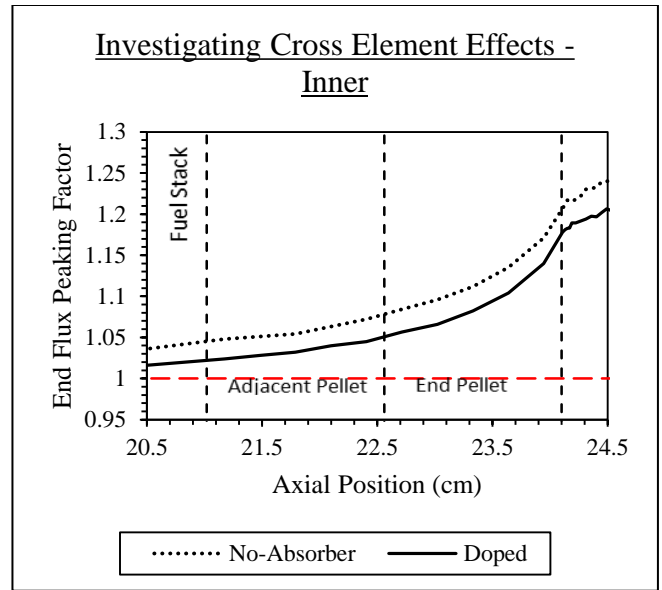
Figure 5.23b demonstrates the cross-ring effect of adding  $\text{Eu}_2\text{O}_3$  in the fuel elements of the outer ring on the fuel elements in the inner ring. Similar to the center element, significant mitigation is observed in the inner ring from the addition of  $\text{Eu}_2\text{O}_3$  to the outer ring. The degree of this mitigation is less than the inner and intermediate optimized cases but greater than the center-optimized case.

Figure 5.23c demonstrates the cross-ring effect of adding  $\text{Eu}_2\text{O}_3$  in the fuel elements in the outer ring on the fuel elements in the intermediate ring. Figure 5.23c demonstrates a level of mitigation similar to the inner ring case from Figure 5.21c. While this amount of mitigation is significant, it is less than the mitigation provided by the intermediate-optimized case shown in Figure 5.14c and 5.22c.

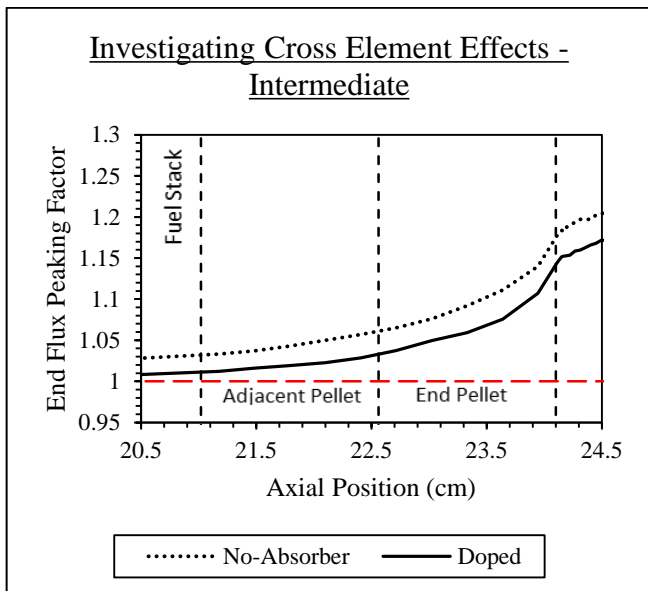
Figure 5.23d is identical to Figure 5.14d, since both cases contain the outer-optimized amount of  $\text{Eu}_2\text{O}_3$  added into the fuel elements of the outer ring.



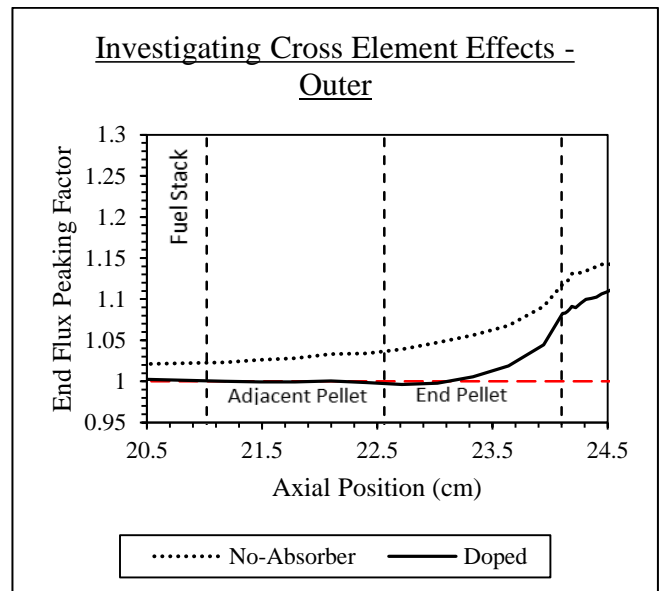
a)



b)



c)



d)

Figure 5.23: Effects of adding ring-optimized amount of  $\text{Eu}_2\text{O}_3$  in the outer element on the other three fuel rings

### 5.7.5 Effect of Using All Ring-Optimized Results

The conclusion of this section is that significant cross-ring mitigation is observed for each of the ring-optimized cases. Therefore, a fuel bundle incorporating each of the ring-optimized amounts of  $\text{Eu}_2\text{O}_3$

in all fuel elements would lead to over mitigation. Figure 5.24 demonstrates the effect of adding all the ring-optimized amounts of  $\text{Eu}_2\text{O}_3$  to a single fuel bundle.

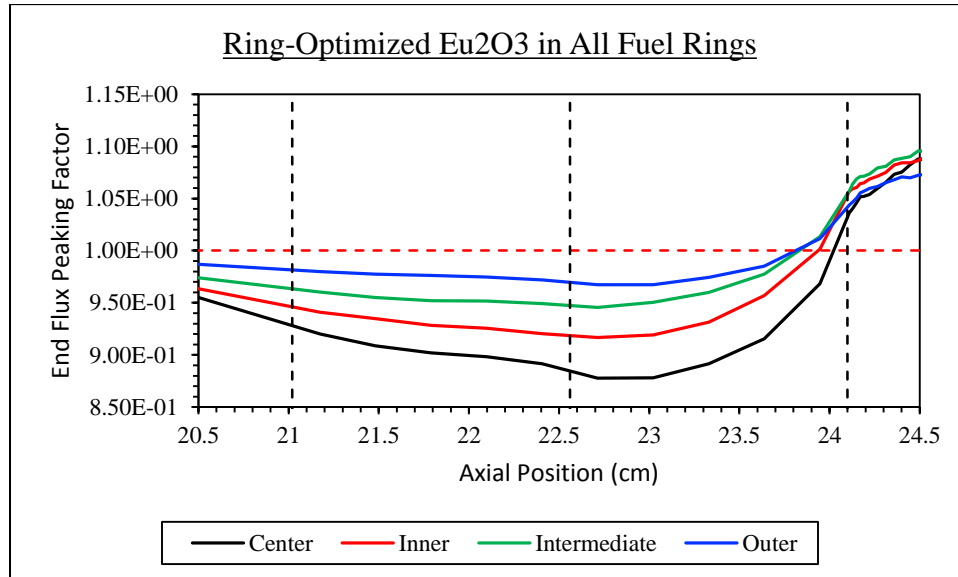


Figure 5.24: Effect of adding ring-optimized  $\text{Eu}_2\text{O}_3$  added to each of the fuel rings simultaneously

All the flux curves in Figure 5.24 drop below the “Ideal” line as with the preliminary cases involving gadolinium. Thus, the results presented in Section 5.5.5, while providing the optimal solution for each fuel ring individually, it does not provide an ideal bundle-wide mitigation solution.

## 5.8 Bundle-Optimized Results

As demonstrated in the previous section significant cross-ring mitigation occurs when  $\text{Eu}_2\text{O}_3$  is added to the fuel pellets. This prevents using all ring-optimized results simultaneously in a fuel bundle. Since the cross-ring mitigation would lead to a case of over-mitigation within the end-region of all fuel elements. Therefore, a configuration must be found which is optimized over all fuel rings simultaneously.

While optimizing over all fuel rings is possible, it is time consuming and not the most practical solution to the problem. As mentioned using two separate end-pellets for each fuel ring leads to many fuel pellets of varying composition. Having many fuel pellets with various  $\text{Eu}_2\text{O}_3$  concentrations is not an ideal solution as there is a potential that they are misplaced with the fuel stack or within the fuel bundle. However, the two end-pellet configurations still present the most effective method of mitigating EFP without altering structural components.

As mentioned in Section 5.5.5, having eight types of doped fuel pellets with varying concentrations of  $\text{Eu}_2\text{O}_3$  presents a complex but effective method for mitigating EFP. Having so many different doped pellets also brings the risk of misplacing the doped pellets in the fuel stack. Therefore, a bundle-optimized solution should strive to limit the number of doped pellets. Ideally, there would only be a single concentration of  $\text{Eu}_2\text{O}_3$  added to all the doped pellets in all fuel elements. Since EFP differs

depending on the fuel ring a fuel element resides, having a single concentration of  $\text{Eu}_2\text{O}_3$  would be effective in particular fuel rings and rather ineffective in others.

Unfortunately, creating a simple mitigation solution using end-pellets to a phenomenon like EFP does not seem possible. Results from the previous section, demonstrating cross-ring effects, show that by adding  $\text{Eu}_2\text{O}_3$  into the fuel elements of certain fuel rings leads to mitigation across all fuel elements. In particular, adding the outer-optimized amount of  $\text{Eu}_2\text{O}_3$  to the outer elements causes significant EFP mitigation across all fuel rings. The amount of mitigation in the fuel rings aside from the outer ring is significant but not as significant as the other ring-optimized cases. The outer-optimized amount places a limit on the amount of  $\text{Eu}_2\text{O}_3$  that can be placed into the outer elements. Since any more  $\text{Eu}_2\text{O}_3$  in the outer elements would lead to the flux curve dropping below the “Ideal” line.

To increase the EFP mitigation in all other fuel rings, the addition of a second ring of doped fuel elements must be added. The proposed second fuel ring in which  $\text{Eu}_2\text{O}_3$  will be placed into the fuel elements will be the inner ring. The inner-optimized amount of  $\text{Eu}_2\text{O}_3$  was able to provide significant mitigation to the center element, while providing decent mitigation to the intermediate and little to the outer ring. Therefore, the proposed bundle-optimized locations of the doped fuel pellets will be in the inner and outer fuel rings only. The goal is to find the amount of  $\text{Eu}_2\text{O}_3$  needed in these two fuel rings to provide significant mitigation across all fuel rings.

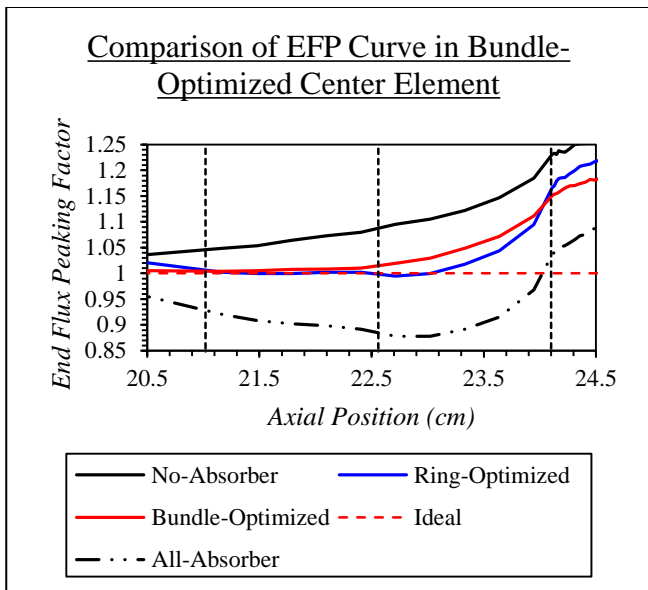
Since there is some cross-ring effect experience from the outer ring on the inner ring and vice-versa, the amount of  $\text{Eu}_2\text{O}_3$  added to both ring may differ from the ring-optimized case. However, the ring-optimized amounts provide a starting point to be used in the optimization procedure outlined in Section 5.5.5. Once following the optimization procedure used for the ring-optimized results, the following bundle-optimized amounts of  $\text{Eu}_2\text{O}_3$  added to the inner and outer rings in the two-pellet configuration was determined.

*Table 5.7: Bundle-Optimized amount of  $\text{Eu}_2\text{O}_3$  in the inner and outer fuel elements*

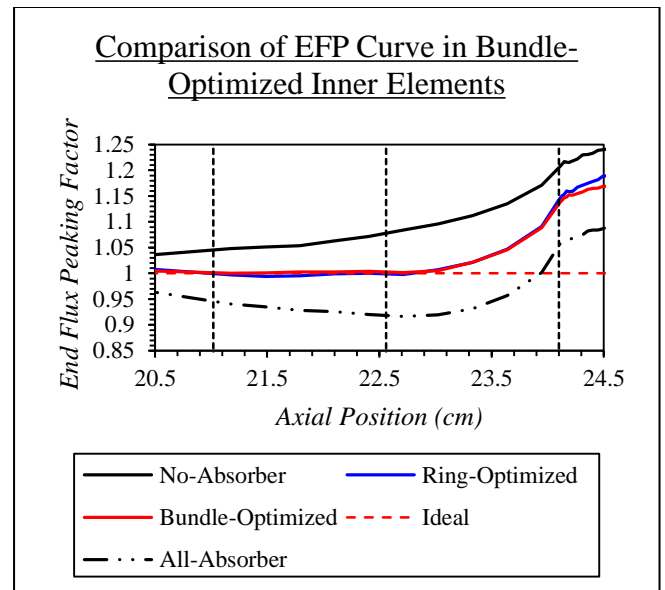
<b>Fuel Ring</b>	<b><math>\text{Eu}_2\text{O}_3</math> in Adjacent Pellet (mg)</b>	<b><math>\text{Eu}_2\text{O}_3</math> in End Pellet (mg)</b>
<i>Inner (6 elements)</i>	4	12
<i>Outer (18 elements)</i>	2	6

Note that the value found using the optimization routine across all fuel rings are close to the amounts in the ring-optimized case. This is especially true for the outer elements where there is only a 1 mg difference in the amount of  $\text{Eu}_2\text{O}_3$  added to the end pellet. The amount of  $\text{Eu}_2\text{O}_3$  added to both the adjacent and end pellet for each element in the inner ring is 4 mg less than the ring-optimized case. This is expected since the elements in the outer ring are providing mitigation to the inner elements as well.

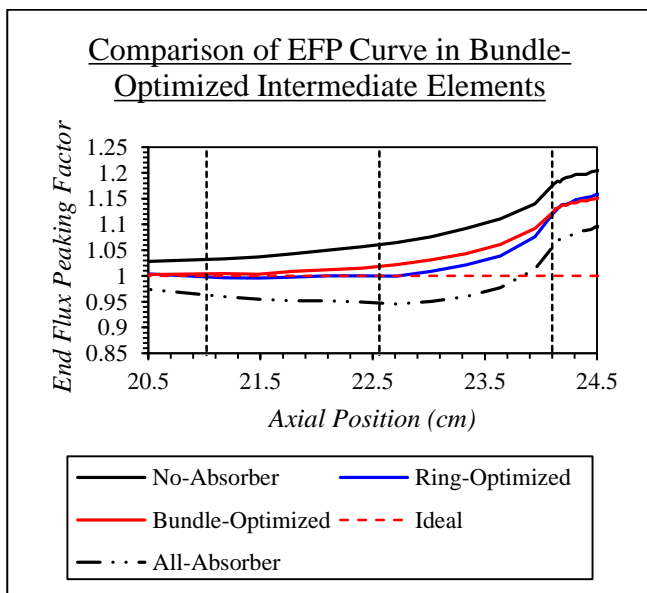
The results for all fuel rings are summarized in Figure 5.25. Note that included in each of the graphs in Figure 5.25 are the flux curves for the ring-optimized case, the no-absorber case, as well as the all-absorber case for comparison. Little difference is observed when comparing the bundle- and ring-optimized results in the inner and outer ring. This is due to the fact that these were the fuel rings where the  $\text{Eu}_2\text{O}_3$  was added in the bundle-optimization procedure. When comparing the bundle- and ring-optimized cases for the center element and intermediate ring there is a slight difference in the flux curves. In both the center and intermediate fuel rings the bundle-optimized curve existed between the ring-optimized and benchmark curve. This means that the bundle-optimized results provide slightly less mitigation to the center element and the elements in the intermediate ring.



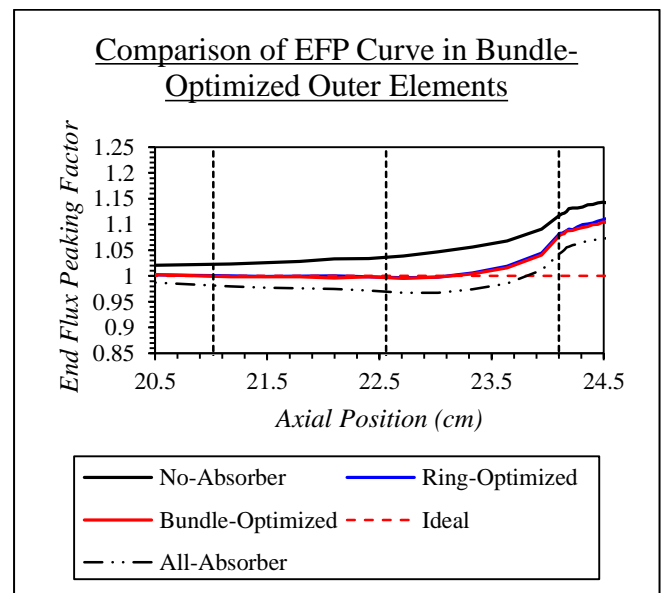
a)



b)



c)



d)

Figure 5.25: Comparison of bundle-optimized solution to all previous cases

The ability of the bundle-optimized results in mitigating EFP is approximately the same as the ring-optimized results. The bundle-optimized curves exist well above the all-absorber case and well below the no-absorber case. While straddling the “Ideal” line closely indicating that the bundle-optimized results perform better than adding all ring-optimized results into a single fuel bundle, as shown in Figure 5.25. While providing significant EFP mitigation potential when compared to adding no  $\text{Eu}_2\text{O}_3$  to the fuel bundle, the conclusion for the bundle-optimized cases tends to mitigate EFP with as much potential as the ring-optimized results.



# Chapter 6: Conclusion

EFP is a phenomenon where a region of elevated neutron flux occurs at the end regions between two adjoining fuel bundles in CANDU reactors. These peaks of high neutron flux lead to an increase in fission rate and therefore greater heat generation in the end regions. This increase in heat generation is of particular concern during refuelling and loss-of-coolant accident conditions.

A three-dimensional CANDU fuel bundle model using MCNP 6.1 was developed to accurately simulate EFP, as well as investigate possible EFP mitigation strategies. The model improves upon results from two-dimensional models in literature by being fully three dimensional while maintaining the ability to predict accurate EFP results. Many scripts such as, MATLAB, Python, general MCNP Input deck and BATCH, allows for users to easily alter the location of the absorber by altering string placeholders. The scripts created also allow users to automate the simulation. The overall package of scripts provides a tool for future graduate students to investigate the impact of EFP on future fuel bundle design changes that are of interest at RMCC.

These mitigation strategies involved the addition of a small amount of neutron absorbing material strategically within a CANDU fuel bundle. In this work, thin disks, CANLUB, endplates and end pellets were investigated as locations in which BNAs could be added. It was determined that the best location to introduce BNA to mitigate EFP was with the last two end pellets at either end of the fuel stack. As the introduction of BNA in these two fuel pellets directly addresses the increase in thermal neutron flux observed in these fuel pellets. Even though endplate alloyed with absorbing material could provide the best mitigation potential, there exist several concerns with this method of implementing absorbers into the fuel bundle. The other two locations demonstrated undesirable behaviour. The BNA in the CANLUB led to a more pronounced EFP phenomenon and the BNA was not isolated in the end region of the fuel elements. Finally, the thin disks caused a significant drop in the thermal neutron flux below the midplane flux value localized to where the thin disks were added

The BNA chosen to best mitigate EFP was  $\text{Eu}_2\text{O}_3$ , since it provides the perfect balance between high thermal neutron absorption cross section and longevity during reactor operation. Both ring-optimized and bundle-optimized solutions for mitigating EFP were determined using the two-end-pellet configuration. This change would have an impact on fuel manufacturing, but the benefits to both EFP and other phenomena are worth further investigation.

Two important conclusions were derived from this work. The first conclusion is that the addition of neutron absorbers affects the flux profile even in small quantities. The second conclusion is that, based on certain criteria the optimal location and amount of absorber can be determined through the use of various optimization techniques.

The design study of strategically introducing burnable neutron absorbers into the fuel bundle is an on-going project at RMCC, as a project funded by COG and NSERC.

# Chapter 7: Recommendations

Continuation of this project should include simulating the conditions during various stages of refuelling. To simulate various stages of refuelling, a variety of MCNP input decks need to be created. Some of these input decks could include contact with the stainless-steel pusher of the refuelling machine, as well as having the end region in contact with the D<sub>2</sub>O coolant only. Further continuation of this project would emphasize investigating EFP at different stages of fuel burnup. A possible method of accounting for fuel burnup is to create various input decks, where the fuel material card reflects the isotopic composition of CANDU fuel at various burnup values. Another extension of this project is to investigate the effects of EFP in a finite core. Instead of modelling a full core, finite effects can be approximated by modelling an extra eight radial fuel channels. Another possible extension would be to investigate EFP during a large-break loss-of-coolant accident (LBLOCA), with various coolant densities.

# References

- [1] French, P. M., *Measurements of Bundle End Flux Peaking Effects in 37-element CANDU PHW Fuel*. Chalk River Nuclear Laboratories, October 1997.
- [2] Morgan, D., *A Thermochemical Model of CANDU Fuel.*, Royal Military College of Canada. May 2007.
- [3] Balaceanu, V. and Hristea, V., *Study of the End Flux Peaking for the CANDU Fuel Bundle Types by Transport Methods*. Institute for Nuclear Research, Nuclear Energy for New Europe 2005, September 2005.
- [4] Chan, P. K., Paquette, S., and Bonin, H. W., *Variation of Burnable Neutron Absorbers in Heavy Water Moderated Fuel Lattice: A Potential for Improved CANDU Reactor Operating Margins*. Nuclear Technology. 1.191.2015.
- [5] Lamarsch, J. R., and Baratta A. J., *Introduction to Nuclear Engineering Third Edition*. Prentice Hall. 2012.
- [6] Bennet, L. G. I., Lewis, B. J., Bonin, H. W. and Corcoran, E. C., *PHYS 491: Physics of Nuclear Reactors.*, Royal Military College of Canada/ Queen's University. September 2013.
- [7] Bonin, H. W., "Canadian Nuclear Engineering Volume 1: Physics of the Nuclear Reactor". Royal Military College of Canada. Kingston, ON. 2014. (Documentation #RMC-CCE-HWB-11-2)
- [8] Lewis, B. J., and Bonin, H. W., "CC501 Course Notes: Chemical and Nuclear Engineering Computations Part 1". Royal Military College of Canada. 2014.
- [9] Lewis, B. J., and Bonin, H. W., "CC501 Course Notes: Chemical and Nuclear Engineering Computations Part 2". Royal Military College of Canada. 2014.
- [10] Lamarsh, J. R., "Nuclear Reactor Theory". Addison-Welsey Series in Nuclear Engineering. September, 1972.
- [11] Rouben, B., "*CANDU Fuel-Management Course*". CANTEACH Publication Library, 1999. Retrieved from <http://canteach.candu.org/SearchCenter/Pages/CLibraryResults.aspx>
- [12] Kaplan, I., "Nuclear Physics: Second Edition". Addison-Welsey Series in Nuclear Science and Engineering. March, 1984.
- [13] Bell, G. I., and Glasstone, S., "Nuclear Reactor Theory". Robert E. Krieger Publishing Company. 1970.
- [14] Tayal, M., and Gacesa, M., "Chapter 17: Fuel". In: *The Essential CANDU: A Textbook on the CANDU Nuclear Power Plant Technology*". September 2014.

- [15] Chaplin, R., “Chapter 2: Genealogy of CANDU Reactors”. In: *The Essential CANDU: A Textbook on the CANDU Nuclear Power Plant Technology*. September 2014.
- [16] Chaplin, R., “Chapter 8: Nuclear Plant Systems”. In: *The Essential CANDU: A Textbook on the CANDU Nuclear Power Plant Technology*. September 2014.
- [17] Chaplin, R., “Chapter 1: Introduction to Nuclear Reactors”. In: *The Essential CANDU: A Textbook on the CANDU Nuclear Power Plant Technology*. September 2014.
- [18] Garland, W. J., “Prologue: CANDU in Context”. In: “*The Essential CANDU: A Textbook on the CANDU Nuclear Power Plant Technology*”. Department of Engineering Physics, McMaster University. Hamilton, Ontario, Canada. September 2014.
- [19] Lewis, B. J., “CC533 Nuclear Fuel Engineering Course Notes”. Royal Military College of Canada. Kingston, Ontario. 2014.
- [20] Chan, P. K., “CC533 Nuclear Fuel Engineering Course Notes”. Royal Military College of Canada. Kingston, Ontario. 2014.
- [21] Olander, D. R., “Fundamental Aspects of Nuclear Reactor Fuel Elements”. Division of Reactor Development and Demonstration, Energy Research and Development Administration. 1976.
- [22] Technical Training Group. “Science and reactor Fundamentals – Reactor Physics”. Canadian Nuclear Safety Commission. Ottawa, Ontario. January, 2003.
- [23] Tayal, M., and Gacesa, M., “Chapter 18: Fuel Cycles”. In: *The Essential CANDU: A Textbook on the CANDU Nuclear Power Plant Technology*. September 2014.
- [24] Klezeck, M. R., “*Thermodynamic and Kinetic Modelling of Iodine Induced Stress Corrosion Cracking in Nuclear Fuel Sheathing Master’s Thesis*”. Royal Military College of Canada. April 2010.
- [25] Aziz, M., Shaker, M. O., Aboanber, A., Massoud, E. and Slama, M. *Improved Formula for Prompt Fission Neutron Spectrum*. National Center for Nuclear Safety and Radiation Control. July 21, 2009.
- [26] Meneley, D. A., and Ruan, Y. Q. Introduction to CANDU 6 – Part 1. Course presented at Xi’an Jiatong University. September 22 – 25, 1998.
- [27] Page, R. D., “Canadian Power Reactor Fuel”. Atomic Energy of Canada Limited Power Projects. Sheridan Park Research Community. Mississauga, Ontario. March 1976.
- [28] Paquette, S., Chan, P. K., Bonin, H. W., and French, C., “Variation of Burnable Neutron Absorbers in a Heavy Water-Moderated Fuel Lattice: A Potential to Improve CANDU Reactor Operating Margins”. *Nuclear Technology* Vol. 191. July 24, 2014.

- [29] Chan, P. K., Paquette, S., Cuning, T. A., French, C., Bonin, H. W., Pandey, M., and Murchie, M., "Margin Improvement Initiatives: Realistic Approaches". The 19<sup>th</sup> Pacific Basin Nuclear Conference (PNBC 2014). Vancouver, British Columbia, Canada. August 24-28, 2014.
- [30] Chan, P. K., Song, J. J., Paquette, S., and Bonin, H. W., "*Fuel Study of a CANDU Reactor Using Fuels Containing Burnable Neutron Absorbers*". Nuclear Technology 193(3).310.2016
- [31] Shen, W. "*Validation of DRAGON End Flux peaking and Analysis of End Power Peaking factors for 37-Element CANFLEX and Next Generation CANDU Fuels*". Proc. Of the 22<sup>nd</sup> CNS Annual Conference. Toronto, June 10-13,2001
- [32] Atfield J. E. and Zeller, M. B., "End-Flux Peaking Experiment in the ZED-2 Reactor using CANFLEX-RU". AECL Chalk River Laboratories. Chalk River. 32<sup>nd</sup> Annual Conference of the Canadian Nuclear Society. June 5-8, 2011.
- [33] Roshd, M. H. M., "Flux Peaking and Suppression in CANDU-BLW Fuel Bundles". Atomic Energy of Canada Limited. May 1968.
- [34] Xu, Z., Jiang, Q., Lai, L., and Shams, M., "Analysis of Fuel End-Temperature Peaking". 12<sup>th</sup> International Conference on CANDU Fuel. Kingston, Ontario. September 15-18, 2013.
- [35] Brenciaglia, G., "Lecture 3: Lattice Parameter Calculations". Department of Nuclear Technology, Chulalongkorn University. July, 1997.
- [35] Horhoianu , G., Moscalu, D. R., Olteanu, G., Ionesco, D.V. "*Development of SEU-43 Bundle for CANDU Type Reactors*". Pergamon. 1998.
- [36] Case K. M., de Hoffmann, F., Placzek, G., "*Introduction to the Theory of Neutron Diffusion Volume 1*". Los Alamos Scientific Laboratory. June 1953.
- [37] Landu, D. P., and Binder K., "A Guide to Monte Carlo Simulations in Statistical Physics: Third Edition". Cambridge University Press.
- [38] Ho. S., "Presentation for Astro 542: Introduction to Monte Carlo". Princeton University.
- [39] Atzberger, P. J., "The Monte-Carlo Method". New York University.
- [40] Moler, C., "Numerical Computing with MATLAB, Electronic Edition". The MathWorks, Inc., Natick, MA. 2004.
- [41] Park, S. K., and Miller, K. W., "Random Number Generators: Good ones are hard to find". Comm. ACM Vol. 32. 1988.
- [42] Lecuyer, P., "Random Number Generation". In: Haerdle, J. E., and Mori, W. Y., "Handbook of Computational Statistics". Springer. Verlag, Berlin, Chapter II.2. 2004.
- [43] Sadus, R. J., "Presentation: Introduction to Monte Carlo Methods". Centre for Molecular Simulation, Swinburne University of Technology. Hawthorn Victoria, Australia.

- [44] Katzgraber, H. G., “Introduction to Monte Carlo Methods”. Department of Physics and Astronomy, Texas A&M University, College Station, Texas, USA. May 4, 2011.
- [45] Mackay, D. J. C., “Introduction to Monte Carlo Methods”. Department of Physics, Cambridge University, Cavendish Laboratory. Cambridge, United Kingdom.
- [46] Whitlock K. *Monte Carlo Methods Volume 1: Basics*. John Wiley and Sons.1986.
- [47] Cashwell, E., Neergaard, J., Taylor, W., and Turner, G., “*MCNP: A Neutron Monte Carlo Code*”. Los Alamos Scientific Laboratory of the University of California., LA-4751, January 1972.
- [48] Brown, F. B., Martin, W. R., *High Performance Computing and Monte Carlo*. Diagnostics Applications Group (X-5), Los Alamos National Laboratory., LA-UR-04-4532.
- [49] Cashwell, E., Neergaard, J., Taylor, W., and Turner, G., *MCN: A Neutron Monte Carlo Code*. Los Alamos Scientific Laboratory of the University of California., LA-4751, January 1972.
- [50] Anderson, H.L., *Metropolis, Monte Carlo and MANIAC*. Los Alamos Science. 1986.
- [51] X-5 Monte Carlo Team, “MCNP – A General Monte Carlo N-Particle Transport Code, Version 5 Volume 1: Overview and Theory” Los Alamos National Laboratory. April 24, 2003.
- [52] X-5 Monte Carlo Team, “MCNP – A General Monte Carlo N-Particle Transport Code, Version 5 Volume 2: User’s Guide” Los Alamos National Laboratory. April 24, 2003.
- [53] X-5 Monte Carlo Team, “Introduction to MCNP5 and MCNPX: Presentation”. Los Alamos National Laboratory. 2003.
- [54] Miller S. J., “*The Method of Least Squares*”. Mathematics Department, Brown’s University. Providence. 2012.
- [55] Page R. D., and Lane, A. D., “The Performance of Zirconium Alloy Clad UO<sub>2</sub> Fuel for Canadian Pressurized and Boiling Water Power Reactors”. Joint ANS-CNA Conference. Toronto, Ontario. June 10-12 1968.
- [56] Chang, T. L. and Tung L. H., “The Density of Heavy Water between 25° and 100°C”. Department of Chemistry, National Tsing Hua University. Peiping. November 30, 1948.
- [57] ATI Wah Chang Allegheny Technologies. “Reactor Grade Zirconium Alloys for Nuclear Waste Disposal Technical Data Sheet”. Albany, Oregon.

# Appendices

## Appendix A.1: Surfaces Defined by Equations

To specify a surface, first find the surface mnemonic and input the coefficients needed for the equation depending on the problem geometry. The following table shows some examples of simple geometry definitions in MCNP,

Table A.1.1: Geometry definitions in MCNP

Mnemonic	Type	Description	Equation	Card Entries
<i>P</i>	Plane	General	$Ax + By + Cz - D = 0$	<i>ABCD</i>
<i>PX</i>		Normal to X-axis	$x - D = 0$	<i>D</i>
<i>PY</i>		Normal to Y-axis	$y - D = 0$	<i>D</i>
<i>PZ</i>		Normal to Z-axis	$z - D = 0$	<i>D</i>
<i>SO</i>	Sphere	Centered at Origin	$x^2 + y^2 + z^2 - R^2 = 0$	<i>R</i>
<i>S</i>		General	$(x - \bar{x})^2 + (y - \bar{y})^2 + (z - \bar{z})^2 - R^2 = 0$	$\bar{x} \bar{y} \bar{z} R$
<i>SX</i>		Centered on X-axis	$(x - \bar{x})^2 + y^2 + z^2 - R^2 = 0$	$\bar{x} R$
<i>SY</i>		Centered on Y-axis	$x^2 + (y - \bar{y})^2 + z^2 - R^2 = 0$	$\bar{y} R$
<i>SZ</i>		Centered on Z-axis	$x^2 + y^2 + (z - \bar{z})^2 - R^2 = 0$	$\bar{z} R$
<i>C/X</i>		Cylinder	Parallel to X-axis	$(y - \bar{y})^2 + (z - \bar{z})^2 - R^2 = 0$
<i>C/Y</i>	Parallel to Y-axis		$(x - \bar{x})^2 + (z - \bar{z})^2 - R^2 = 0$	$\bar{x} \bar{z} R$
<i>C/Z</i>	Parallel to Z-axis		$(x - \bar{x})^2 + (y - \bar{y})^2 - R^2 = 0$	$\bar{x} \bar{y} R$
<i>CX</i>	On X-axis		$y^2 + z^2 - R^2 = 0$	<i>R</i>
<i>CY</i>	On Y-axis		$x^2 + z^2 - R^2 = 0$	<i>R</i>
<i>Cz</i>	On Z-axis		$x^2 + y^2 - R^2 = 0$	<i>R</i>

Form: *j n a list*

where,

*j* = surface number  $1 \leq i \leq 99999$ , can add an asterick for a reflecting surface or plus for a white boundary



*n* = coordinate transformation, absent if no coordinate transformations are present in surface, 0, specifies number of TRn card, < 0, specifies surface j is periodic with surface n

*a* = equation mnemonic from MCNP

*list* = one to ten entries for the equation of the surface, as required

## Appendix A.2: Derivation of the F4 Tally

Define the scalar flux as,

$$\phi(\vec{r}, E, t) = \int d\Omega \Psi(\vec{r}, \Omega, E, t) \quad \text{A.1.1}$$

then, the value of,

$$\phi(\vec{r}, E, t) d\vec{r} dE \quad \text{A.1.2}$$

is the total scalar flux in volume element  $d\vec{r}$  about  $\vec{r}$  and energy element  $dE$  about  $E$ . Now introduce energy and time bins to convert the F4 equation provided in Table 4.2 into,

$$F4 = \frac{1}{V} \int_{E_i} dE \int_{t_j} dt \int dV \phi(\vec{r}, E, t) \quad \text{A.1.3}$$

Going back to the full equation from Table 4.2, expand the equation as follows,

$$\bar{\phi}_V = \frac{1}{V} \int dE \int dt \int dV \int d\Omega \Psi(\vec{r}, \Omega, E, t) \quad \text{A.1.4}$$

$$\bar{\phi}_V = \frac{1}{V} \int dE \int dt \int dV \int d\Omega v n(\vec{r}, \Omega, E, t) \quad \text{A.1.5}$$

$$\bar{\phi}_V = \frac{1}{V} \int dE \int dt \int dV v N(\vec{r}, \Omega, E, t) \quad \text{A.1.6}$$

where,

$$N(\vec{r}, \Omega, E, t) = \int d\Omega n(\vec{r}, \Omega, E, t) \quad \text{A.1.7}$$

is the density of particles, regardless of trajectory at a given point. define  $ds$  to be the unit of track length, which is given by,

$$ds = v dt \quad \text{A.1.8}$$

Applying this to the above yields the following equation:

$$\bar{\phi}_V = \frac{1}{V} \int dE \int dV \int ds N(\vec{r}, E, t) \quad \text{A.1.9}$$

The quantity  $N(\vec{r}, E, t)ds$  may be thought as a track length density. Therefore, the average flux can be estimated by summing the track lengths. This is the exact method MCNP uses to calculate the value of  $\bar{\phi}_V$ , by summing  $WT_l/V$  for all particle tracks in a given cell. The method of using the track length estimator is considered reliable since there are frequently many particle tracks in a given cell, which contribute to the value of this tally.

## Appendix A.3: Section of General MCNP Input File for Automation

General MCNP input deck

```

c -----
c Cell cards
c -----
c
c This next set of cells defines the elements (1)
c
  1 10 -10.4    -1 4 -5                tmp=8.2782e-8 imp:n=1 $1st Fuel
  2 90 -AAAAAAAAA -1 5 -6            tmp=8.2782e-8 imp:n=1 $1st End Pellet
  3 90 -AAAAAAAAA -1 6 -7            tmp=8.2782e-8 imp:n=1 $2nd End Pellet
  4 80 -0.0014   -1 7 -8                tmp=2.9414e-8 imp:n=1 $1st Air Gap (He)
  5 80 -0.0014   -1 12 -13           tmp=2.9414e-8 imp:n=1 $2nd Air Gap (He)
  6 90 -AAAAAAAAA -1 13 -14          tmp=8.2782e-8 imp:n=1 $3rd End Pellet
  7 90 -AAAAAAAAA -1 14 -15          tmp=8.2782e-8 imp:n=1 $4th End Pellet
  8 10 -10.4    -1 15 -16            tmp=8.2782e-8 imp:n=1 $2nd Fuel
  9 40 -2.1914   1 -2 4 -8            tmp=5.1702e-8 imp:n=1 $1st CANLUB
 10 40 -2.1914   1 -2 12 -16         tmp=5.1702e-8 imp:n=1 $2nd CANLUB
 11 30 -6.5      (-3 -9 8);(-3 -8 2 4) tmp=4.8425e-8 imp:n=1 $1st Sheath
 12 30 -5.03     -3 9 -10            tmp=4.8425e-8 imp:n=1 $1st End Plate
 13 30 -5.03     -3 10 -11           tmp=4.8425e-8 imp:n=1 $2nd End Plate
 14 30 -6.5      (-3 11 -12);(-3 12 2 -16) tmp=4.8425e-8 imp:n=1 $2nd Sheath
c
c The next set of cells is used to define element 2 (ring 1)
c
 15 10 -10.4    -21 4 -5                tmp=8.2782e-8 imp:n=1 $1st Fuel
 16 90 -10.4    -21 5 -6            tmp=8.2782e-8 imp:n=1 $1st End Pellet
 17 90 -10.4    -21 6 -7            tmp=8.2782e-8 imp:n=1 $2nd End Pellet
 18 80 -0.0014   -21 7 -8                tmp=2.9414e-8 imp:n=1 $1st Air Gap (He)
 19 80 -0.0014   -21 12 -13          tmp=2.9414e-8 imp:n=1 $2nd Air Gap (He)
 20 90 -10.4    -21 13 -14          tmp=8.2782e-8 imp:n=1 $3rd End Pellet
 21 90 -10.4    -21 14 -15          tmp=8.2782e-8 imp:n=1 $4th End Pellet
 22 10 -10.4    -21 15 -16            tmp=8.2782e-8 imp:n=1 $2nd Fuel
 23 40 -2.1914   21 -22 4 -8          tmp=5.1702e-8 imp:n=1 $1st CANLUB
 24 40 -2.1914   21 -22 12 -16       tmp=5.1702e-8 imp:n=1 $2nd CANLUB
 25 30 -6.5      (-23 -9 8);(-23 -8 22 4) tmp=4.8425e-8 imp:n=1 $1st Sheath
 26 30 -5.03     -23 9 -10            tmp=4.8425e-8 imp:n=1 $1st End Plate
 27 30 -5.03     -23 10 -11          tmp=4.8425e-8 imp:n=1 $2nd End Plate
 28 30 -6.5      (-23 11 -12);(-23 12 22 -16) tmp=4.8425e-8 imp:n=1 $2nd Sheath
c

```

## Appendix A.4: MATLAB Script to Generate a Set of MCNP Trials

```
%%%%%%%%%%%%%%%%%%%%%%%%%%%%%%%%%%%%%%%%%%%%%%%%%%%%%%%%%%%%%%%%%%%%%%%%
%%%%%%%%%%%%%%%%%%%%%%%%%%%%%%%%%%%%%%%%%%%%%%%%%%%%%%%%%%%%%%%%%%%%%%%%
%%%%%%%%%%%%%%%%%%%%%%%%%%%%%%%%%%%%%%%%%%%%%%%%%%%%%%%%%%%%%%%%%%%%%%%% AUTOMATION CODE COMPLETE AUTOMATED INPUTS GENERATED %%%%%%%%%
%%%%%%%%%%%%%%%%%%%%%%%%%%%%%%%%%%%%%%%%%%%%%%%%%%%%%%%%%%%%%%%%%%%%%%%%
%%%%%%%%%%%%%%%%%%%%%%%%%%%%%%%%%%%%%%%%%%%%%%%%%%%%%%%%%%%%%%%%%%%%%%%%
```

```
% Center ring configuration
% Defining the isotopic abundance of each isotope in the absorber
IA_Eu_151=0.412808365000;
IA_Eu_153=0.450807461000;
IA_OEu_16=0.136384172000;
```

```
% Defining the isotopic abundance of each isotope in the fuel
IA_U_235=0.0063;
IA_U_238=0.8752;
IA_O2_16=0.1185;
% Creating a zero
zero = 0.0;
```

```
% Defining the number of elements absorber is distributed amongst, Mass in grams and Volume in cm^3
Number_of_Pellets=1;
Pellet_Mass=18.9025137525;
Pellet_Volume=1.800239405;
Fuel_Density=10.40;
Eu_Density=7.40;
trial_num=5;
```

```
for Absorber_Mass=0.005:0.01:0.035
```

```
    fopen('AT_NU_CnR.txt');
```

```
    string_MCNP=fileread('AT_NU_CnR.txt');
```

```
    Absorber_Mass_Distributed=Absorber_Mass/Number_of_Pellets;
```

```
    Vol_Absorber = Absorber_Mass_Distributed/Eu_Density;
```

```
    Vol_U_p = Pellet_Volume-Vol_Absorber;
```

```
    Mass_U_p = Fuel_Density.*Vol_U_p;
```

```
    Decimal_Eu_151=((Absorber_Mass_Distributed.*IA_Eu_151)/(Absorber_Mass_Distributed+
    Decimal_Eu_153=((Absorber_Mass_Distributed.*IA_Eu_153)/(Absorber_Mass_Distributed+
    Decimal_OEu_16=((Absorber_Mass_Distributed.*IA_OEu_16)/(Absorber_Mass_Distributed+
    Decimal_U_235=((Mass_U_p.*IA_U_235)/(Absorber_Mass_Distributed+Mass_U_p));
    Decimal_U_238=((Mass_U_p.*IA_U_238)/(Absorber_Mass_Distributed+Mass_U_p));
    Decimal_O2_16=((Mass_U_p.*IA_O2_16)/(Absorber_Mass_Distributed+Mass_U_p));
```

```
    Eu_151_1=strfind(string_MCNP,'AAAAAAAAAAAA');
    window=string_MCNP(Eu_151_1:Eu_151_1+12);
```

```

new_Eu_151_1=sprintf('%0.10f',Decimal_Eu_151);
new=strrep(string_MCNP>window,new_Eu_151_1);

Eu_153_1=strfind(string_MCNP,'BBBBBBBBBBBB');
window=string_MCNP(Eu_153_1:Eu_153_1+12);
new_Eu_153_1=sprintf('%0.10f',Decimal_Eu_153);
new2=strrep(new>window,new_Eu_153_1);

U_235_1=strfind(string_MCNP,'CCCCCCCCCCCC');
window=string_MCNP(U_235_1:U_235_1+12);
new_U_235_1=sprintf('%0.10f',Decimal_U_235);
new3=strrep(new2>window,new_U_235_1);

U_238_1=strfind(string_MCNP,'DDDDDDDDDDDD');
window=string_MCNP(U_238_1:U_238_1+12);
new_U_238_1=sprintf('%0.10f',Decimal_U_238);
new4=strrep(new3>window,new_U_238_1);

O2_16_1=strfind(string_MCNP,'EEEEEEEEEEEE');
window=string_MCNP(O2_16_1:O2_16_1+12);
new_O2_16_1=sprintf('%0.10f',(Decimal_O2_16+Decimal_OEu_16));
new5=strrep(new4>window,new_O2_16_1);

Mat_Density=(Absorber_Mass_Distributed+Mass_U_p)/Pellet_Volume;

Cell_Density_1=strfind(string_MCNP,'MMMMMMMMMMMMMM');
window=string_MCNP(Cell_Density_1:Cell_Density_1+12);
new_Cell_Density_1=sprintf('%0.10f',Mat_Density);
new6=strrep(new5>window,new_Cell_Density_1);

input_title='AT_Cn_Eu5';

input=strcat(input_title,'_Eu',num2str(trial_num),'.txt');

fid=fopen(input,'w');

fprintf(fid,'%s',new6);

fclose('all');

trial_num=trial_num+10;
end
%%%%%%%%%%%%%%%%%%%%%%%%%%%%%%%%%%%%%%%%%%%%%%%%%%%%%%%%%%%%%%%%%%%%%%%%

```

## Appendix A.5: Batch Script to Execute Multiple MCNP Inputs

```
@ set MCNPPATH=c:\MCNP6\MCNP_CODE\bin  
@ PATH %MCNPPATH%;%PATH%
```

```
@ set DISPLAY=:0.0
```

```
@ set DATAPATH=C:\MCNP6\MCNP_DATA
```

```
echo on
```

```
cd..
```

```
cd..
```

```
cd..
```

```
cd mcnp6/mcnp_code/mcnp6/current_work/eu_eu_trial
```

```
cd center
```

```
cd 12mg
```

```
mcnp6 i=AT_Eu12_Eu33.txt n=AT_Eu12_Eu33 tasks 12
```

```
mcnp6 i=AT_Eu12_Eu34.txt n=AT_Eu12_Eu34 tasks 12
```

```
mcnp6 i=AT_Eu12_Eu35.txt n=AT_Eu12_Eu35 tasks 12
```

```
cd..
```

## Appendix A.6: MATLAB Script to Lift Output From MCNP Output File

```
%%%%%%%%%%%%%%%%%%%%%%%%%%%%%%%%%%%%%%%%%%%%%%%%%%%%%%%%%%%%%%%%%%%%%%%%  
%%%%%%%%%%%%%%%%%%%%%%%%%%%%%%%%%%%%%%%%%%%%%%%%%%%%%%%%%%%%%%%%%%%%%%%%  
%%%%%%%%%%%%%%%%%%%%%%%%%%%%%%%%%%%%%%%%%%%%%%%%%%%%%%%%%%%%%%%%%%%%%%%% THIS CODE IS USED TO AUTOMATE THE OUTPUT OF MCNP %%%%%%%%%  
%%%%%%%%%%%%%%%%%%%%%%%%%%%%%%%%%%%%%%%%%%%%%%%%%%%%%%%%%%%%%%%%%%%%%%%%  
%%%%%%%%%%%%%%%%%%%%%%%%%%%%%%%%%%%%%%%%%%%%%%%%%%%%%%%%%%%%%%%%%%%%%%%%
```

```
% This output automation code is used to compare the effect of different  
% mass of absorbers has on the EFP value and axial profile.
```

```
trial_num = 0;
```

```
for a = 1:1:6
```

```
    trial_num = trial_num + 1;
```

```
    if trial_num == 1
```

```
        output_title='AT_OP_Gd';  
        output=strcat(output_title,'_',num2str(trial_num),'_1000','.txt');  
        results4 = importfile4(output);  
        error4 = importerror4(output);  
        xlswrite('Gd_OP_1000.xlsx',results4,1,'E4');  
        xlswrite('Gd_OP_1000.xlsx',error4,1,'F4');
```

```
    elseif trial_num == 2
```

```
        output_title='AT_OP_Gd';  
        output=strcat(output_title,'_',num2str(trial_num),'_1000','.txt');  
        results4 = importfile4(output);  
        error4 = importerror4(output);  
        xlswrite('Gd_OP_1000.xlsx',results4,1,'H4');  
        xlswrite('Gd_OP_1000.xlsx',error4,1,'I4');
```

```
    elseif trial_num == 3
```

```
        output_title='AT_OP_Gd';  
        output=strcat(output_title,'_',num2str(trial_num),'_1000','.txt');  
        results4 = importfile4(output);  
        error4 = importerror4(output);  
        xlswrite('Gd_OP_1000.xlsx',results4,1,'K4');  
        xlswrite('Gd_OP_1000.xlsx',error4,1,'L4');
```

```
    elseif trial_num == 4
```

```
        output_title='AT_OP_Gd';  
        output=strcat(output_title,'_',num2str(trial_num),'_1000','.txt');  
        results4 = importfile4(output);  
        error4 = importerror4(output);  
        xlswrite('Gd_OP_1000.xlsx',results4,1,'N4');
```



```

        xlswrite('Gd_OP_1000.xlsx',error4,1,'O4');

elseif trial_num == 5

    output_title='AT_OP_Gd';
    output=strcat(output_title,'_',num2str(trial_num),'_1000','.txt');
    results4 = importfile4(output);
    error4 = importerror4(output);
    xlswrite('Gd_OP_1000.xlsx',results4,1,'Q4');
    xlswrite('Gd_OP_1000.xlsx',error4,1,'R4');

elseif trial_num == 6

    output_title='AT_OP_Gd';
    output=strcat(output_title,'_',num2str(trial_num),'_1000','.txt');
    results4 = importfile4(output);
    error4 = importerror4(output);
    xlswrite('Gd_OP_1000.xlsx',results4,1,'T4');
    xlswrite('Gd_OP_1000.xlsx',error4,1,'U4');

end

end

trial_num = 0;

for b = 1:1:6

    trial_num = trial_num +1;

    if trial_num == 1

        output_title='AT_OP_Gd';
        output=strcat(output_title,'_',num2str(trial_num),'_0100','.txt');
        results3 = importfile3(output);
        error3 = importerror3(output);
        xlswrite('Gd_OP_0100.xlsx',results3,1,'E4');
        xlswrite('Gd_OP_0100.xlsx',error3,1,'F4');

elseif trial_num == 2

        output_title='AT_OP_Gd';
        output=strcat(output_title,'_',num2str(trial_num),'_0100','.txt');
        results3 = importfile3(output);
        error3 = importerror3(output);
        xlswrite('Gd_OP_0100.xlsx',results3,1,'H4');
        xlswrite('Gd_OP_0100.xlsx',error3,1,'I4');

elseif trial_num == 3

        output_title='AT_OP_Gd';
        output=strcat(output_title,'_',num2str(trial_num),'_0100','.txt');
        results3 = importfile3(output);
        error3 = importerror3(output);

```

```
xlswrite('Gd_OP_0100.xlsx',results3,1,'K4');
xlswrite('Gd_OP_0100.xlsx',error3,1,'L4');
```

```
elseif trial_num == 4
```

```
output_title='AT_OP_Gd';
output=strcat(output_title,'_',num2str(trial_num),'_0100','.txt');
results3 = importfile3(output);
error3 = importerror3(output);
xlswrite('Gd_OP_0100.xlsx',results3,1,'N4');
xlswrite('Gd_OP_0100.xlsx',error3,1,'O4');
```

```
elseif trial_num == 5
```

```
output_title='AT_OP_Gd';
output=strcat(output_title,'_',num2str(trial_num),'_0100','.txt');
results3 = importfile3(output);
error3 = importerror3(output);
xlswrite('Gd_OP_0100.xlsx',results3,1,'Q4');
xlswrite('Gd_OP_0100.xlsx',error3,1,'R4');
```

```
elseif trial_num == 6
```

```
output_title='AT_OP_Gd';
output=strcat(output_title,'_',num2str(trial_num),'_0100','.txt');
results3 = importfile3(output);
error3 = importerror3(output);
xlswrite('Gd_OP_0100.xlsx',results3,1,'T4');
xlswrite('Gd_OP_0100.xlsx',error3,1,'U4');
```

```
end
```

```
end
```

```
trial_num = 0;
```

```
%%%%%%%%%%%%%%%%%%%%%%%%%%%%%%%%%%%%%%%%%%%%%%%%%%%%%%%%%%%%%%%%%%%%%%%%%
```

## Appendix A.7: MATLAB Script for Function “importfile” Used In MATLAB Output Script

```
function Result = importfile1(filename, startRow, endRow)
%IMPORTFILE Import numeric data from a text file as column vectors.
% RESULT = IMPORTFILE(FILENAME) Reads data from text file FILENAME for the default selection.
% RESULT = IMPORTFILE(FILENAME, STARTROW, ENDROW) Reads data from rows
% STARTROW through ENDROW of text file FILENAME.

if nargin<=2
    startRow = 13;
endRow = 252;
end

column5: double (%f)
    formatSpec = '%*41s%12f%[\n\r]';
    fileID = fopen(filename,'r');
    textscan(fileID, '%[\n\r]', startRow(1)-1, 'ReturnOnError', false);
    dataArray = textscan(fileID, formatSpec, endRow(1)-startRow(1)+1, 'Delimiter', '');

for block=2:length(startRow)
    frewind(fileID);
    textscan(fileID, '%[\n\r]', startRow(block)-1, 'ReturnOnError', false);
    dataArrayBlock = textscan(fileID, formatSpec, endRow(block)-startRow(block)+1,
    dataArray{1} = [dataArray{1};dataArrayBlock{1}];
end

fclose(fileID);
Result = dataArray{: , 1};
%%%%%%%%%%%%%%%%%%%%%%%%%%%%%%%%%%%%%%%%%%%%%%%%%%%%%%%%%%%%%%%%%%%%%%%%%
```

## Appendix A.8: MATLAB Script for Function “importerror” Used In MATLAB Output Script

```
function RelError = importerror1(filename, startRow, endRow)
%IMPORTFILE Import numeric data from a text file as column vectors.
% RELERROR = IMPORTFILE(FILENAME) Reads data from text file FILENAME for the default selection
% RELERROR = IMPORTFILE(FILENAME, STARTROW, ENDROW) Reads data from rows
% STARTROW through ENDROW of text file FILENAME.

if nargin<=2
startRow = 13;
endRow = 252;
end

column6: double (%f)
formatSpec = '%*53s%12f%[\n\r]';
fileID = fopen(filename,'r');
textscan(fileID, '%[\n\r]', startRow(1)-1, 'ReturnOnError', false);
dataArray = textscan(fileID, formatSpec, endRow(1)-startRow(1)+1, 'Delimiter', '');

for block=2:length(startRow)
frewind(fileID);
textscan(fileID, '%[\n\r]', startRow(block)-1, 'ReturnOnError', false);
dataArrayBlock = textscan(fileID, formatSpec, endRow(block)-startRow(block)+1,
dataArray{1} = [dataArray{1};dataArrayBlock{1}];
end

fclose(fileID);
RelError = dataArray{: , 1};
%%%%%%%%%%%%%%%%%%%%%%%%%%%%%%%%%%%%%%%%%%%%%%%%%%%%%%%%%%%%%%%%%%%%%%%%%
```

## Appendix A.9: Python Script to Determine the Optimal Amount of Europium Oxide

```
# *****  
# *** LEAST SQUARES METHOD ONLY NEEDED FOR TWO PELLET EUROPIUM CASES ***  
# ***** AS DETERMINED IN THE PRELIMINARY WORK *****  
# *****  
  
# Getting some user inputs  
print('What location are the trials from?')  
location = input()  
  
# Defining variables used in the script  
count = 0  
midflux = 0.0  
EFP_val = 0  
Score = 0  
Score_List = []  
Score_List_final = []  
  
# Depending on the fuel ring location the total axial mesh density (# of mesh points) might differ  
if location == 'Cn':  
    count = 100  
elif location == 'In':  
    count = 100  
elif location == 'It':  
    count = 100  
elif location == 'Ou':  
    count = 100  
  
# Specify the keyline parameters  
keyline = ' 6.250E-07'  
  
print(count)  
  
# Python Script to generate a Least Squares Comparison for MCNP results  
i = 0  
j = 1  
k = 0  
  
# Run a loop to go through all the output files for a certain location  
while j < 10:  
  
    # Step j by 1 for each loop iteration  
    #j += 1  
  
    while k < 10:  
  
        # Step k by 1 for each loop iteration
```

```

k += 1

input = 'AT_' + location + '_Eu' + str(j) + '_Eu' + str(k) + '.txt'

outputfile = open('least_squares_' + 'Eu' + str(j) + '_Eu' + str(k) + '.txt', 'w')
# Write a header to the output file
outputfile.write('Trial_Identifier' + "\t" + 'Position (cm)' + "\t" + 'Flux_Value' + "\t" + 'EFP_Value' + "\t" \
    + 'Residual Squared' + "\n")

with open(input, 'r') as file_in:
    lines = file_in.readlines()[15:]

    for line in lines:

        i += 1

        if i < count:

            if line[:11] == keyline and i == 1:
                midflux = float(line[42:53])

            if line[:11] == keyline:
                EFP_val = float(line[42:53]) / midflux

                ResSqd = (1.0 - EFP_val) ** 2

                outputfile.write('Eu' + str(j) + '_Eu' + str(k) + "\t" + line[25:30] + "\t" + line[42:53] \
                    + "\t" + str(EFP_val) + "\t" + str(ResSqd) + "\n")

                Score += ResSqd

        i = 0

        outputfile.write('Sum of squared residuals = ' + str(Score) + "\n")
        file_in.close()
        outputfile.close()
# Error with score list because there isn't a proper number of input files
Score_List.append(Score)
print(Score_List)

Score = 0

k = 0
j += 1
print(j)

# --- End of File ---

```